ISSN 1451 - 9372 (Print)
ISSN 2217 - 7434 (Online)
APRIL-JUNE 2023
Vol.29, Number 2, 87-167

Chemical Industry & Chemical Engineering Quarterly

The AChE Journal for Chemical Engineering, Biochemical Engineering, Chemical Technology, New Materials, Renewable Energy and Chemistry

www.ache.org.rs/ciceq

Journal of the
Association of Chemical Engineers of
Serbia, Belgrade, Serbia

Chemical Industry & Chemical Engineering
CI&CEQuarterly

Journal of the
Association of Chemical Engineers of
Serbia, Belgrade, Serbia

Chemical Industry & Chemical Engineering Quarterly

Vol. 29 | Belgrade, April-June 2023 | No. 2

Chemical Industry & Chemical Engineering Quarterly (ISSN 1451-9372) is published quarterly by the Association of Chemical Engineers of Serbia, Kneza Miloša 9/I, 11000 Belgrade, Serbia

Editor:
Vlada B. Veljković
veljkovic@yahoo.com

Editorial Office:
Kneza Miloša 9/I, 11000 Belgrade, Serbia
Phone/Fax: +381 (0)11 3240 018
E-mail: shi@ache.org.rs
www.ache.org.rs

For publisher:
Ivana T. Drvenica

Secretary of the Editorial Office:
Slavica Desnica

Marketing and advertising:
AChE Marketing Office
Kneza Miloša 9/I, 11000 Belgrade, Serbia
Phone/Fax: +381 (0)11 3240 018

Publication of this Journal is supported by the Ministry of Education, Science and Technological Development of the Republic of Serbia

Subscription and advertisements make payable to the account of the Association of Chemical Engineers of Serbia, Belgrade, No. 205-2172-71, Komercijalna banka a.d., Beograd

Computer typeface and paging:
Marija B. Tasić

Journal manager:
Aleksandar B. Dekanski

Printed by:
Faculty of Technology and Metallurgy, Research and Development Centre of Printing Technology, Karnegijeva 4, P.O. Box 3503, 11120 Belgrade, Serbia

Abstracting/Indexing:
Articles published in this Journal are indexed in *Thompson Reuters* products: *Science Citation Index - Expanded*™ - access *via Web of Science*®, part of *ISI Web of Knowledge*℠

CONTENTS

The activities of the Association of Chemical Engineers of Serbia are supported by:

MINISTRY OF SCIENCE, TECHNOLOGICAL DEVELOPMENT AND INNOVATION OF REPUBLIC OF SERBIA

Faculty of Technology and Metallurgy, University of Belgrade

Faculty of Science, University of Novi Sad

Institute for Technology of Nuclear and Other Mineral Raw Materials, Bekgrade

Faculty of Technology, University of Novi Sad

Institute of Chemistry, Technology and Metallurgy, University of Belgrade

Faculty of Technical Sciences University of Novi Sad

Faculty of Technology, University of Niš, Leskovac

Faculty of Technical Sciences, University of Priština, Kosovska Mitrovica

IMS Institute, Belgrade

DCP HEMIGAL
Leskovac

Elixir Prahovo

CI&CEQ
Chemical Industry & Chemical Engineering Quarterly

Available online at
Association of the Chemical Engineers of Serbia AChE
www.ache.org.rs/CICEQ

Chem. Ind. Chem. Eng. Q. 29 (2) 87–98 (2023) CI&CEQ

RAJASEKAR SUBRAMANYAM
MEYYAPPAN NARAYANAN

Department of Chemical Engineering, Sri Venkateswara College of Engineering, Tamil Nadu, India

ARTIFICIAL NEURAL NETWORK MODELING FOR DRYING KINETICS OF PADDY USING A CABINET TRAY DRYER

Article Highlights

- The drying temperature has a significant positive correlation on drying kinetics than air velocity
- ANN modeling with activation function TANSIGMOID shows the best prediction of drying kinetics
- ANN modeling shows exceptionally better prediction accuracy than mathematical modeling

Abstract

The study of drying kinetics and characteristics of agricultural products is essential for drying time estimation, designing dryers, and optimizing the drying process. Moisture diffusivity under different drying conditions is crucial to process and equipment design. The drying kinetics of paddy using a cabinet tray dryer was modeled using an Artificial Neural Network (ANN) technique. For predicting moisture ratio and drying rate, the Levenberg-Marquardt (LM) training algorithm with TANSIGMOID and TANSIGMOID hidden layer activation function provided superior results. A comparative evaluation of the predicting abilities of ANN and 12 different mathematical drying models was also carried out. The Midilli model was adequate for fitting the experimental data with an R^2 comparable to that of the ANN. However, the RMSE observed for ANN (0.0360) was significantly lower than that of the Midilli model (0.1673 to 0.712). Effective moisture diffusivity increased with an increase in temperature from 15.05 10^{-9} m^2/s to 28.5 10^{-9} m^2/s. The activation energy for drying paddy grains varied between 6.8 kJ/mol to 7.3 kJ/mol, which showed a moderate energy requirement for moisture diffusion.

Keywords: cabinet tray dryer, equilibrium moisture content, mathematical modeling, ANN modeling, effective diffusivity, activation energy.

SCIENTIFIC PAPER

UDC 66.047:66:632.51

Paddy (*Oryza Sativa* L.) is a staple food in most countries. It is regarded as one of the world's most essential nutritious staple food crops among cereals due to its use as human food and animal feed [1]. Drying is one of the earliest preservation procedures used to reduce the moisture content of biological materials to a level that inhibits microbial development and reduces the rate of deteriorative chemical reactions. Besides improving shelf life, drying allows for the development of a wide range of value-added goods from agricultural food [2]. The growing global demand for high-quality dried paddy rice has prompted the investigation of viable preservation solutions [3]. Cabinet tray drying is a versatile method because of its ease of operation. It is a ubiquitous drying technique. It retains the quality and nutritional content of dried material compared to sun drying, infrared drying, freeze-drying, fluidized bed drying, and dielectric drying [4]. The paddy will be spread out on the trays, with a heating medium (hot air) passing through. The drying process can be efficient by ensuring uniform airflow distribution across the trays. Besides many matematical

Correspondence: M. Narayanan, Department of Chemical Engineering, Sri Venkateswara College of Engineering, Pennalur, Sriperumbudur Tk, Kancheepuram Dt, Tamil Nadu - 602117, India.
E-mail: nmena@svce.ac.in
Paper received: 6 January, 2022
Paper revised: 6 May, 2022
Paper accepted: 21 July, 2022

https://doi.org/10.2298/CICEQ220106017S

models, artificial neural networks (ANNs) are a sophisticated computational tool for modeling complicated interactions between input and output parameters [5]. ANN analysis can produce more realistic and accurate forecasts [6]. Some of the notable pieces of literature are illustrated below (Table 1).

Table 1. Existing literature report.

Ref.	Year	Methodologies	Inferences
[5]	2016	Statistical analysis	— The drying temperature and tempering duration effects were investigated on drying kinetics and moisture diffusivity. The results showed that adding a tempering stage considerably impacted drying performance and effective moisture diffusivity. — Several thin layer drying models were fitted to experimental data of each drying stage, namely pre-tempering and post-tempering, and the models' appropriateness was assessed using statistical analysis. The Midilli and Tow-Term models were determined to be the most suitable for the first and second drying stages.
[6]	2016	ANN modeling	— Using six distinct models, thin-layer drying kinetic analysis of paddy dried under low-temperature conditions (20°C–40°C) and constant air velocity of 1.41 m/s was performed using a drying chamber. The Midilli model was found to be the best fit for describing the drying behavior of this species of paddy. — The drying constant for paddy drying increased with the drying temperature at low ambient temperatures (20°C–40°C).
[7]	2017	Third-order regression modeling	— The drying kinetics of high moisture paddy at 25% (wet basis) in a cylindrical drying bin were investigated about process variables such as inlet air temperature, rate of airflow, and bed depth. — The drying rate and moisture ratio increased with drying temperature and airflow rate.
[8]	2017	Mathematical and ANN modeling	— To estimate the drying curves of rough rice, a comparison was made between mathematical thin-layer models and artificial neural networks. — The kinetics of the thin layers of grains were investigated when the drying bed was separated into four thin layers (each 5 cm in height). According to the least *RMSE* and *chi-square* values, the Midilli model was the best for describing drying curves among the nine mathematical models employed for the prediction.
[9]	2018	Thermogravimetric analysis	— The thermogravimetric analyzer was used to investigate the isothermal drying kinetics of paddy with three initial dry basis moisture contents of 17.18, 21.05, and 30.12 percent. Under the drying temperature of 50 °C, the final moisture content of the three samples increased from 4.61 to 7.61 percent, with a rise in IMC from 17.18 to 30.12 percent. — The model proposed by Midilli is the most appropriate because the R^2 for the three samples was higher than the R^2 for the other four models.
[10]	2019	Regression analysis	— Paddy's drying kinetics and moisture diffusivity are investigated in a fluidized bed dryer. For drying paddy, different values of drying air temperatures (*T*) of 45 °C, 50 °C, and 55 °C, drying air velocities (*V*) of 2 m/s, 2.5 m/s, and 3 m/s, and paddy inventory of 2 kg and 3 kg are utilized. — The linear regression analysis obtains a regression equation correlating effective moisture diffusivity across all drying process parameters.
[11]	2020	ANN modeling	— To forecast M.R., the ANN approach was used. The impact of different drying processes on parboiled paddy's thermodynamic and qualitative parameters was investigated. Five mathematical approaches were used to predict the moisture ratio of parboiled rice. The results showed that as the intensity of the radiation, the temperature of the air, or the microwave power increased, the product surface temperature and moisture loss increased.
[12]	2021	Nonlinear regression analysis	— The drying kinetics model of paddy at a certain drying period was investigated in a swirling fluidized bed (SFB) drier. The drying was carried out at capacities of 1 kg, 2 kg, and 3 kg, with temperatures of 55 °C, a 45-minute drying duration, and an initial moisture content of 31.23 ± 0.26% percent (d.b.). A linear-plus-exponential model best describes the change in M.R. of paddy with time in the capacity range of 1 kg to 3 kg among the six drying kinetics models.
[13]	2021	ANN and adaptive neuro-fuzzy modeling	— The impact of hot air-drying kinetics on milled rice's quality and microstructural features during the instant controlled pressure drop (ICPD) assisted parboiling process was examined. In addition, the thin layer drying dynamics were studied using mathematical modeling. The Midilli model, which had the highest R^2 and the lowest *RMSE* and SSE values of the five mathematical models, predicted the best drying behavior of ICPD-treated parboiled rice grains.

However, considering the above inferences, the authors could not inspect any available literature investigating cabinet tray drying kinetics for paddy. Paddy drying kinetics prediction needs a more accurate and reliable method to attain better accuracy using evaluation metrics. Based on these needs, this work focused on the following objectives:

To assess the drying kinetics of paddy at different drying conditions; to estimate the equilibrium moisture content using the static gravimetric technique; to demonstrate ANN modeling using different activation functions such as TANSIGMOID, LOGSIGMOID, and PURELIN for paddy drying; To analyze the ANN modeling techniques using evaluation metrics such as

R^2, *RMSE*, and mean absolute error (*MAE*); To select and recommend the most accurate prediction technique to evaluate the drying kinetics of paddy.

MATERIAL AND METHODS

The paddy variety (rice CO 51) was collected from an agricultural field near Sriperumbudur, Tamilnadu, India. A paddy of fixed mass (100 g) was steeped in a constant temperature water bath for 3 hours at 45 °C, The excess water was drained, and surface moisture was removed by spreading it on the floor or using a muslin cloth. It has typically resulted in a moisture content of 26% on a dry basis. The conventional oven technique assessed the sample's initial moisture content (IMC). The convective cabinet tray dryer (Fig.1) was used for the study with only one tray in position, and it had a provision to control the temperature. The dimensions of the drying chamber were 250 mm x 250 mm x 300 mm with an air circulating fan (2HP centrifugal air blower). The air velocity was monitored and measured using a rotameter. A digital weighing balance with an accuracy of ±0.01 g was used to measure the weight loss. Paddy samples of approximately 100 g were dehydrated in a convective cabinet tray dryer at different drying temperatures of 40 °C, 50 °C, 60 °C, and 70 °C and air velocities of 1 m/s, 1.5 m/s, and 2 m/s. A thermostat was used to manage the tray dryer drying temperature. Moisture loss was measured every 5 minutes until equilibrium was established.

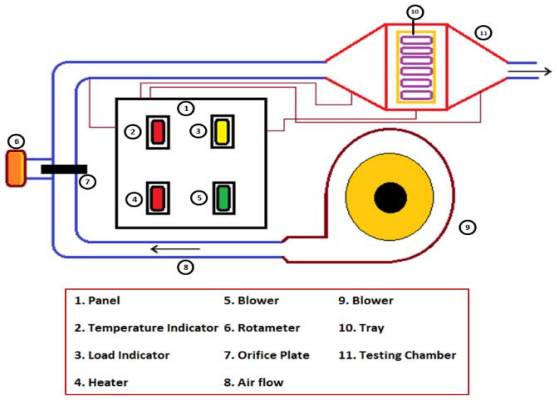

Figure 1. Schematic representation of cabinet tray dryer.

Radius of paddy

The volume displacement method using kerosene as the fluid was used to measure the paddy radius (r) by Eq. (1).

$$\text{Change in volume: } (V_f - V_i) = N \cdot \frac{4}{3}\pi r^3 \quad (1)$$

where N is number of dried paddy kernels, V_i is the initial volume of kerosene and V_f is the final volume of the kerosene.

$$\text{radius of the paddy: } r = \sqrt[3]{\frac{3\cdot(V_f - V_i)}{4\pi N}} \quad (2)$$

This method could only determine the approximate value of radius because the volume of individual paddy has been approximated to the volume of a perfect sphere. Therefore, the radius of the paddy grain is calculated to be 1.683 mm.

Equilibrium moisture content - relative humidity (EMC-RH)

The static gravimetric technique was utilized to determine the paddy's equilibrium moisture content (EMC) [14]. In a confined chamber, saturated solutions of different inorganic salts were used for sorption investigations to achieve regulated humidities ranging from 30% to 85% (5 levels), such as concentrated magnesium chloride, magnesium nitrate, sodium nitrate, sodium chloride, and potassium chloride. The sorption process was investigated at a temperature of 28 °C for paddy. For each of these trials, a 10 g sample of paddy was placed individually in desiccators in porous paper bags. The loss of moisture per unit weight of bone-dry material was used to calculate moisture content on a dry basis (d.b.). The increase or loss of weight of samples in each desiccator was tracked regularly until two successive measurements were consistent. Due to the nature of the samples, this took 36–40 days. For every sample, four homologs were preserved, and the average EMC values were taken. The moisture content of a paddy sample was tested by drying it for 24 hours at 105 °C. The samples were measured on a precision electronic balance with a least count of ±0.001 g. Eq. (3) is an appropriate model to estimate the EMC for paddy in the temperature range of 40 °C –70 °C and relative humidity (RH) of 30%–85% [15]:

$$-\ln(1-RH) = \beta(T)\cdot(M_e)^{\alpha} \quad (3)$$

where RH is the relative humidity, M_e is the equilibrium moisture content (d.b.) and T is the temperature (°C).

Determination of effective diffusivity

The effective diffusivity of spherical particles was evaluated using Eq. (4).

$$MR = \frac{6}{\pi^2}\sum_{n=1}^{\infty}\frac{1}{n^2}\exp\left(\frac{-n^2 D_{eff}\pi^2 t}{r^2}\right) \quad (4)$$

where D_{eff} is the effective diffusivity (m^2/s), r is the radius of the grain (m), t is the time of drying in seconds For long drying times, Eq. (4) can be further simplified to the first term of the series [16]. Thus Eq. (4) can be approximated in the logarithmic form to Eq. (5).

$$\ln MR = \ln \frac{6}{\pi^2} - \frac{\pi^2 D\ t}{r^2} \quad (5)$$

The most typical method for determining effective diffusivities is to plot experimental drying data in terms of *ln (MR)* vs. time. From Eq. (5), a plot of *ln(MR)* vs. *t* gives a straight line with a slope of $\pi^2 D / r^2$.

Effect of temperature on diffusivity

The temperature effect on diffusivity can be represented by the Arrhenius type of relationship (Eq.6).

The activation energy were calculated using relation is given by:

$$D = D_0 \exp\left(\frac{E_a}{RT}\right) \quad (6)$$

where D_0 is a constant, E_a is the activation energy required for moisture diffusion (kJ/mol), R is the Universal gas constant = 8.3144 J/mol K. D was measured at different temperatures to evaluate the constant D_0 and (E_a/R). Therefore, the above equation can be linearized as Eq.(7):

$$\ln D = \ln D_0 - E_a / RT \quad (7)$$

MODELING PROCESS

Mathematical modeling

The experimental moisture ratio (MR) data were fitted with twelve mathematical drying models (Table 1). First, the curve fitting tool in MATLAB version.2021 was used to determine the empirical constants and model performance metrics such as R^2, *RMSE*, and reduced chi-square (χ^2) in each model using regression analysis. Then, Eq. (1) was used to calculate the *MR* values.

$$MR = (M - M_e) / (M_0 - M_e) \quad (8)$$

where *MR* is the ratio of moisture, *M* is the moisture content at any time, M_0 is the initial moisture content, and M_e is the equilibrium moisture content. The best-fit coefficients of empirical models were evaluated by minimizing the mean square error between the measured data and predicted data by thin-layer drying models because it captured error between the actual and predicted data. The fmincon (minimum of inhibited nonlinear multivariable function) was used to curtail the *RMSE*. The highest R^2, the χ^2 and least *RMSE* were implied as error functions for the competence of the fit [17,18]. The statistical analysis parameters are represented as follows:

$$R^2 = 1 - \frac{\sum_{i=1}^{n}\left(MR_{\exp,i} - MR_{pre,i}\right)^2}{\sum_{i=1}^{n}\left(MR_{\exp,i} - MR'_{pre,i}\right)^2} \quad (9)$$

$$\chi^2 = \frac{\sum_{i=1}^{n}\left(MR_{\exp,i} - MR_{pre,i}\right)^2}{n - z} \quad (10)$$

$$RMSE = \frac{\sqrt{\left(MR_{\exp,i} - MR_{pre,i}\right)^2}}{n} \quad (11)$$

where $MR_{exp,i}$ is the i^{th} experimentally observed moisture ratio, $MR_{pre,i}$ is the i^{th} predicted moisture ratio, $MR'_{pre,i}$ is the mean average of predicted moisture ratio n is the number of observations, and z, the number of constants in models.

ANN modeling

ANNs have shown the upper hand in serving nonlinear programming over predictable modeling methods due to their rapid learning ability and suitability to nonlinear processes. An input layer, one or more hidden layer(s), and an output layer make up the ANN infrastructure. Each layer is made up of a collection of neurons or nodes. The internal connections between these nodes are known as weights, and they determine which nodes should be triggered based on the relative relevance of each signal. A mathematical activation function is used to process data in the nodes (e.g., TANSIGMOID, LOGSIGMOID, PURELIN, etc.) [19]. ANN learns from examples through iterations (epochs) without prior knowledge of the relationship between the variables being considered. ANN corrects the network by altering the internal connections based on the discrepancy between experimental and predicted results. This iterative process continues until the network predictions are reasonably accurate and consistent with the target data. Model simulations are used to obtain anticipated data once the training model has been tested and validated.

The data were modeled using a multiple-layer Feed-forward backpropagation algorithm network. One of the supervised learning techniques is the backpropagation algorithm (BP). The BP algorithm updates the weights by going ahead and backward until the output vector, and the predicted vector is as close as possible. Nonlinear mapping is a strong suit of the BP method. The primary benefit of adopting BP is that it can learn and adapt independently. Input data such as drying temperature, air velocity, and drying time make up the input layer. The output data, such as moisture ratio and drying rate, are stored in the output layer. 75% of the input data was utilized for training the network, with the remaining 25% being used to test the network. The Levenberg-Marquardt (LM) learning method was used to train ANN, a well-known efficient algorithm [19]. The adaptive learning algorithm was LEARNGDM (gradient descent with momentum weight and bias learning function). This ANN simulation was

done in MATLAB version.2021 with the ANN toolbox (command: NN tool). The number of neurons in the input hidden layer was varied to test various topologies. In addition, various permutations of activation functions in the hidden layers were employed. Standard statistical measures, including coefficient of determination (R^2), root mean square error (*RMSE*), and mean absolute error (*MAE*), were used to assess the predictability of the ANN model.

$$R^2 = 1 - \frac{\sum_{i=1}^{n}\left(y_{i,\exp} - y_{i,\mathrm{mod}}\right)^2}{\sum_{i=1}^{n}\left(y_{i,\exp} - y'_{i,\mathrm{mod}}\right)^2} \quad (12)$$

$$RMSE = \frac{\sqrt{\left(MR_{i,\exp} - MR_{i,\mathrm{mod}}\right)^2}}{n} \quad (13)$$

$$MAE = \frac{1}{n}\sum_{i=1}^{n}\left(y_{i,\exp} - y_{i,\mathrm{mod}}\right) \quad (14)$$

where n is the number of observations, $y_{i,exp}$ is experimental data, $y_{i,mod}$ is predicted data and $y'_{i,mod}$ is mean average of predicted data.

RESULTS AND DISCUSSION

Equilibrium moisture content - Relative humidity (EMC-RH)

The EMC and *RH* for the paddy were analysed. From the results, it was found that EMC decreases with temperature and increases with *RH*, as shown in Table 2. By fitting the data to Eq. (3). coefficients of the Henderson equation β and α were evaluated. β = 0.3461 and α = 2.164 [20]. The equilibrium moisture content at any other relative humidity and temperature can be easily measured by fitting the data to Henderson's equation (Eq. 3).

Table 2. EMC-RH data.

Relative humidity, %	Temperature, °C				
	28	40	50	60	70
	EMC				
33	7.92	7.51	7.40	7.30	7.20
52	9.94	9.90	9.98	9.96	9.53
64	11.56	11.54	11.42	11.26	11.10
75	13.14	13.10	13.05	12.90	12.79
84	16.13	15.18	14.96	14.75	14.55

Effect of drying temperature and air velocity

The moisture content was found to reduce with rising drying time. Moisture content was determined at various temperatures where the equilibrium was reached faster while increasing the temperature. However, removing the bound moisture at low temperatures requires extended time. In the case of higher temperatures (60 and 70) °C, the time taken to reach the equilibrium was less due to the higher diffusivity of moisture from the paddy to the surrounding air [21], the relative humidity of the drying air at a higher temperature was less compared to that at a lower temperature. Due to this reason, there was a higher rate of moisture diffusion as the temperature increased. Furthermore, it could be noted that the temperature affected the drying rate, and the total drying method was found to occur only in the falling rate period, as shown in Fig. 2. [22]. It specified that the method explaining the dehydration behavior of the paddy in a tray dryer was diffusion-governed [23].

Modeling of drying process by various mathematical models

The moisture ratio estimated from the experimental drying data at various temperatures and velocities was matched to twelve thin-layer models. The statistical parameters obtained from the regression analysis of these models are listed in Table 3. The R^2, *RMSE* and χ^2 values for the models varied between 0.899 to 0.999, 0.053 to 0.947, and 0.0001 to 0.0223, respectively. Hence, the model with the highest R^2 and the lowest χ^2 and *RMSE* was considered the best fit [24–27]. The Midilli model, in particular, was shown to be adequate in representing the tray drying behavior of paddy. The moisture ratio was calculated by considering the equilibrium moisture content, which is evaluated using Eq. (9). Fig. 3 was drawn between observed data and data predicted by the Midilli model at different temperatures and velocities [28]. Midilli model describes sufficiently well the drying characteristics of paddy at a given set of conditions [29,30].

Moisture ratio processing by ANN predictive modeling

Several topologies were tested by varying the number of processing elements (neurons) in the input hidden layer. The number of neurons in the hidden input layer varied to find the optimum number of processing elements. Several combinations of activation functions in the input hidden layer and output hidden layer were also employed. The number of processing elements and iterations (epoch) were recorded for each topology. Standard statistical parameters, like *RMSE*, *MAE*, and R^2 were employed to verify the accuracy of the prediction and validate the predictability of the ANN model [31]. After using various ANN topologies to the testing data, it was found that the network with TANSIGMOID – TANSIGMOID activation function combinations and five neurons in the input hidden layer gave the best result with maximum values of R^2, *RMSE*, and *MAE* of 0.9976, 0.0360, and 0.0034 were in accordance with the range reported in the

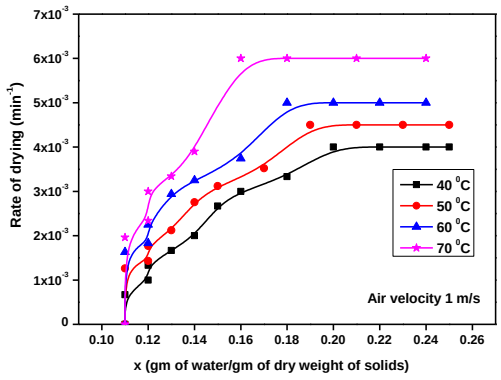

(a)

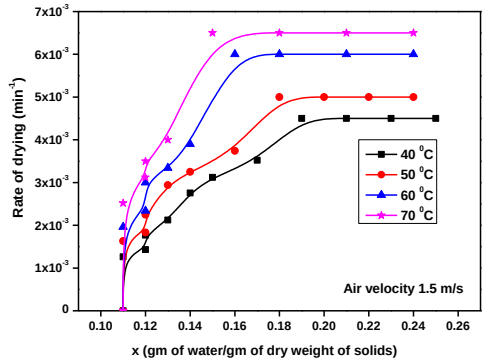

(b)

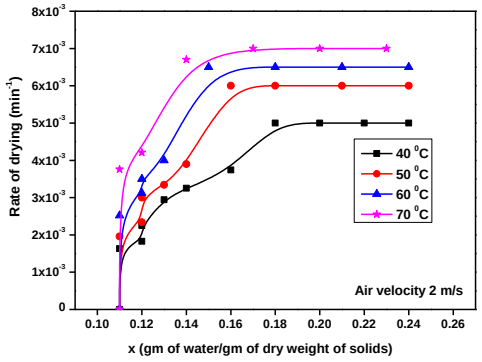

(c)

Figure 2. Rate of drying curves of paddy at different temperature and air velocity of (a) 1 m/s (b) 1.5 m/s (c) 2 m/s.

literature R^2 ranged from 0.981 to 0.999, *RMSE* ranged from 0.0333 to 0.1475 and *MAE* ranged from 0.05318 to 0.0088 [19,32].

Compared to other combinations, most training, validation, and testing data points for TANSIGMOID-TANSIGMOID activation function combinations and five neurons in the input hidden layer were closer to the equity line, indicating better fitness between experimental

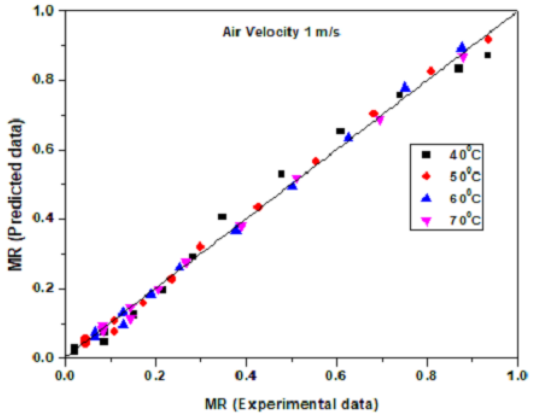

(a)

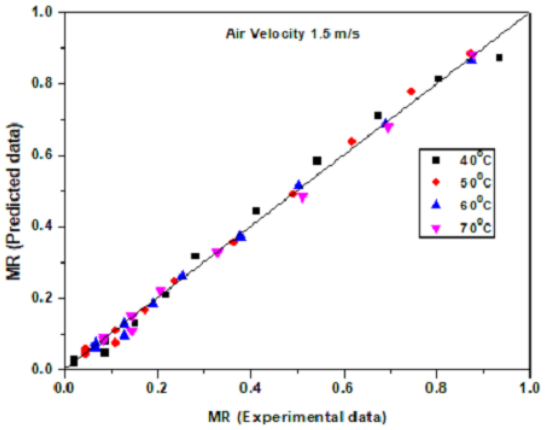

(b)

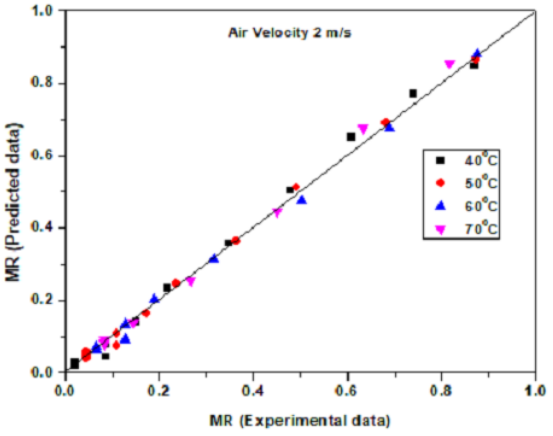

(c)

Figure 3. Experimental MR vs predicted MR by the Midilli model: (a) 1 m/s (b) 1.5 m/s (c) 2 m/s.

and ANN outputs shown in Fig.4. It was also noticed that TANSIGMOID - PURELIN activation function combinations, seven neurons in the input hidden layer showed the minimum deviation, and nine neurons in the input hidden layer with TANSIGMOID - LOGSIGMOID

Table 3. Results of statistical parameters estimated by regression analysis for paddy.

Model, MR =	Statistical parameters	Air velocity, m/s											
		1				1.5				2			
		Temperature °C											
		40	50	60	70	40	50	60	70	40	50	60	70
Page	R^2	0.998	0.997	0.995	0.992	0.999	0.996	0.993	0.981	0.997	0.995	0.982	0.987
$\exp(-kt^n)$	RMSE	0.845	0.573	0.513	0.457	0.834	0.596	0.499	0.571	0.840	0.578	0.612	0.636
	χ^2	0.0002	0.0005	0.0010	0.0019	0.0001	0.0007	0.0016	0.0046	0.00049	0.0011	0.0044	0.0033
Weibull distribution	R^2	0.991	0.994	0.998	0.996	0.992	0.997	0.992	0.992	0.991	0.998	0.993	0.993
$a-b\cdot\exp\left[-(kt^n)\right]$	RMSE	0.726	0.438	0.326	0.266	0.683	0.418	0.321	0.268	0.637	0.418	0.316	0.202
	χ^2	0.019	0.003	0.004	0.0001	0.0017	0.006	0.0012	0.0014	0.0018	0.0002	0.0001	0.0015
Henderson and Pabis	R^2	0.899	0.958	0.981	0.994	0.911	0.966	0.992	0.987	0.923	0.984	0.984	0.981
$a\cdot\exp(-kt)$	RMSE	0.947	0.754	0.545	0.449	0.752	0.702	0.484	0.566	0.570	0.586	0.595	0.626
	χ^2	0.0258	0.0101	0.0044	0.0013	0.0219	0.0078	0.0017	0.0030	0.0183	0.0034	0.0036	0.0047
Two term	R^2	0.964	0.952	0.976	0.992	0.911	0.966	0.987	0.983	0.923	0.984	0.978	0.969
$a\cdot\exp(-k_0t)+b\cdot\exp(-k_1t)$	RMSE	0.946	0.812	0.629	0.292	0.828	0.772	0.359	0.374	0.653	0.741	0.429	0.455
	χ^2	0.0216	0.017	0.0064	0.0017	0.0202	0.0076	0.0028	0.0039	0.0182	0.0042	0.0051	0.0073
Wang and Singh	R^2	0.984	0.991	0.996	0.997	0.989	0.995	0.997	0.994	0.995	0.997	0.993	0.993
$1+at+bt^2$	RMSE	0.732	0.442	0.332	0.318	0.624	0.397	0.363	0.401	0.567	0.437	0.458	0.302
	χ^2	0.0042	0.0021	0.0009	0.0005	0.0026	0.0010	0.0006	0.0014	0.0011	0.0006	0.0014	0.0017
Modified Page	R^2	0.998	0.997	0.995	0.992	0.999	0.996	0.993	0.981	0.997	0.995	0.982	0.987
$\exp\left[-(kt^n)\right]$	RMSE	0.845	0.573	0.513	0.457	0.834	0.596	0.499	0.571	0.840	0.578	0.612	0.636
	χ^2	0.0002	0.0005	0.0010	0.0019	0.0001	0.0007	0.0016	0.0046	0.0004	0.0011	0.0044	0.0033
Verma	R^2	0.913	0.958	0.979	0.991	0.926	0.969	0.988	0.983	0.940	0.982	0.979	0.978
$a\exp(-kt)+(1-a)\exp(-kt)$	RMSE	0.696	0.917	0.626	0.457	0.714	0.817	0.511	0.573	0.828	0.649	0.614	0.650
	χ^2	0.0274	0.0119	0.0055	0.0020	0.0223	0.0085	0.0027	0.0041	0.0171	0.0044	0.0053	0.0059
Lewis	R^2	0.926	0.948	0.972	0.986	0.913	0.944	0.981	0.972	0.934	0.962	0.981	0.983
$\exp(-kt)$	RMSE	0.759	0.958	0.791	0.676	0.657	0.904	0.715	0.757	0.546	0.806	0.784	0.806
	χ^2	0.0274	0.0119	0.0055	0.0020	0.022	0.0085	0.0027	0.0041	0.0171	0.0044	0.0053	0.0059
Simplifed Fick's diffusion	R^2	0.899	0.95	0.981	0.994	0.912	0.966	0.992	0.987	0.923	0.984	0.984	0.981
$a\exp\left(-c\left(t/L^2\right)\right)$	RMSE	0.947	0.754	0.545	0.449	0.752	0.702	0.484	0.566	0.570	0.586	0.595	0.626
	χ^2	0.0258	0.0101	0.0044	0.0013	0.0219	0.0078	0.0017	0.0030	0.0183	0.0034	0.0036	0.0047
Logarithmic	R^2	0.944	0.974	0.981	0.989	0.946	0.974	0.986	0.977	0.947	0.981	0.973	0.967
$a\exp(-kt)+c$	RMSE	0.686	0.708	0.545	0.379	0.562	0.690	0.451	0.460	0.454	0.582	0.523	0.582
	χ^2	0.0139	0.0063	0.0043	0.0025	0.0131	0.0060	0.0030	0.0054	0.0125	0.0042	0.0063	0.0081
Midilli	R^2	0.991	0.998	0.998	0.999	0.992	0.997	0.999	0.998	0.992	0.998	0.999	0.994
$a\exp(-kt^n)+bt$	RMSE	0.713	0.427	0.316	0.259	0.668	0.406	0.311	0.270	0.620	0.405	0.313	0.167
	χ^2	0.0020	0.0003	0.0004	0.0001	0.0017	0.0006	0.0001	0.0002	0.0018	0.0002	0.0002	0.0012
Two Term Exponential	R^2	0.913	0.958	0.979	0.991	0.926	0.969	0.988	0.983	0.997	0.995	0.982	0.987
$a\exp(-kt)+(1-a)\exp(-kat)$	RMSE	0.696	0.917	0.626	0.457	0.714	0.817	0.511	0.573	0.840	0.578	0.612	0.636
	χ^2	0.0274	0.0119	0.0055	0.0020	0.0223	0.0085	0.0027	0.0041	0.0004	0.0011	0.0044	0.0033

activation function combinations showed the least fit.

Using regression analysis and the Minitab version, a correlation was created between moisture ratio, drying time, drying temperature, and air velocity [33,34]. Fig.5 shows the schematic representation of ANN model topology.

$$MR = 0.000349t^2 - 0.000005T^2 - 0.0131v^2 + 0.000058Tt + 0.000286tv + 0.000083Tv - 0.04195t - 0.00531T - 0.081v + 1.523 \quad (15)$$

Drying rate processing by ANN predictive modeling

The number of neurons in the input hidden layer was changed to determine the optimal number of processing elements. Several activation functions were used in the input hidden layer and output hidden layer. The number of processing elements and iterations (epoch) for each topology was recorded. After applying different ANN topologies to the testing data, it was found that the network with TANSIGMOID-TANSIGMOID activation function combinations and

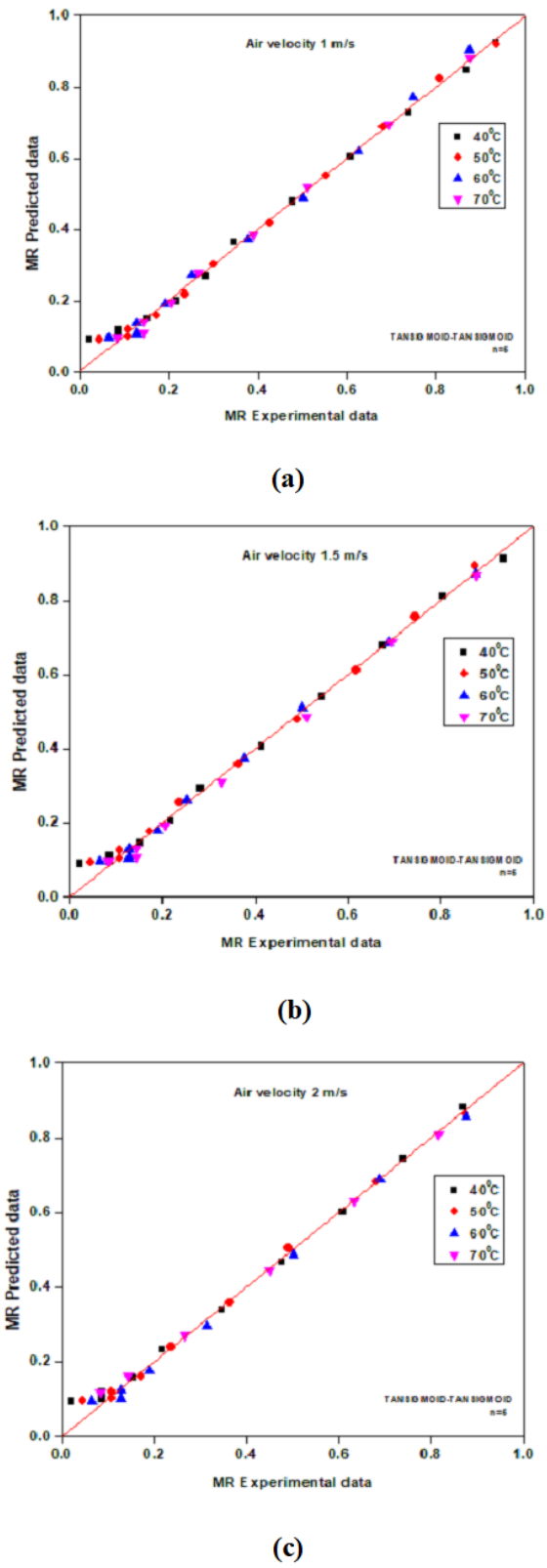

Figure 4. Comparison of experimental MR and predicted MR of ANN modeling using TANSIGMOID -TANSIGMOID activation function: (a) 1 m/s (b) 1.5 m/s (c) 2 m/s.

nine neurons in the input hidden layer produced the best results, with R^2, *RMSE*, and *MAE* values of 0.9696, 0.0916, and 0.0028 were in accordance with the range

reported in the literature, R^2 ranged from 0.981 to 0.999, *RMSE* ranged from 0.0333 to 0.1475, and *MAE* ranged from 0.05318 to 0.0088 [19,32].

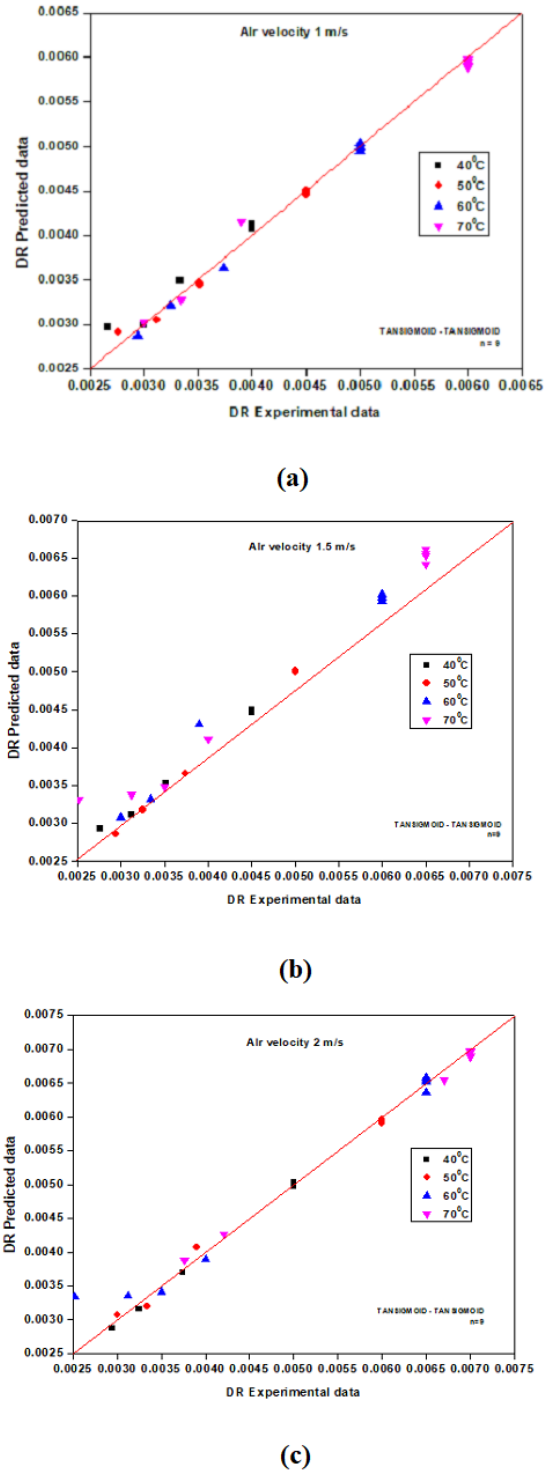

Figure 5. Comparison of experimental DR and predicted DR of ANN modeling using TANSIGMOID - TANSIGMOID activation function: (a) 1 m/s (b) 1.5 m/s (c) 2 m/s.

Similarly, the drying rate data predicted by the other models, most of the training, validation, and testing data points for TANSIGMOID-TANSIGMOID activation function combinations and nine neurons in

the input hidden layer were closer to the diagonal than for other combinations, indicating that the experimental and ANN outputs shown in Fig. 6 are the best fit. Eight neurons in the input hidden layer with TANSIGMOID - LOGSIGMOID activation function combinations have the least fit, whereas six neurons in the input hidden layer with TANSIGMOID - PURELIN activation function combinations have the reasonable fit. Using regression analysis, Minitab version.17 was used to build a correlation between drying rate, drying time, drying temperature, and air velocity.

$$DR = -0.000001t^2 - 0.000057v^2 - 0.000002tT - 0.000041tv - 0.000006Tv + 0.000126t + 0.000115T + 0.00214v - 0.00226 \quad (16)$$

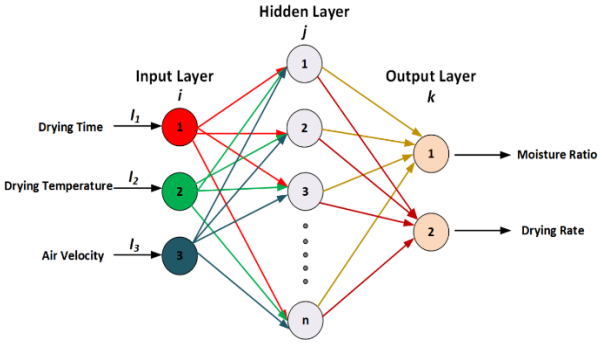

Figure 6. Schematic representation of ANN model.

ANN versus mathematical models

The twelve mathematical drying models had lower R^2 and higher *MSE* than the ANN (Table 4). The plot of experimental vs. predicted data (Fig. 4) and (Fig. 6) reveals that ANN accurately predicted the moisture ratio and drying rate for tray-dried paddy. Similarly, the independent of parameters used, the prediction capability of trained ANN was better than that of the investigated mathematical models, was reported by [35–38]. It is worth noting that the Midilli model was able to compete spiritedly with ANN's unique predictive capabilities, which were made possible by the lesser complexity of drying data. Fig. 7 shows a comparative analysis between different combinations of activation functions.

Determination of effective diffusivity

During the falling rate period, diffusion-controlled drying was investigated. It can be described by using Fick's diffusion equation [39,40]. Effective diffusivities of paddy for given temperatures and velocities were evaluated by Eq.(5). The effective diffusivity varied from 15.05 10^{-9} m^2/s to 28.5 10^{-9} m^2/s for paddy presented in Table 5. It was observed that the effective diffusivity was increased with the increased drying temperatures [41].

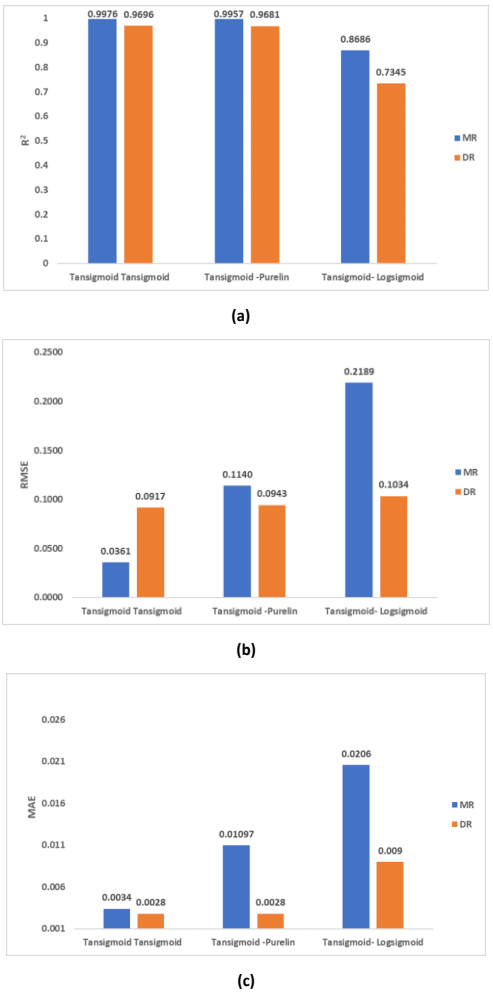

Figure 7. Comparative analysis between different combinations of activation functions: (a) R^2, (b) RMSE, (c) MAE.

Table 4. Comparative evaluation of ANN and selected semi-empirical model for a temperature range of (40–70) °C and air velocity range of (1–2) m/s.

Model	R^2	*MSE*
Midilli	0.991–0.999	0.028–0.508
ANN	0.9976	0.0013

However, no significant increment was observed due to increasing air velocities. Water evaporation occurred at the seed's surface, which was more immediately affected by temperature and velocity. Even with accelerated velocity and increasing temperature, the air had inadequate energy to release water molecules from the seed surface [42].

Effect of temperature on diffusivity

The activation energy was calculated from the slope of the Arrhenius plot, *ln(D)* versus *1/T*. The activation energy was evaluated to be 6.8 to 7.3 kJ/mol.

The majority of the water in paddy (like in other agricultural products) is bounded water. As a result, the drying process occurred at a falling rate. The drying and energy consumption rate increases with temperature and air velocity. If temperature increases, the water molecules gain more kinetic energy, leading to faster diffusion. The effect of temperature and air velocity on moisture diffusivity and activation energy in drying are shown in Table 6 [43].

Table 5. Effective diffusivity (m^2/s) at different temperatures and velocities.

Values	Air velocity, m/s											
	1				1.5				2			
	Temperature, °C											
	40	50	60	70	40	50	60	70	40	50	60	70
Slope	0.0524	0.0559	0.0614	0.0654	0.0711	0.0751	0.0795	0.0820	0.0782	0.0826	0.0868	0.0992
$D_{eff}10^{-9}$	15.05	16.06	17.62	18.81	20.43	21.58	22.86	23.56	22.47	23.72	24.93	28.50

Table 6. Data for diffusivity vs temperature.

	Air velocity, m/s											
	1				1.5				2			
1/T, 1/K	0.00319	0.00309	0.00300	0.00291	0.00319	0.00309	0.00300	0.00291	0.00319	0.00309	0.00300	0.00291
ln *D*	-18.01	-17.94	-17.85	-17.78	-17.70	-17.65	-17.59	-17.56	-17.61	-17.55	-17.50	-17.37
E_a, kJ	6.8				6.9				7.3			

CONCLUSION

Prediction of the drying kinetics of paddy was carried out using mathematical and ANN modeling. Specifically, twelve mathematical drying models and ANNs with different activation functions, such as TANSIGMOID, LOGSIGMOID, and PURELIN were evaluated. ANN models result in better prediction of drying kinetics. The accuracy level of the various activation functions was evaluated using model performance metrics. The following conclusions are made with the observed outcomes: ANN modeling attained exceptionally greater prediction accuracy than mathematical modeling based on the results of evaluation metrics. Among the three activation function, such as TANSIGMOID, LOGSIGMOID, and PURELIN, TANSIGMOID predicted the drying kinetics of paddy more precisely. R^2, *RMSE*, and *MAE*, performance metrics of ANN, showed a better scale of 0.9976, 0.0360, and 0.0034, respectively. Investigation of equilibrium moisture content revealed a direct relationship between relative humidity and drying temperature. It was observed that EMC and relative humidity increased as the temperature decreased.

REFERENCES

[1] M.R. Manikantan, P. Barnwal, R.K. Goyal, J. Food Sci. Technol. 51 (2014) 813–819. https://doi.org/10.1007/s13197-013-1250-1.

[2] S. Rajasekar, N. Meyyappan, D.G. Rao, ChemBioEng Rev. 4 (2017) 304–309. https://doi.org/10.1002/cben.201600018.

[3] O. Yaldýz, C. Ertekýn, Drying Technol. 19 (2001) 583–597. https://doi.org/10.1081/DRT-100103936.

[4] N. Norhadi, A.M. Akhir, N.R. Rosli, F. Mulana, Malaysian J. Chem.Eng. Technol. 3 (2020) 51–59. https://doi.org/10.24191/mjcet.v3i2.10965.

[5] R. Winiczenko, K. Górnicki, A. Kaleta, M. Janaszek-Mańkowska, Neural Comput. Appl. 30 (2018) 1795–1809. https://doi.org/10.1007/s00521-016-2801-y.

[6] V.K. Chasiotis, D.A. Tzempelikos, A.E. Filios, K.P. Moustris, Comput. Electron. Agric. 172 (2020). https://doi.org/10.1016/j.compag.2019.105074.

[7] M. Golmohammadi, M. Foroughi-dahr, M. R. Hamaneh, A. Reza, S. Jalaledin, Iran. J. Chem. Chem. Eng. 35 (2016) 105–117. https://doi.org/10.30492/IJCCE.2016.22064.

[8] S. Chakraborty, M. Sarma, J. Bora, S. Faisal, M.K. Hazarika, Agric. Eng. Int. 18 (2016) 177–189. https://cigrjournal.org/index.php/Ejounral/article/view/3645/2477.

[9] A.D. Arjun, S. Ganapathy, T. Pandiarajan, K. Bhuvaneswari, M. Duraisamy, Int. J. Agric. Eng. 10 (2017) 623–630. https://doi.org/10.15740/HAS/IJAE/10.2/623-630.

[10] M. Beigi, M. Torki-Harchegani, M. Mahmoodi-Eshkaftaki, Chem. Ind. Chem. Eng. Q. 23 (2017) 251–258. https://doi.org/10.2298/CICEQ160524039B.

[11] J. Zhang, P. Ma, X. Zhang, B. Wang, J. Wu, X. Xing, J. Therm. Anal. Calorim. 134 (2018) 2359–2365. https://doi.org/10.1007/s10973-018-7716-7.

[12] B. Pattanayak, S.S. Mohapatra, H.C. Das, Int. J. Postharvest Technol. Innov 6 (2019) 162–178. https://doi.org/10.1504/IJPTI.2019.106194.

[13] E. Taghinezhad, A. Szumny, M. Kaveh, V.R. Sharabiani, A. Kumar, N. Shimizu, Foods 9 (2020) 1–17.

https://doi.org/10.3390/foods9010086.

[14] A. Sitorus, Novrinaldi, S.A. Putra, I.S. Cebro, R. Bulan, Case Stud. Therm. Eng. 28 (2021) 1–9. https://doi.org/10.1016/j.csite.2021.101572.

[15] S. Chakraborty, S.P. Gautam, M. Sarma, M.K. Hazarika, Food Sci. Technol. Int. 27 (2021) 746–763. https://doi.org/10.1177/1082013220983953.

[16] M. Lutovska, V. Mitrevski, I. Pavkov, M. Babic, V. Mijakovski, T. Geramitcioski, Z. Stamenkovic, J. Process. Energy Agric. 21 (2017) 91–96. https://scindeks.ceon.rs/article.aspx?artid=1821-44871702091L.

[17] D.G. Rao, B.S. Sridhar, G. Nanjundaiah, J. Food Eng. 17 (1992) 49–58. https://doi.org/10.1016/0260-8774(92)90064-D.

[18] M. Ahmet Tütüncü, T.P. Labuza, J. Food Eng. 30 (1996) 433–447. https://doi.org/10.1016/S0260-8774(96)00028-3.

[19] T. Gunhan, V. Demir, E. Hancioglu, A. Hepbasli, Energy Convers. Manage. 46 (2005) 1667–1679. https://doi.org/doi:10.1016/j.enconman.2004.10.001.

[20] R.L. Sawhney, P.N. Sarsavadia, D.R. Pangavhane, S.P. Singh, Drying Technol. 17 (1999) 299–315. https://doi.org/10.1080/07373939908917531.

[21] A. Tarafdar, N. Jothi, B.P. Kaur, J. Appl. Res. Med. Aromat. Plants 24 (2021) 1–8. https://doi.org/10.1016/j.jarmap.2021.100306.

[22] G.O. Ondier, T.J. Siebenmorgen, R.C. Bautista, A. Mauromoustakos, Trans. ASABE. 50 (2011) 1007–1013. https://doi.org/10.13031/2013.37085.

[23] J.O. Ojediran, A.O. Raji, Int. Food Res. J. 17 (2010) 1095–1106. http://www.ifrj.upm.edu.my/17%20(04)%202010/(30)%20IFRJ-2010-042%20Raji%20Nigeria[1].pdf.

[24] V.C. Siqueira, R.A. Leite, G.A. Mabasso, E.A.S. Martins, W.D. Quequeto, E.P. Isquierdo, Cienc. Agrotecnol. 44 (2020) 1–10. https://doi.org/10.1590/1413-7054202044011320.

[25] S. Rafiee, A. Keyhani, A. Jafari, Int. J. Food Prop. 11 (2008) 223–232. https://doi.org/10.1080/10942910701291858.

[26] B.H. Hassan, A.I. Hobani, J. Food Process Eng. 23 (2000) 177–189. https://doi.org/10.1111/j.1745-4530.2000.tb00510.x.

[27] I.L. Pardeshi, S. Arora, P.A. Borker, Drying Technol. 27 (2009) 288–295. https://doi.org/10.1080/07373930802606451.

[28] N.A. Akgun, I. Doymaz, J. Food Eng. 68 (2005) 455–461. https://doi.org/10.1016/j.jfoodeng.2004.06.023.

[29] Xiao-Kang Yi, Wen-Fu Wu, Ya-Qiu Zhang, Jun-Xing Li, Hua-Ping Luo, Math. Probl. Eng. (2012) 1–19. https://doi.org/10.1155/2012/386214.

[30] Y.G. Keneni, A.K. (Trine) Hvoslef-Eide, J.M. Marchetti , Ind. Crops Prod. 132 (2019) 12–20. https://doi.org/10.1016/j.indcrop.2019.02.012.

[31] Qing-An Zhang, Yun Song, Xi Wang, Wu-Qi Zhao, Xue-Hui Fan, CYTA J. Food 14 (2016) 509–517. https://doi.org/10.1080/19476337.2015.1136843.

[32] S. Soodmand-Moghaddam, M. Sharifi, H. Zareiforoush, H. Mobli, Qual. Assur. Saf. Crop.12 (2020) 57–66. https://doi.org/10.15586/QAS2019.658.

[33] P. Thant, P. Robi, P. Mahanta, Int. J. Eng. Appl. Sci. 5 (2018) 118–123. https://www.ijeas.org/download_data/IJEAS0503034.pdf.

[34] A. Sitorus, Novrinaldi, S.A. Putra, I.S. Cebro, R. Bulan, Case Stud. Therm. Eng. 28 (2021). https://doi.org/10.1016/j.csite.2021.101572.

[35] S. Kono, I. Kawamura, T. Araki, Y. Sagara, Int. J. Refrig. 65 (2016) 218–227. https://doi.org/10.1016/j.ijrefrig.2015.10.009.

[36] B. Osodo, D. Nyaanga, J. Kiplagat, J. Muguthu, Am. J. Food Technol. 6 (2018) 263–271. http://pubs.sciepub.com/ajfst/6/6/6/.

[37] M. Kashiri, A.D. Garmakhany, A.A. Dehghani, Qual. Assur. Saf. Crop. Foods 4 (2012) 179–184. https://doi.org/10.1111/j.1757-837X.2012.00184.x.

[38] I. Golpour, R. Amiri Chayjan, J. Amiri Parian, J. Khazaei, J. Agric. Sci. Technol. 17 (2015) 287–298. https://jast.modares.ac.ir/article-23-10165-en.pdf.

[39] U. Şahin, H.K. Öztürk, J. Food Process Eng. 41 (2018) 1–14. https://doi.org/10.1111/jfpe.12804.

[40] J.W. Bai, H.W. Xiao, H. L. Ma, C.S. Zhou, J. Food Qual. (2018) 1–9. https://doi.org/10.1155/2018/3278595.

[41] M. Garg, S. Sharma, S. Varmani, S. Sadhu, Int. J. Food Sci. Nutr. 3 (2014) 61–66. https://www.researchgate.net/publication/341440997_DRYING_KINETICS_OF_THIN_LAYER_PEA_PODS_USING_TRAY_DRYING#fullTextFileContent.

[42] A. Motevali, S. Younji, R.A. Chayjan, N. Aghilinategh, A. Banakar, Int. Agrophys. 27 (2013) 39–47. https://doi.org/10.2478/v10247-012-0066-y.

[43] A. Fernandez, C. Román, G. Mazza, R. Rodriguez, Case Stud. Therm. Eng. 12(2018) 248–257. https://doi.org/10.1016/j.csite.2018.04.015.

RAJASEKAR SUBRAMANYAM
MEYYAPPAN NARAYANAN

Department of Chemical Engineering, Sri Venkateswara College of Engineering, Tamil Nadu, India

NAUČNI RAD

MODELOVANJE KINETIKE SUŠENJE PIRINČA U SUŠARI SA TAVAMA VEŠTAČKOM NEURONSKOM MREŽOM

Proučavanje kinetike sušenja i karakteristika poljoprivrednih proizvoda je od suštinskog značaja za procenu vremena sušenja, projektovanje sušara i optimizaciju procesa sušenja. Difuzivnost vlage u različitim uslovima sušenja je ključna za projektovanje procesa i opreme. Kinetika sušenja pirinča u sušari sa tavama je modelovana korišćenjem veštačke neuronske mreže (ANN). Levenberg-Markuardt (LM) algoritam za obuku sa funkcijama aktivacije skrivenog sloja TANSIGMOID i TANSIGMOID dao je superiorne rezultate u predviđanju odnosa vlage i brzine sušenja. Takođe, izvršena je komparativna procena prediktivnih sposobnosti ANN i 12 različitih matematičkih modela sušenja. Midilijev (Midillijev) model adekvatno opisuje eksperimentalne podatke sa vrednošću koeficijenta determinacije R^2 koja uporediva sa vrednošću za ANN. Međutim, RMSE za ANN (0,0360) je značajno niži od onog kod Midilijevog modela (0,167 do 0,712). Efektivna difuzivnost vlage se povećava sa porastom temperature sa 15,05 x 10^{-9} m^2/s na 28,5 x 10^{-9} m^2/s. Energija aktivacije za sušenje zrna pirinča varirala je između 6,8 kJ/mol i 7,3 kJ/mol, što je pokazalo umerenu potrebu za energijom za difuziju vlage.

Ključne reči: sušara sa tavama, ravnotežni sadržaj vlage, matematičko modelovanje, ANN modelovanje, efektivna difuzivnost, energija aktivacije.

CI&CEQ
Chemical Industry & Chemical Engineering Quarterly

Available online at
Association of the Chemical Engineers of Serbia AChE
www.ache.org.rs/CICEQ

Chem. Ind. Chem. Eng. Q. 29 (2) 99–109 (2023) CI&CEQ

VOJO JOVANOV[1]
SNEŽANA VUČETIĆ[2]
SINIŠA MARKOV[2]
BILJANA ANGJUSHEVA[1]
EMILIJA FIDANCEVSKA[1]
JONJAUA RANOGAJEC[2]

[1]Ss. Cyril and Methodius University in Skopje, Faculty of Technology and Metallurgy, Skopje, Republic of North Macedonia

[2]University of Novi Sad, Faculty of Technology, Novi Sad, Serbia

RESISTANCE TO FROST ACTION AND MICROBIOLOGICAL CORROSION OF NOVEL CERAMIC COMPOSITES

Article Highlights

- The incorporation of fly ash in producing more sustainable ceramic products
- Prediction of frost action mechanisms on ceramic compacts and biocorrosion resistance
- Utilization of fly ash in ceramic composites without significant deteriorating effect

Abstract

This work illustrates the prediction of frost action mechanisms on ceramic compacts and their biocorrosion resistance to fungus action. The ceramic compacts were produced from two raw materials: coal fly ash (40 wt.%) and clay material (60 wt.%). The ceramics models were made in laboratory conditions by pressing (P = 45 MPa), drying (105 °C, 3h), and sintering (1100 °C, 1 h; heating rates 3 °C/min and 10 °C/min.). The mechanisms responsible for the deterioration of the designed ceramic compacts were defined based on the values of the total porosity, pore size distribution, pore critical radius, and the Maage factor, as well as on the values of water permeability. The biocorrosion process was investigated using Aspergillus niger fungus as a model microorganism. The different degrees of fungus colonization on the designed compacts were comparatively analyzed based on the Scanning Electron Microscopy investigation results. The gained results are encouraging as they show that the utilization of fly ash (40 wt.%) in ceramic composites is possible without significant deterioration of their durability (frost action and microbiological corrosion resistance) compared with the ones whose production was based only on clay material.

Keywords: waste treatment, fly ash, ceramic, weathering, pore size distribution, thermal analysis.

SCIENTIFIC PAPER

UDC 666.3/.7:620.193.2

One type of waste material with a high potential for the production of ceramic materials is fly ash, a by-product of coal combustion in thermal power plants [1]. As a waste material, fly ash is often stored in landfills, presenting a major source of environmental pollution in the form of dust and toxic substances, such as heavy metals and sulphur compounds. However, the ashes mostly contain particles with dimensions of (50–100) μm; therefore, no extra milling is needed. The application of fly ashes as industrial wastes from coal combustion in thermal power plants, the cement industry, road base construction, and agriculture is well known [2, 3]. The potential use of this secondary raw material in the building and construction industry minimizes the ecological footprint of this sector. In addition, it reduces the pressure on using primary raw materials such as clay materials, quartz sand, and carbonates. It contributes to the transition towards a more resource-efficient and sustainable world.

The growing interest in environmental protection shows an increasing need to utilize fly ash in producing new materials and for other reuses [4, 5]. Due to envi-

Correspondence: V. Jovanov, Ss. Cyril and Methodius University in Skopje, Faculty of Technology and Metallurgy, Rudjer Boskovic 16, 1000 Skopje, Republic of North Macedonia.
E-mail: vojo@tmf.ukim.edu.mk
Paper received: 4 September, 2021
Paper revised: 29 Jun, 2022
Paper accepted: 21 July, 2022

https://doi.org/10.2298/CICEQ210904016J

ronmental issues, price volatility, supply chain, and pressure on valuable resources have compelled companies to look for alternative and sustainable materials and energy supplies. According to the Ellen MacArthur Foundation, "a circular economy is restorative and regenerative by design and aims to keep products, components, and materials at their highest utility and value at all times, distinguishing between technical and biological cycles" [6].

Many studies have been published regarding the benefits of fly ash as a component of the raw material composition in the production of ceramic composites [7–9]. Still, the frost and microbiological resistance of the composite ceramic materials based on fly ash have not met with the same interest and attention.

Weathering is a group of processes that leads to the decay or degradation of materials upon their exposure to surrounding environmental conditions [10]. The most dominant factors regarding the environmental damage of buildings, more precisely those with ceramic materials as their constitutive parts, are moisture, atmospheric pollution, and the presence of soluble salts and microorganisms. Even the most durable materials could be modified and ruined due to the deposition of dust and, consequently, the action of microorganisms, such as cyanobacteria, fungi, and algae [11]. It is well known that the textural properties, especially the pore size distribution and the values of the total porosity, and the mechanical properties of ceramic materials are of great interest for application in real environmental conditions [12].

In many ceramic applications, there is a growing need to predict the service life of the products based on laboratory tests. Many scientists and science groups have been working on analyzing the factors that influence ceramic materials' weathering and developing models to predict the aging of ceramic building materials (frost resistance and biocorrosion). Maage [13,14], Franke and Bentrup [15], Koroth *et al*. [16], Robinson [17], and Vincenzini [18] elaborated different models which refer to technological properties: water absorption in different outdoor conditions or textural properties (total porosity, size and specific surface of pores). They gave modeling equations based on which the frost resistance of materials could be predicted.

Porous ceramic materials in their structure always contain some quantity of moisture, i.e., of physically bound water. The presence of this water directly affects the physical-mechanical properties of ceramic materials, such as strength, shrinkage/expansion, water vapor transmission, and resistance to external conditions (resistance to frost action, soluble salts, and microorganisms). The capacity of materials to accumulate moisture within the porous system is one of the basic parameters that influence their durability and use as building materials. Namely, the existing stress in the material, when the temperature falls below 0 °C, is generated during the conversion of water into ice, leading to the formation of micro-cracks whose extent can overcome the mechanical resistance of the material, later promote inevitable damages. The material's compressive strength is directly related to textural properties and indirectly related to the frost resistance of materials [19].

The knowledge about the development and action of the defined frost action mechanism (closed container, hydraulic pressure, and micro ice lens mechanism) gives the possibility to predict the durability of building materials during the frost action.

The mechanism of a closed container [20] can be simply explained if the ceramic materials can be considered as closed system from which no water enters or leaves. In such a case, the mechanism of destruction caused by the increase of the ice volume becomes dominant due to the phase transformation of the water-ice, which is accompanied by an increase of the volume by 9%. Also, the physical size of the representative samples for this mechanism should be so small that the influence of the temperature gradient to destroy the samples can be neglected. The water saturation and the lack of air-filled pores determine the presence of this mechanism. When a porous network is partly saturated, some porosity remains occupied by air, and ice can extrude toward these trapped air gaps without creating any pressure on the porous medium. This paper determines the susceptibility to this mechanism by the number of pores with a radius smaller than 0.1 μm. With water suction availability, these pores are responsible for high water saturation causing larger expansion.

The mechanism of hydraulic pressure [20] appears when the temperature gradient cannot be neglected, as in the case of a rapid temperature drop. According to this mechanism, ice is initially formed on the surface of the samples, where the temperature is the lowest. Then, the water that does not freeze in the pores with a small radius is pressed over time under hydraulic pressure and moves through the capillary and gel pores, partially filled with ice, in the bulk of the sample. The response of the samples to this mechanism depends on the rate of ice formation (determined by the rate of freezing, total porosity, pore size distribution, and width of the pore size distribution), permeability, and the maximum distance that water has to pass until it reaches the air pore (both of which is determined by pore size distribution).

The ice-lens mechanism [20] occurs when there

is a lower freezing rate and a longer freezing period. As a result, a balance between frozen and unfrozen water is established in larger and smaller pores, respectively. As a result of this mechanism, non-frozen water has more free energy than ice and moves through a pore system to the ice crystals participating in their growth. As a result, the ice, shaped like a lens (hence the name of the mechanism), grows and can cause pressure on the walls of the pores and lead to the deterioration of the material.

Although frost damage is mostly a physical process, the action of microorganisms (biocorrosion) implies several physical and chemical changes in the material caused by their metabolic activity. Physical degradation is caused by penetration, pressure, and dimensional growth of biological structures within materials. In contrast, chemical degradation is brought by the excretion of metabolic intermediates or the end products of metabolism that could have hindering or very aggressive roles. Apart from these causes, chemical degradation can also be a consequence of the process of assimilation, when microorganisms, using a mediator (water), use the material as food and energy source for enzymatic activities or ionic transfer [24].

The biocorrosion phenomenon of ceramic building materials causes structural, esthetical, and economic issues, and it strongly influences the final products' chemical and physical properties, functionality, and durability. All the mentioned facts present a good basis for research dedicated to biocorrosion resistance and the application of ceramic products in real environmental conditions [22]. Colonizing roofing tiles by organisms is progressive, heterogeneous, and slow. On the other hand, laboratory assessment of this phenomenon requires a procedure that could be conducted within a reasonable period of time. Bearing that the lichens are a major causative agent of bio-deterioration of ceramic materials, the fungus *Aspergillus niger* (*A. niger*), as a possible symbiotic partner for lichen formation, could be very useful for the laboratory colonization of the clay roofing tiles. *A. niger* fungus is the most common species of the genus *Aspergillus*, and it belongs to the saprotrophic fungi that live on inorganic substrates. This fungus is most commonly found in oxygen-rich environments where it grows on the surface of the substrate. Fungi usually grow on carbonate-rich substrates or in wet places (walls, bricks, tiles), but they can also grow in carbonate-deficient environments [23]. Water availability and physical properties, such as porosity, roughness, and substrate surface temperature, strongly impact microbiological growth. Still, no correlation has been found between the raw material characteristics and phototropic growth [24].

Considering that numerous studies have been published concerning the benefits of fly ash utilization in the production of ceramic composites and that frost resistance and microbiological corrosion have not received the same attention, our work aimed to examine the durability of composites based on fly ash and clay materials. For that purpose, was used the novel ceramic composite composed of 60 wt.% clay and 40 wt.% fly ash sintered at 1100 °C/1h, which was found as optimal in our previous work [25], where fly ash content and the sintering temperature varied from 10 wt.% to 90 wt.% and from 900 °C/1h to 1100 °C/1h, respectively. Bearing in mind all the mentioned facts, the experimental investigation presented in this work was performed by combining the exploitation capacity (resistance to freezing cycles and microbiological corrosion) and the characteristics of the novel ceramic product, i.e., its microstructural, textural, and physical-mechanical properties.

MATERIAL AND METHODS

It is a well-known fact that the mechanical properties of ceramics are very important in determining their application for any specific function. This property, together with the porosity of ceramics, is an important factor considering resistance to freezing temperatures. Bearing in mind this relationship, the idea of our work was to estimate the dominant deterioration mechanism regarding frost and biocorrosion actions of the novel ceramic composites, found as optimal in previous work [25], where a significant part of the clay material (40 wt.%) was replaced with fly ash. A detailed characterization of raw materials (clay and fly ash) and the porous final product was performed.

Material

The raw materials used for the performed investigation were: fly ash from the thermal power plant REK Bitola, Republic of North Macedonia, and clay material from a region near Bitola, Republic of North Macedonia. Production parameters of the novel ceramic composites, as well as of the ones prepared only from clay materials/fly ash, were the following: (1) fly ash content in the investigated composites was 40 wt.%; (2) particles size of the used raw materials (clay and fly ash) was less than 63 μm; (3) processing parameters: pressing parameter of the compacts was 45 MPa (uniaxial press, Weber Pressen KIP 100), and polyvinyl alcohol (PVA) was used as a plasticizer; the drying process was done in laboratory conditions at 105 °C for 3 h until the mass of the compacts was constant; (4) sintering process was performed in a laboratory electric furnace under the following conditions:

sintering temperature was 1100 °C for 1 h (air atmosphere) while the heating rates were 3 °C/min and 10 °C/min.

Six different systems were produced to investigate the influence of fly ash on the characteristics of ceramic composites: (1) the first system of novel ceramic composites (40 wt.% fly ash and 60 wt.% of clay) was sintered with the heating rate of 3 °C/min; (2) the second system was designed with the same raw materials, but sintered with the heating rate of 10 °C/min; (3) and (4) systems based only on the clay material sintered with two different heating rates of 3 °C/min and 10 °C/min; (5) and (6) systems based only on the fly ash material, sintered with two different heating rates of 3 °C/min and 10 °C/min.

Methods

The mineralogical composition of the raw materials, as well as of the novel ceramic composites, was determined by X-ray powder diffraction (XRD) analysis (model PW 1710, Philips, Germany) under the following experimental conditions: monochromatic CuKα radiation with λ=1.54178 Å wavelength in the 5–55° of 2θ range, scan rate 0.02°, 0.5 s per step.

The chemical composition of the raw materials was determined by an X-Ray Fluorescence Spectroscope, model ARL 9900XP, USA.

Water absorption of the sintered samples was determined from the difference between the total dry mass, mdry, and the surface dry mass, msur.dry, after their immersion in water (19 °C). The bulk density value was determined by the water displacement method according to EN-993. Finally, the total porosity of the samples was calculated from the results of the relative density values.

The mechanical properties, i.e., bending strength and E-modulus of the produced novel ceramic composite, are determined using a three-point bending tester (Netzsh 401/3, Germany) with a 30 mm span and a 0.5 mm/min loading rate. Furthermore, the compressive strength tests were carried out using an Instron testing machine (model 1126, Germany) with a crosshead speed of 0.5 mm/min.

The frost resistance investigation was conveyed through mercury (Hg) intrusion porosimetry: total porosity, pore size distribution, pore critical radius values, and Maage factor [26]. Hg porosimetry of the final compacts was conducted using an AutoPore IV 9500 device (Micromeritics, USA), with the possibility of achieving the pressure up to 33,000 psi (228 MPa), which enables measurement of pore radius ranging from 360 μm to 0.001 μm. In addition, the low-temperature nitrogen adsorption method (ASAP Micrometrics, US model 2000) was used to determine surface area, pore volume, the surface area of pores, and the percentage of pores smaller than 20 nm.

Low-temperature dilatation measurements were done using a Thermo Mechanical Analyzer (Model 981, Du Pont, USA) to simulate the relatively low-temperature behavior of the same ceramic composite's dried and water-saturated samples materials. These measurements were performed in the temperature interval of -40 °C up to +40 °C (thawing rate was 10 C/min). The desired low temperature (-40 °C) was achieved by holding the samples in liquid nitrogen for a defined time.

The microbiological corrosion was later artificially induced on the novel ceramic composite, which stood out as the most frost-resistant product. Finally, the biocorrosion process was performed in laboratory conditions using *A. niger* fungus. This approach was chosen based on: (1) our previous work dedicated to biocorrosion resistance of clay roofing tiles [27] and (2) the fact that the lichen, as a symbiotic life form of fungus and alga/cyanobacteria, is a major causative agent of bio-deterioration of ceramic materials [28].

The ceramic compacts were put in a sterile Petri dish. On the top surface of the ceramic models, a drop of the suspension (0.05 ml) of the *A. niger* fungus spore, with a concentration of 1.105 CFU/ml (Colony-forming units/milliliters), was added. Malt broth was used as a medium in which the spores were suspended. The specimens were submerged to a certain level in distilled water. The experiment was conducted over one month. The samples were sterilized in an autoclave with time, temperature, and pressure relation of 15 min, 121 °C, and 1.1 bar, respectively, then submerged to a certain level in distilled water to maintain humidity and exclude other environmental influences. The period of a month was chosen as long enough for the incubation of the fungus. This experiment was based on the fact that lichen is a symbiotic life form between a fungus and an alga or cyanobacteria, excreting organic acids while metabolizing the inorganic compounds of the ceramic system. The acidotic and complexing activity shown by the lichens was due to the fungal component of this symbiotic association. The degree of fungal colonization on the novel ceramic composite was comparatively analyzed with the colonization of the same fungus on the pure compacts of clay and fly ash using SEM (JEOL JSM-6460LV Scanning Electron Microscope). Before applying the spores, a number of incisions were made on the surface of the compacts, which were later used for breaking the compacts to perform SEM analysis of the cross-section to analyze the penetration of the fungus hyphae inside the compacts.

RESULTS AND DISCUSSION

Raw materials characterization

The raw materials were characterized in terms of their phase and chemical composition.

Phase composition

The XRD pattern of the fly ash (Figure 1) confirmed the presence of an amorphous phase and the following minerals: quartz, anorthite, hematite, albite, diopside, and anhydrite. In addition, the clay material used contained the following major mineral composition: quartz, feldspar, aragonite, chlorite, and calcite.

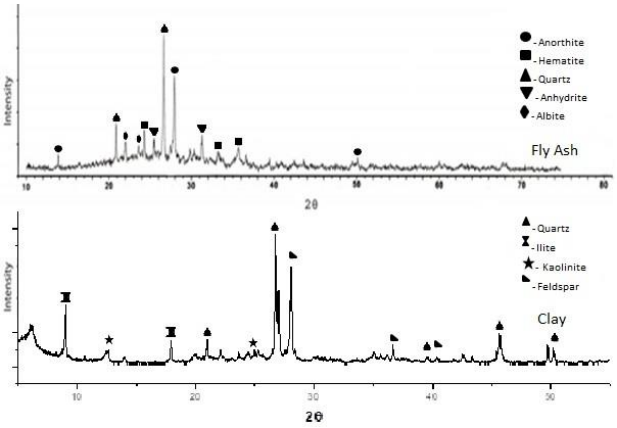

Figure 1. XRD profiles of raw materials.

Chemical composition and loss on ignition

The chemical composition (in terms of oxides) of the fly ash and the clay material is shown in Table 1. In both raw materials, there was a dominant presence of SiO_2, Al_2O_3, Fe_2O_3, and CaO. The fly ash, based on the content of SO_3, MnO, and P_2O_5, is an ecologically risky material, as already mentioned in the introduction part (pollution of surrounding areas in the form of dust and toxic substances, such as heavy metals and sulfur compounds). The identified loss on ignition (LOI) in the case of fly ash is related to the existence of unburned and partially burned coal particles.

Characterization of novel ceramic composite

XRD of novel ceramic composite

The phase composition of the novel ceramic composites, Fig. 2, based on fly ash and clay material, shows that the sintering process reduces the intensity of quartz and anhydrite peaks and promotes the formation of anorthite and diopside crystal phases. No significant differences exist in the phase composition of the samples sintered at the same sintering temperature (1100 °C) with different heating rates (3 °C/min vs. 10 °C/min). The relatively high content of CaO present in the fly ash and the clay material is the most likely reason for forming an anorthite crystal phase. Diopside [$Ca(Mg,Al)(Si,Al)_2O_6$], identified in the case of both

Table 1. Chemical composition of the fly ash and the clay material.

Oxide	SiO_2	TiO_2	Al_2O_3	Fe_2O_3	CaO	MgO	Na_2O	K_2O	MnO	P_2O_5	ZnO	PbO	SO_3	LOI	Σ
Fly ash	52.38	0.09	23.61	7.31	7.42	2.11	0.9	1.67	0.03	0.08	0.01	0.03	1.2	3.12	99.94
Clay	58.48		19.8	7.44	6.18	1.43	2.1	2.51						2.05	99.99

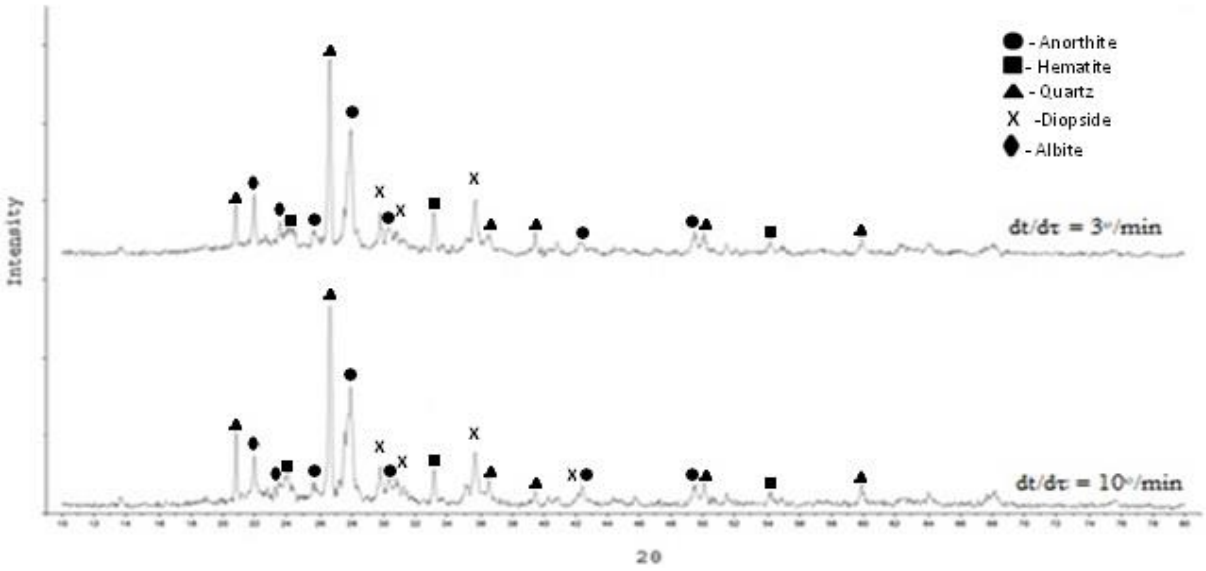

Figure 2. Diffractograms of novel ceramic composite.

systems, displays good resistance to frost action [29] due to the intercalation of its crystals. Therefore, the idea for future research is to encourage the formation of this crystalline phase.

Microstructural analysis

The SEM images of the novel ceramic composite sintered with different heating rates are given in Fig 3a (3 °C/min) and Fig 3b (10 °C/min). More closed micro pores and fewer larger pores were detected in the sample sintered with a heating rate of 10 °C/min. Therefore, this model seems to be more compact.

Physical and mechanical properties of the novel ceramic composites

It is well known that variations of physical and mechanical properties are related to sintering conditions used to obtain the desired microstructure of the samples. A dense microstructure is preferred when the produced composite is intended to resist weathering processes [30–32].

The physical and mechanical properties of the sintered models, Table 2, are a function of the sintering heating rate. The density value increased with the heating rate and vice-versa. On the other hand, a slight drop in the density value and increased porosity of the novel ceramic composite was noticed when the heating rate was reduced from 10°/min to 3°/min. These phenomena seemed to be caused by the expansion of the trapped gases during the sintering process.

According to the results in Table 2, the utilization of fly ash (40 wt.%) had a negative impact on mechanical properties and water absorption of the novel ceramic composite compared with the systems produced with 100 wt.% clay. Despite this, the values of the physical and mechanical properties of the novel composites were still solid enough for their potential application as bricks and tiles [33].

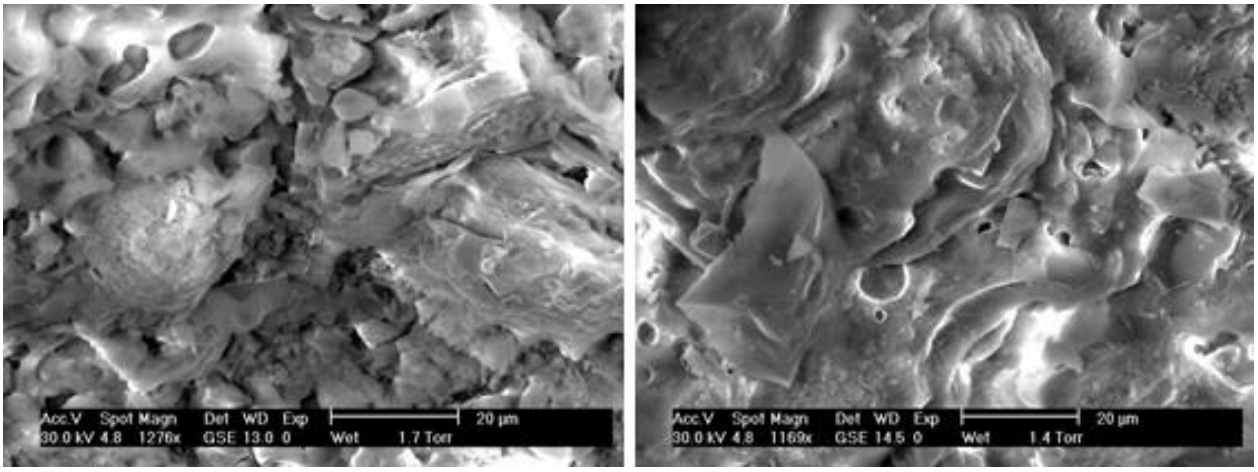

Figure 3. SEM photos of the novel ceramic composites.

Table 2. Physical and mechanical properties of the ceramic composites.

Composite	Heating rate, °C/min	Density, g/cm^3	Water porosity under the vacuum, %	Water absorption, %	Compressive strength, MPa	Bending strength, MPa	E-modulus, GPa
Novel ceramic composites	3	2.009	18.91	9.93	85.47	44.09	21.65
	10	2.089	15.70	7.02	100.01	50.47	25.35
100 % fly ash	3	1.41	38.13	25.45	10.38	11.92	5.88
	10	1.44	36.82	23.77	21.24	14.01	7.22
100 % clay	3	2.45	6.25	3.15	240.00	80.02	31.23
	10	2.47	5.43	0.34	285.00	90.00	34.12

Textural characterization

Hg porosimetry values

Based on the values of Hg porosimetry measurements, Figures 4 and Table 3, it is evident that the values of pore size distribution were significantly affected by the sintering heating rate. The samples sintered with the heating rate of 10 °/min have a

broader range of pore-size distribution, Figure 4.

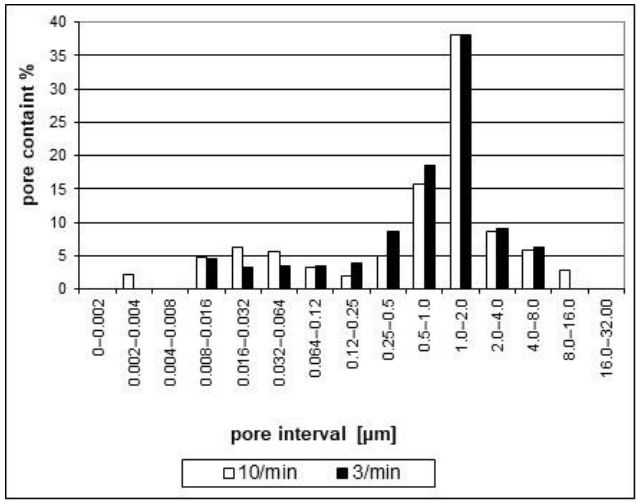

Figure 4. Pore size distribution of the composites based on fly ash and clay material sintered with respective heating rates.

The average total porosity determined by the mercury intrusion technique, Table 3, differs from the values of the total porosity measured by water absorption under vacuum. It is due to the difference between the two techniques covering different pore size intervals. Nevertheless, the total porosity was increased in both cases by lowering the heating rate from 10 °C /min to 3 °C /min.

The results of Hg porosimetry and the microstructural characteristics were used as parameters for predicting the ceramic models' frost action durability and determining the dominant frost action mechanisms [30–32]. The main parameters for this type of prediction are presented in Table 3.

The samples sintered at a lower heating rate (3 °C/min) showed different microstructural and textural properties than those sintered at (10 °C /min). It is the consequence of the microstructural heterogeneity of

Table 3. Total porosity, pore size fractions, dominant pore interval, scatter coefficient, Critical pore radius, Maage factor.

Heating rate, °C/min	Total porosity vol, %	Pore size fraction (r<0,1 µm) vol, %	Pore size fraction (r>3 µm vol, %	Dominant pore interval, µm	Scatter coefficient Cd	Critical pore radius, µm	Maage factor
3	17.29	10.4	23.55	1–2	1.28	2.83	82.45
10	10.51	16.1	17.8	1–2	1.62	3.42	58.5

the green compacts, more precisely, due to the mixture of two different mineralogical raw materials. The heating rate of 3 °C/min influenced the reduction of the quantity of smaller pores (r<0.1 µm) and consequently caused the increase of the quantity of larger pores (r>3 µm), Table 3. The obtained textural and microstructure features, with a significant quantity of glass phase (Figure 3), positively influenced the resistance of the products to freezing temperatures (Magee factor is 82.45) but negatively affected the mechanical characteristics (Compressive strength values), Table 2.

As the composites, sintered at a heating rate of 10 °C/min, had a higher fraction of capillary pores (the number of pores with radius < 0.1 µm), it is evident that the closed container mechanism was adequate for this type of product.

The value of the scatter coefficient (Cd parameter) for the ceramic models sintered at 3 °C/min was smaller than that for the ceramics sintered at 10 °C/min. It means that a narrower pore size distribution and, consequently, greater sensitivity of the products to the hydraulic pressure mechanism was obtained for the models sintered with a lower heating rate (3 °C/min).

In terms of critical pore radius, the novel ceramics sintered with 10 °C/min had a larger critical pore radius value, which means that this system should have greater permeability and a lower possibility of the hydraulic pressure mechanism to be anticipated as the dominant mechanism of deterioration. This conclusion correlates well with the prediction of frost resistance based on the scatter coefficient, Table 3.

The volume (%) of pores larger than 3 µm signifies the existence of air-filled parts in the ceramic systems. Namely, these pores are large enough to facilitate the passage of water from smaller to larger pores without affecting disruptive pressures and positively influencing the Maage criteria. Therefore, in accordance with the Maage factor, the composite ceramics sintered at 3 °C /min are more frost resistant than the ones sintered at 10 °C /min.

Results of low-temperature nitrogen adsorption

The distribution of the pores smaller than 150 nm in diameter for both ceramic products is presented in Figure 5, while in Table 4, the following values are presented: specific surface area of the materials and the pores; specific pore volume; average pore diameter and percentage of the pores smaller than 20 nm in diameter.

The samples sintered with 10 °C /min had a smaller average diameter and a greater fraction of the

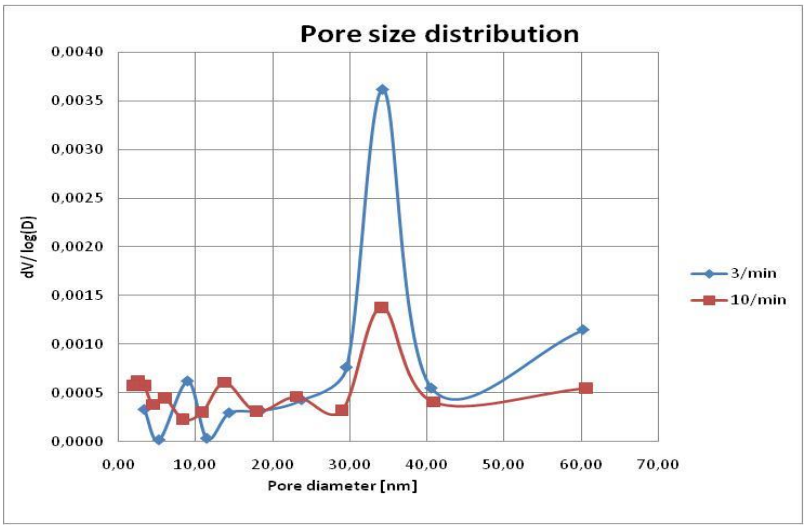

Figure 5. Pore size distribution.

Table 4. Values of the specific surface area of the materials and the pores, specific pore volume, average pore diameter, and percentage of pores smaller than 20 nm.

Heating rate, °C/min	Specific surface area of the material, m^2/g	Specific pore volume, cm^3/g	Specific surface area of pores, m^2/g	Average pore diameter, mm 10^3	Percentage of pores < 20 nm
3	1.2352	0.000694	0.1492	18.6035	20.5
10	0.9142	0.000784	0.4946	6.3439	61.6

pores < 20 nm. These results predict that the novel ceramic composites sintered with 10 °C /min will likely be more sensitive to the ice lens mechanism.

The results of the determination of frost action susceptibility to different frost action mechanisms are comparatively presented in Table 5.

Table 5 shows that the ceramic models sintered with 10 °C /min are more sensitive to the closed container mechanism and ice lens mechanism but less sensitive to the action of the hydraulic pressure mechanism.

Table 5. Summary of the dominant frost action mechanism.

Sample	Mechanism of the closed container, (ratio of pores r < 0,1 μm)	Mechanism of hydraulic pressure		Mechanism of ice lens, (percentage of pores < 20 nm)
		Rate of ice formation, Cd parameter	Permeability	
10	1	2	2	1
3	2	1	1	2

[1] Very sensitive to the specific mechanism; [2] less sensitive to the specific mechanism.

Low-temperature dilatation measurements

As the results of similar linear thermal expansion of both samples (in the temperature area 0°C to -40 °C), Figure 6 shows no major differences in the dilatation values between the dry and water-saturated samples. Therefore, based on these results, all models could be considered resistant to the action of the hydraulic pressure mechanism.

Pore structure (values of critical pore radius) and especially the scattering coefficient values showed that the models sintered with the heating rate of 10 °C /min are the most resistant to the hydraulic pressure mechanism. Furthermore, their compressive and flexural strength values, Table 2, correlate well with this estimation.

Biocorrosion resistance

The novel ceramic composites sintered with a heating rate of 10 °C /min had better stability to hydraulic pressure, which is known as the more common destruction mechanism in the case of ceramic materials [26]. Based on this fact, further investigations considering biocorrosion resistance were dedicated to this type of model sample. The obtained results were compared to the results of the products based only on

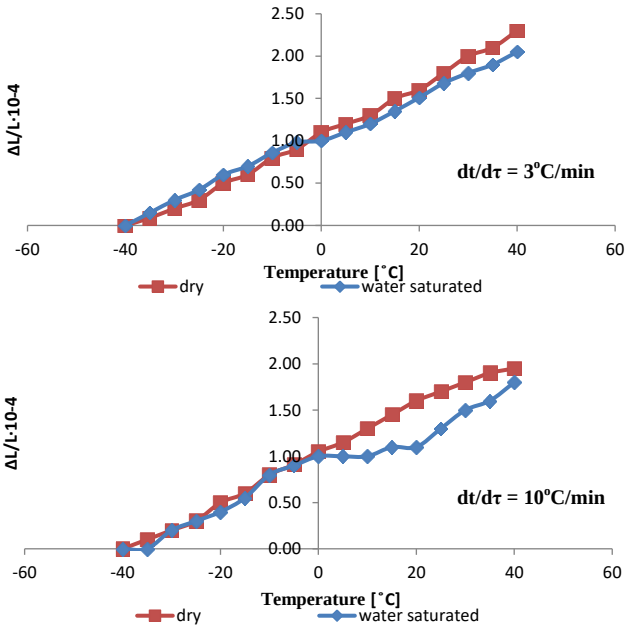

Figure 6. Low-temperature dilatation values of the composites.

the clay material/fly ash (heating rate 10 °C/min). The SEM micrographs in Figure 7 illustrate the results of the biocorrosion investigation.

The SEM micrographs show that the hyphae were present on the product's surface composed only from the clay material, Figure 7a. In contrast, the complete fungi formation was identified in the product fully designed based on fly ash, Figure 7 b. There is no sharply defined border between the outer surface and inner section, Figure 7 b, i.e., due to the high porosity of the compact, hyphae penetrate a part of the inside of the compact. In the case of the composite material, Figure 7 c and d, a very similar situation is observed as in the case of the product based only on the clay. The fungal growth on the sample surface is evident, but the beginning of the hyphae penetration into the ceramic composite structure was also noticed. It could be explained based on the fact that the colonization process of *A. niger* fungus goes through two stages [24]. In the primary stage, the colonization process is highly related to the capacity of microorganisms to attach themselves to the surfaces of the ceramic materials, while in the second phase, the textural properties are the key factors for their development [21]. Evidently, all three systems had the same surface affinity for the microorganisms, but the second stage of colonization differs as their textural properties differ. Based on the results shown in Table 2, it is evident that the changes in the values of the water absorption (indirectly, of the porosity value) from 0.34% (clay material) to 7.02% (novel composite material) and the changes from 23.77% (fly ash) to 7.02% (novel composite material), influenced the fungi growth and penetration differently. The penetration of the fungi is in good correlation with the decrease of the water absorption value. This value is more important for fungal growth and penetration than the raw material characteristics [21]. Moreover, in the case of novel products, chemical degradation and the presence of new mineralogical forms, due to the action of *A. niger*, were not observed. It is a positive result for further application of novel ceramic composites as building materials in real conditions.

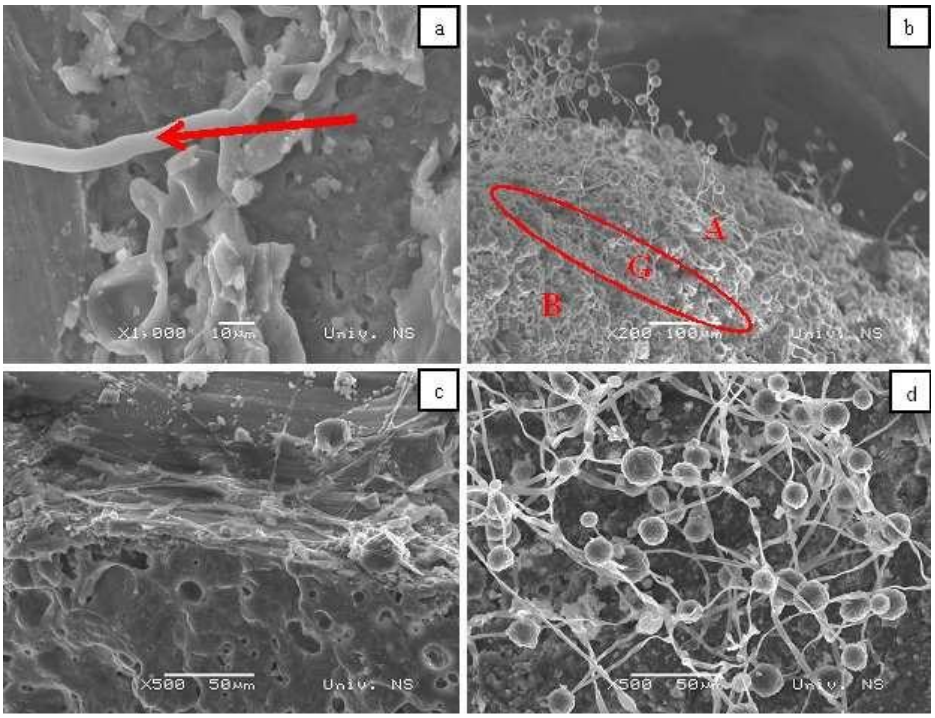

Figure 7. SEM micrographs of the final product prepared only with clay (a), fly ash (b), and the novel composite material (c and d).

CONCLUSION

The results of low-temperature dilatation confirmed satisfactory thermal stability of the formed ceramic composites (produced with different heating rates). Novel ceramic composites sintered with a heating rate of 10 °C/min, based on the results of textural properties, were more sensitive to the frost mechanisms of closed containers and ice lenses but less sensitive to the action of the mechanism of hydraulic pressure. Besides good durability regarding frost resistance properties, the simulation of biocorrosion deterioration (fungal action) initiated only aesthetic changes in the surfaces of the novel ceramic composites without chemical degradation. The results of durability investigations are encouraging, showing that the utilization of fly ash (40 wt.%) in ceramic composites is possible without the significant deteriorating effect of their resistance to frost action and microbiological corrosion action, compared with the ones produced only from clay material. Bearing in mind the high consumption of fly ash in the designed ceramic compacts (40 wt.%) and promising results regarding the resistance of the novel products in aggressive outdoor environments, the potential use of fly ash will reduce the environmental burden due to the accumulation of waste and will enable the production of more sustainable ceramic products.

ACKNOWLEDGMENTS

This research was supported by the Serbian Ministry of Education, Science and Technological Development, project No.: 451-03-9/2021-14/200134.

REFERENCES

[1] B. Angjusheva, E. Fidancevska, K. Lisichkov, V. Jovanov, J. Eng. Process. Manage. 8 (2016) 73–79. https://doi.org/10.7251/JEPMEN1608073A.

[2] S. Kramar, L. Zilbert, E. Fidancevska, V. Jovanov, B. Angjusheva, V. Ducman, Mater. Constr. 69 (333) (2019) e176. https://doi.org/10.3989/mc.2019.11617.

[3] D. Jubinville, E. Esmizadeh, S. Saikrishnan, C. Tzoganakis, T. Mekonnen, Sustainable Mater. Technol. 25 (2020) e00188. https://doi.org/10.1016/j.susmat.2020.e00188.

[4] B. Angjusheva, E. Fidancevska, V. Jovanov, Qual. Life 7(3–4) (2016) 59–65. https://doi.org/10.7251/QOL1603059A.

[5] B. Angjusheva, E. Fidancevska, V. Jovanov, Qual. Life 7(3–4) (2016) 53–58. https://doi.org/10.7251/QOL1603053A.

[6] M. Sutcu, E. Erdogmus, O. Gencel, A. A Gholapour, E. Atan, T. Ozbakkaloglu, J. Cleaner Prod. 233 (2019) 753–764. https://doi.org/10.1016/j.jclepro.2019.06.017.

[7] P. Lopez-Arcea, J. Garcia-Guinea, Build. Environ. 40 (2005) 929–941. https://doi.org/10.1016/j.buildenv.2004.08.027.

[8] P. Berdahl, H. Akbari, R. Levinson, W.A. Miller, Constr. Build. Mater. 22 (2008) 423–433. https://doi.org/10.1016/j.conbuildmat.2006.10.015.

[9] K. Ikeda, H.-S. Kim, K. Kaizu, A. Higashi, J. Eur. Ceram. Soc. 24 (2004) 3671–3677. https://doi.org/10.1016/j.jeurceramsoc.2003.12.014.

[10] M. Maage, ZI, Ziegelind. Int. 9 (1990) 472–481.

[11] M. Maage, ZI, Ziegelind. Int. 10 (1990) 582–588.

[12] L. Franke, H. Bentrup, ZI, Ziegelind. Int. 7-8 (1993) 483–492.

[13] R. Koroth, P. Fazio, D. Fedman, J. Archit. Eng. 9 (1998) 87–93. https://ascelibrary.org/doi/10.1061/%28ASCE%291076-0431%281998%294%3A1%2826%29.

[14] G.C. Robinson, Amer. Ceram. Soc. Bull. 56 (1995) 1071–1075.

[15] P. Vincenzini, Ceramurgia 3 (1974) 176–188.

[16] I.N. Grubeša, M. Vračević , J. Ranogajec, S. Vučetić, Materials 13 (2020) 2364. https://doi.org/10.3390/ma13102364.

[17] J.G. Ranogajec, S.L. Markov, O.Lj. Rudić, S.B. Vučetić, V.S. Ducman, Acta Period. Technol. 42 (1-288) (2011) 197–207. https://doi.org/10.2298/APT1142197R.

[18] M.L. Coutinho, J.P. Veig, M.F. Macedo, A.Z. Miller, Coatings 10 (2020) 1169. https://doi.org/10.3390/coatings10121169.

[19] W. Sand, Int. Biodeterior. 40 (1997) 183–190. https://doi.org/10.1016/S0964-8305(97)00048-6.

[20] J. Ranogajec, M. Radeka, in Self-Cleaning Materials and Surfaces, W.A. Daoud Ed., Wiley Online Library, (2013) 89–128. https://doi.org/10.1002/9781118652336.ch4.

[21] V. Jovanov, B. Anguseva, K. Pantovic, E. Fidancevska, "Ecological Truth" ECO-IST'15, XXIII International conference, Kopaonik, Serbia (2015) 207–211.

[22] V. Ducman, A.S. Skapin, M. Radeka, J. Ranogajec, Ceram. Int. 37 (2011) 85–91. https://doi.org/10.1016/j.ceramint.2010.08.012.

[23] M. Radeka, J. Ranogajec, J. Kiurski, S. Markov, R. Marinković-Nedučin, J. Eur. Ceram. Soc. 27 (2–3) (2007) 1763–1766. https://doi.org/10.1016/j.jeurceramsoc.2006.05.001.

[24] T. Chand Dakal, S.S. Cameotra, Environ. Sci. Eur. 24 (2012) 1–13. https://doi.org/10.1186/2190-4715-24-36.

[25] B. Angjusheva, E. Fidancevska,V. Jovanov, Chem. Ind. Chem. Eng. Q. 18 (2012) 245–254. https://doi.org/10.2298/CICEQ110607001A.

[26] H.S. Kim, J.M. Kim. K. Ikeda, Br. Ceram. Trans. 102 (2003)133-137. https://doi.org/10.1179/096797803225001623.

[27] M. Sveda, ZI, Ziegelind. Int. 55, (2002) 29–33.

[28] M. Sveda, ZI, Ziegelind. Int. 57 (2004) 36–43.

[29] T. Hulan, I. Stubna, J. Ondruska, A. Trnik, Minerals 10(10) (2020) 930. https://doi.org/10.3390/min10100930.

VOJO JOVANOV[1]
SNEŽANA VUČETIĆ[2]
SINIŠA MARKOV[2]
BILJANA ANGJUSHEVA[1]
EMILIJA FIDANCEVSKA[1]
JONJAUA RANOGAJEC[2]

[1]Univerzitet Sv. Ćirila i Metodija u Skoplju, Tehnološko-metalurški fakultet, Ruđer Bošković 16, 1000 Skoplje, Republika Severna Makedonija

[2]Univerzitet u Novom Sadu, Tehnološki fakultet, Bulevar cara Lazara 1, Novi Sad, Srbija

NAUČNI RAD

OTPORNOST NA DEJSTVO MRAZA I MIKROBIOLOŠKU KOROZIJU NOVIH KERAMIČKIH KOMPOZITA

U radu je prikazano predviđanje mehanizama delovanja mraza na keramičkim kompozitima, kao i analiza njihove otpornosti na biokoroziju dejstvom gljiva. Keramički kompoziti su proizvedeni od dve sirovine: lebdećeg pepela (40 mas. %) i glinenog materijala (60 mas. %). Ovi kompoziti pripremljeni su u laboratorijskim uslovima presovanjem (P = 45 MPa), sušenjem (105 °C, 3h) i sinterovanjem (1100 °C, 1h; brzine zagrevanja 3 °C/min i 10 °C/min). Mehanizmi propadanja projektovanih keramičkih kompozita definisani su na osnovu vrednosti ukupne poroznosti, raspodele veličine pora, kritičnog radijusa pora i faktora Maage, kao i vrednosti vodopropusnosti. Proces biokorozije je ispitan korišćenjem gljive Aspergillus niger kao modelnog mikroorganizma. Različiti stepeni kolonizacije upotrebnjenog mikroorganizma na dizajniranim kompozitima su uporedno analizirani na osnovu rezultata ispitivanja skenirajuće elektronske mikroskopije (SEM analiza). Rezultati dobijeni u ovom radu pokazuju da je upotreba lebdećeg pepela (40 mas. %) u keramičkim kompozitima moguća bez značajnog pogoršanja njihove trajnosti (dejstvo na mraz i mikrobiološka otpornost) u poređenju sa onima čija se proizvodnja zasniva samo na glini.

Ključne reči: tretman otpada, pepeo, keramika, starenje materijala, raspodela veličine pora, termička analiza.

CI&CEQ
Chemical Industry & Chemical Engineering Quarterly

Available online at
Association of the Chemical Engineers of Serbia AChE
www.ache.org.rs/CICEQ

Chem. Ind. Chem. Eng. Q. 29 (2) 111–118 (2023) CI&CEQ

MOHAMED SADEK[1]
REHAB M. EL-MAGHRABY[2]
MOHAMED FATHY[3]

[1]Egyptian Natural Gas Company GASCO, New Cairo, Cairo, Egypt

[2]Faculty of Petroleum and mining engineering, Suez University, Egypt

[3]Egyptian Refining Company (ERC), Mostorod, Cairo, Egypt

SCIENTIFIC PAPER

UDC 621.3:502/504

EVALUATION OF VARIABLE SPEED DRIVES TO IMPROVE ENERGY EFFICIENCY AND REDUCE GAS EMISSIONS: CASE STUDY

Article Highlights

- Installing variable frequency drivers improve energy efficiency
- Variable frequency drivers reduce energy consumption and greenhouse gas emissions by 67%
- Variable frequency drivers are economical, with a payback period of less than one year for fan equipment
- Variable frequency driver is not economically attractive for reciprocating compressors

Abstract

Variable speed drives are the most promising technique for reducing electric motors' energy consumption. This paper discusses energy savings by installing variable speed drives to control rotating equipment motors such as pumps, compressors, blowers, and fans in oil processing facilities. In addition to energy savings, variable speed drives will improve overall equipment efficiency, increase reliability, and reduce greenhouse gas (GHG) emissions. An energy audit was performed on a case study to investigate energy consumption for all electric motors. Technical and operational constraints for installing and operating variable speed drives were discussed. Installation requires adjustments in operation schedules and parameters to allow reducing energy consumption. The case study has illustrated how to calculate energy savings for pipelines, air coolers, air blowers for furnaces, pumps with variable flow rates, and reciprocating compressing systems. Variable speed drives were technically and economically accepted in air blowers, fans, and pumps. Energy consumption and GHG emission were reduced by 67%. The payback period for the whole project was less than one year. Meanwhile, it was not valid for reciprocating compressors as the payback period was 6.2 years.

Keywords: energy efficiency, pump optimization, greenhouse gas emissions, variable speed drives.

Oil refining is an intensive energy-consuming industry. Therefore, great interest has been put into minimizing energy consumption and reducing greenhouse gas (GHG) emissions. Most of the efforts on energy optimization focus on optimizing heat exchanging networks and furnaces operations as it represents most of the energy consumption. Electric energy represents a smaller percentage of the overall energy consumption at a refinery. However, it has an interesting potential for energy saving and reducing GHG emissions with a short payback period in many cases. Electric motors are the main driver for most rotating equipment like pumps, fans, blowers, and compressors at oil refineries. They consume about 80% of the electric energy consumption at an oil refinery (60% of the electric motors are driving pumps, 15% for air compressors, 9% for fans, and 16% for various applications) [1].

Fan laws or affinity laws define the relationship between fan or pump rotational speed (N), flow rate (Q), and brake horsepower required (P). Fan laws assume that the fan's efficiency remains constant at various rotational speeds [2].

Correspondence: M. Sadek, Egyptian Natural Gas Company GASCO, New Cairo, Cairo, Egypt.
E-mail: moh_sadek@gasco.com.eg
Paper received: 18 March, 2022
Paper revised: 29 Jun, 2022
Paper accepted: 28 July, 2022

https://doi.org/10.2298/CICEQ220318018S

$$\frac{Q_1}{Q_2} = \frac{N_1}{N_2} \quad (1)$$

$$\frac{H_1}{H_2} = \left(\frac{N_1}{N_2}\right)^2 \quad (2)$$

$$\frac{P_1}{P_2} = \left(\frac{N_1}{N_2}\right)^3 \quad (3)$$

where, Q is the flow rate, H is the head, P is the shaft power, and N is the pump's rotational speed. As the cubic relation between pump speed and horsepower requirement, a minor decrease in the speed will result in great energy savings. Fig 1 illustrates the change of the pump characteristic curve with changing speed. As the speed decreases, the Q-H curve moves toward a lower flow rate (Q) and head (H); there is a unique Q-H curve for every rotating speed. So, adjusting the rotating speed will give the exact required flow rate and significantly reduces energy consumption. Furthermore, as the speed decreases, the pump's best efficiency point (BEF) will also change [3]. So, adjusting the speed keeps the operating point as near as possible to the BEF point, resulting in energy savings. There are multiple ways to control the speed of the pump. Combustion engine or steam turbine drivers are equipped with speed control techniques that adjust speed as needed. Meanwhile, electric motor drivers have a constant speed and need gearboxes or belt drives to control speed. Fortunately, VSD could be integrated with electric motors to control their rotating speed.

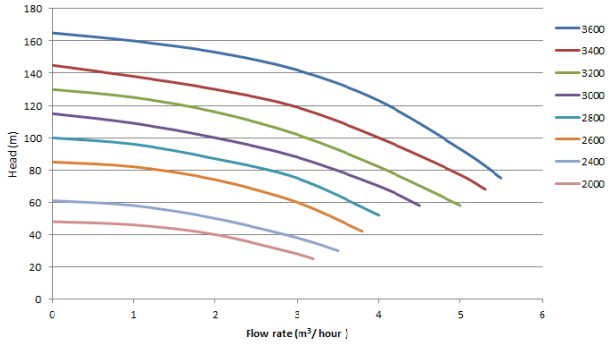

Figure 1. Pump performance curves at various speeds.

Variable speed drives (VSD) are electronic devices that change the motor rotation speed by changing the frequency of the electric current supplied to the motor. As the frequency of the supplied electric energy decreases, the rotational speed of the motor, energy consumption, and head decrease and vice versa [2]. That allows the motor speed to match the required flow rate. At lower demanded process flow rates reducing motor speed will reduce energy loss in friction and throttling by control valves or recycling. Modern VSD can adjust the rotation speed with an accuracy of ±0.1% independent of the motor load [4]. Such great speed control capability in VSD will achieve a greater flow rate control. Therefore, a small reduction in motor speed produces great savings. For example, reducing pump speed by 20% will reduce energy consumption by 50%. Fig 2. illustrates the expected savings when reducing motor speed.

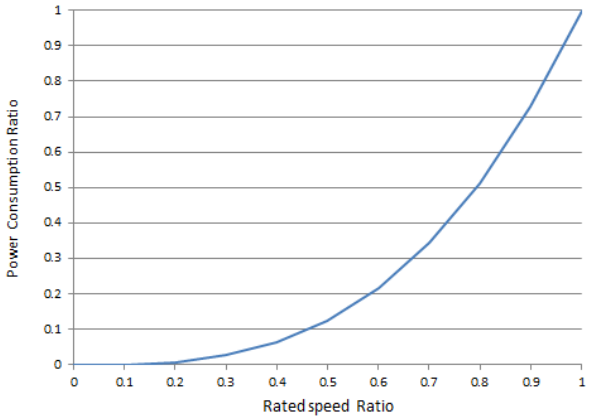

Figure 2. The relationship between motor power and rotation speed.

VSD consists of a Rectifier, regulator, and inverter. The supplied alternative current (AC) is converted to direct current DC in the rectifier, then the inverter converts the DC to AC adjusted at the required new frequency. The regulator controls the VSD components [4]. After great advancements in VSD technology, it became the most efficient controller and energy-saving technology for electric motors with variable load in operations. VSD installation reduces energy consumption, improves process control, provides soft starting for motors, and eliminates valve throttling to control the flow. Another advantage of using VSD is reducing GHG emissions [4].

VSD limitations

Despite the great benefits of VSD, there are multiple limitations to its widespread use. Harmonics, overheating, old motors compatibility, and limited space for installation are the major technical obstacles to installing VSD. Harmonics in electrical systems refers to the deviation of current and voltage waveforms from ideal sinusoidal waveforms. They are created via non-linear loads (like VSD) connected to power grids. Harmonics distort all equipment connected to the grid, causing overheating for cables, motors, and transformers [5]. There are multiple solutions to eliminate harmonics effects from VSD driving systems like Line reactors, passive or active filters, and Harmonic filters. Harmonic filters are the best technique to demolish harmonics effects; they are easy to apply, decrease system losses and increase the system's protection [4]. Most motors cooling systems depend on a fan connected to the motor shaft. As the speed decreases, the flow rate of cooling air decreases.

Overheating issues become clear at much-reduced motor speeds, so an external air-cooling source will help under such conditions [6]. Old motors may not have good compatibility with VSD drives, they have poor efficiency at low motor loads, and motor coil insulations may not withstand higher operating temperatures or electrical stresses. Finally, VSD drives need space for installation. A significant improvement has been achieved in reducing the size of units, including a built-in filter. In addition, manufacturers could provide customized space solutions that fit customers needed dimensions [7].

Effect of rotational speed change on efficiency

Affinity laws assume that the pump or fan efficiency stays constant at all rotation speeds. Therefore, the efficiency of the fan or pump decreases when reducing the speed lower than rated. For example, the efficiency drops when the rotation speed falls under 30% of the rated full speed. However, affinity laws could not predict decreased efficiency with rotation speed [8].

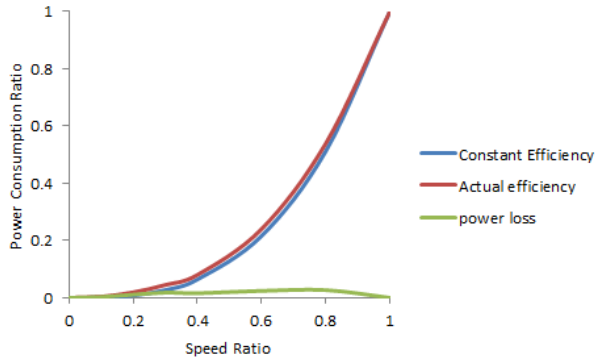

Figure 3. Case study shows the power loss due to a decrease in pump efficiency with speed reduction.

Fig 3. Illustrates results from a case study from Coelho and Andrade-Campos [9] or pump at various rotation speeds, at speed 30% of rated speed, the pump efficiency will be 60% of rated efficiency, and the energy loss due to efficiency decrease will be 1.8% of the rated power. The consumption will be only 13% of the rated power. The efficiency of the motor and VSD is also affected by reduced loads. As the speed decreases, the load and energy consumption decreases, so the efficiency of both motor and VSD will decrease. Fortunately, the motor has constant efficiency up to approximately 20% of rated power, and their decrease begins to be sharply lower than 20% of rated load as was indicated in Fig 1. [10]. On the other hand, VSD efficiency is still preserved at reduced loading, even at loads as low as 25% of the rated load [11]. As a result, VSD and motor efficiency will begin to have a clear effect at loads lower than 20% of the total load. However, the efficiency of the motor, pump, and VSD decreases sharply at extremely low loads, the energy saving achieved will outweigh the losses due to efficiency loss.

Economic considerations for VSD

Evaluating the economic factors for installing VSD is the most important step in VSD feasibility studies. As mentioned in [12], the companies are evaluating the financial benefits of projects based on indicators such as return on investment (ROI) and payback period (PBP). The payback period is the most important indicator calculated by Eq. (4). Payback period of fewer than two years is the most common for VSD replacement projects. However, an acceptable payback period depends on the availability of Funds and expected reliability improvements. Therefore, improving the equipment reliability favors the VSD installation even at a payback period longer than two years. In addition, VSD is the best energy-efficient solution for variable torque applications [13].

$$PBP = \frac{Total\ VSD\ Costs}{Total\ Energy\ Savings\ with\ VSD\ per\ year} \quad (4)$$

The total cost of VSD installation includes the cost of VSD Purchasing, cables, and installation Labor. The cost of VSD purchasing is most of the cost. Cable cost is variable according to required cable lengths and sizes. There are two types of VSD according to the operating voltage. First, low-voltage VSD is a good fit for lower-power equipment, and its cost is low. The second is medium voltage VSD, which deals with medium voltage VSD like 3300 V or 6600 V; it is very convenient with large power motors like 500 kW or above [14]. The prices for medium voltage VSD are higher than low voltage VSD. However, the prices for medium voltage VSD have decreased, comparing prices mentioned in [12] and [15]. The prices dropped by 45% from 2013 to 2019. Table 1 indicates the average cost per kW for VSD applicable for equipment in the oil and gas industry from local distributors in Egypt.

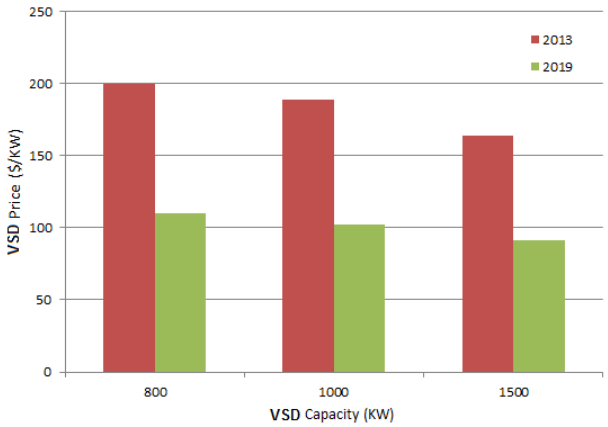

Figure 4. VSD prices 2013 vs. 2019.

Table 1. Average cost per kW for VSD in Egypt from the local market, prices in USD/kW.

Voltage Type	Low		Medium
Motor capacity, kW	0–10	10–100	500–1000
Average VSD Cost USD/kw	150	90	110

MATERIAL AND METHODS

Estimating Energy savings must be performed carefully. Errors usually overestimate energy savings and favor the installation of variable speed drives due to neglecting efficiency change with speed or neglecting the constraints of the system curve, including head and power requirements at reduced flow rates [16]. Energy savings by the VSD system depends on two factors: the ratio of reduction in rotational speed; the second is characteristic system curves.

The system characteristics curve illustrates the frictional and static head of the system against the flow rate. Systems with a dominated frictional head than a static head (the frictional head includes both head loss from throttling valves and pipeline friction) will have greater energy savings than systems with a dominated static head [6] since the speed reduction ratio must keep the head after reducing speed higher than the system curve to allow the flow.

There are several methods for estimating the expected energy savings by installing VSD on the pump and fan motors. A simplified method [4] to calculate the energy saving is based directly on applying affinity laws, assuming a constant efficiency for different fan speeds:

$$E_{motor} = T_o \times W_{rated} \times LF_{motor} \quad (5)$$

where. E_{motor} is the electric energy consumption without VSD (kWh), T_o is the number of operating hours, W_{rated} is the rated motor capacity (kW), and LF_{motor} is the loading factor for the motor:

$$SP_F = \left(\frac{N_1}{N_2}\right)^3 \quad (6)$$

where SP_F is the energy-saving factor, and N is the rotation speed:

$$E_{VSD} = \frac{T_{o,VSD} \times SP_F \times E_{motor}}{T_o} \quad (7)$$

where E_{VSD} is the electrical energy consumption (kWh) with VSD installed, and $T_{o,VSD}$ is the operating hours after installing VSD (h).

$$ES_{VSD} = E_{motor} - E_{VSD} \quad (8)$$

where ES_{VSD} is the energy savings in kWh.

The air compressing system could benefit from installing VSD by lowering the system's pressure and keeping start and stop cycles as low as possible. The energy-savings factor could be calculated using equation (9) to estimate the horsepower reduction factor (FR) based on current and proposed operating pressures [17].

$$FR = \frac{[(P_{dp} + P_i)/P_i]^{(K-1)/(K*N)} - 1}{[(P_{dc} + P_i)/P_i]^{(K-1)/(K*N)} - 1} \quad (9)$$

where P_{dp} is the reduced discharge pressure, P_{dc} is the discharge pressure at current operating conditions, P_i is the inlet pressure, k the ratio of specific heat for air (k = 1.4; dimensionless), and N is the number of stages; all pressures are in kPa.

Another advantage of reducing energy consumption is a similar reduction in the emission of GHG. The reduction in GHG due to applying VSD could be calculated similarly using equation (10) [18].

$$ER_{GHG} = ES_{VSD} \times \sum E_f \quad (10)$$

where ER_{GHG} is the GHG emission reduction per annum for CO_2, SO_2, and NO_x (kg), ES_{VSD} is the electrical energy saving (kWh), and E_f is the emission factor. Emission factors for natural gas electricity generation are 448.6 kg/MWh, 0.36 kg/MWh, and 0.36 kg/MWh for CO_2, NO_x, and SO_2, respectively [19].

Equations (5–10) assume that the energy loss due to motor and VSD efficiency decrease is negligible compared to the saving ratio of energy consumption.

Case study

A Qarun oil processing facility case study was selected to evaluate the savings by applying VSD to electric motors. This facility works at a variable feed flow rate. It receives crude oils from remote areas to perform preliminary oil processing. As a result, there are variations in inlet feed flow rates; multiple reasons, including variable production schedules, variable water content, and non-uniform tank settling and drainage durations, cause such variation.

The energy audit in Table 2. indicated the energy consumption profile for various rotating equipment at the facility. It includes the power load factor measured on-site and annual energy consumption in MWh for each piece of equipment at current operating conditions. Some equipment has duty and standby, and energy consumption was calculated based on the number of units in service. In addition, some equipment works on variable flow rates, and the flow rate variation is controlled through a control valve on pump discharge. Operating hours were indicated to calculate the total energy consumption per year in MWh.

Table 2. Energy audit at Qarun oil processing plant.

Equipment	Operating location	Rated power KW	Load Factor %	Installed units	Operating h/day	Running units	Total energy consumption MWh/year	Flow rate status
Pump shipping	Pipeline	450	0.86	3	12	2	3,401	Fixed
Pump-disposal	Pipeline	750	0.86	3	16	1	3,769	Fixed
Open drain	Pipeline	10	0.80	2	2	1	6	Fixed
DSD	Pipeline	21	0.85	2	12	1	78	Fixed
Heater pump A	VFP	56	1.00	2	24	1	490	Variable
Heater pump B	VFP	56	1.00	2	24	1	490	Variable
Heater pump C	VFP	56	1.00	2	24	1	490	Variable
Utility pumps	VFP	45	0.56	2	24	1	222	Variable
Potable pumps	VFP	15	0.94	2	24	1	124	Variable
Air blower	Fired Heater	3	0.49	11	24	11	142	Fixed
Air cooler fans	Air cooler	25	0.82	6	24	6	1,077	Fixed
Compressor	Compressor	100	0.44	2	24	1	385	Fixed
Total							10,674	

RESULTS AND DISCUSSION

The potential energy savings, GHG emission reduction, and cost savings by using VSD drives at Qarun oil processing facilities are evaluated in this section. Eqs (1–10) are used in the evaluation process at various flow rates. The financial indicators have been evaluated at current operating conditions and compared between operations with VSD installed against those without it. VSD losses were not included as it depends on the manufacturer and VSD loading factor. Also, VSD efficiency will be above 90% for loads up to 50% of its rated power [11]. Even the efficiency of the motor and fan or pump will decrease with decreasing the speed; Losses were estimated to be a very slight percentage compared to savings achieved.

Operation conditions like pump operating schedules, flow rates, and pressures were considered, so there is no negative impact for applying VSD into the plant. The cost calculations do not include the cost of labor as laborers are already available at Qarun Company with the required experience. When installing a VSD connection, energy feed lines bypasses could connect power directly to the motor. Therefore, the equipment could be in service without being affected in case of a VSD breakdown. In cost calculation, installing VSD has been considered for operating and standby equipment. The standby VSD represents a complete backup for the working VSD, which improves the overall reliability of equipment at the plant. The calculations and results were divided into groups; every group has similar operating conditions like pipeline pumps, variable flow rate pumps, fired heater blowers, air coolers fans, and air compressor motors. This will clarify in the results which equipment best fits VSD operation.

Energy savings were calculated for installing VSD on pumps installed on major plant pipelines, including (Pump shipping, Pump-disposal, Open Drain, and DSD). The results for all pipelines are illustrated in Table 3. The four pipelines have fewer than 24 h, so we can extend the operating hours to 24 h and simultaneously decrease the pump speed and flow rate. Operational constraints were considered while extending operating hours. For example, open Drain pumps have a restriction on flow rate, we could not extend the 2 h of operation to 24 h, and it will not be practical in operation. Installing VSD on all pipeline pumps saved 4,758 MWh/year and reduced energy consumption by 65%. GHG emissions were reduced by 2,137,861 kg/year. Three pipelines could reduce the flow rate and compensate for that by extending the operating hours to 24 h/day. Pipelines that restrict flow rates are less attractive opportunities for energy savings. All pipelines have a payback period of less than one year except for an open drain line, with a payback period of 4.5 years, which is extremely high compared with other pipelines.

Variable flow rate pumps, including heater pumps A, B, and C, utility pumps, and potable pumps, could not be replaced with smaller flow rate pumps, as the flow rate continuously changes and rises to the rated flow rate frequently for short durations during daily operation. So, we have two options for its optimization; first, we could install an additional smaller pump to work on a lower flow rate and keep the main pump for peak demand. However, installing an additional smaller pump is not feasible due to limited space for equipment. The second option is installing VSD on current pumps. As shown in Table 3, Installing VSD on pumps to regulate the flow will save 1433 MWh per year and

Table 3. Operation status before VSD installation VS after VSD installation.

Equipment	Operation without VSD				Operation with VSD				Energy Savings MWh/year
	Run hours per day	Rated flow rate BPD	Operating flow rate BBL/day	Energy consumption MWh/year	Run hours per day	Flow rate BBL/day	Reduced speed ratio	Energy consumption MWh/year	
Pump shipping	12	100,000	100,000	3,401	24	50,000	0.5	850	2,551
Pump-disposal	16	30,000	30,000	3,769	24	20,000	0.66	1,625	2,144
Open drain pump	12	13,000	13,000	78	24	6,500	0.5	19	59
DSD	2	10,000	10,000	6	4	6,500	0.5	1	4
Heater Pump A	24	25000	16500	491	24	16500	0.66	141	350
Heater Pump B	24	25000	17800	491	24	17800	0.71	177	314
Heater Pump C	24	25000	12500	491	24	12500	0.5	62	429
Utility pumps	24	7500	2000	222	24	2000	0.27	4	218
Potable pumps	24	4350	1000	124	24	1000	0.23	2	122
Air blower	24	1200	720	142	24	720	0.6	30	110
Air cooler fans	24	$3.56*10^8$	$3.56*10^8$	1077	24	$2.136*10^8$	0.6	232	845
Compressor	24	8400	8400	385	24	7560	0.9	328	58
Total				10677				3471	7204

reduce energy consumption by 78% while keeping operation regular without being affected. In addition, all pumps with variable flow rates have an average payback period of 0.58 years which is very encouraging to pursue in the project.

A fired heater damper or throttling on air blower discharge does not supply the exact flow for the optimized combustion. VSD is more sensitive and accurate in adjusting the flow rate required for the complete combustion process. Energy savings were achieved from two sides. First, energy consumption for blowers at reduced flow rates would decrease without throttling. Second, it would adjust the required air to guarantee complete optimized combustion. VSD of air blowers could be connected to flow gas sensors to measure the concentration of flue gases as an indicator of combustion efficiency to increase or decrease the amount of air supplied. Heater efficiency improvements were not included in calculations as it is difficult to predict efficiency accurately without a flow gas analyzer. Installation of VSD for the heater will save 110 MWh /year; it has a payback period of 0.9 years without including efficiency improvements of the heater. Results have indicated that VSD will be feasible for blowers of fired heaters with a payback period of fewer than 11 months.

Energy savings were calculated for installing VSD on all air cooler fans to match fan speed with ambient temperature. The airflow rate was designed for 42 °C, but the ambient air temperature is 24 °C. Therefore, we had an opportunity to decrease the amount of cooling to 40% of the current rate on average operation around the year. It would reduce energy consumption by 78%. Installation of VSD for the air cooler fans would save 845 MWh/year, and the payback period was 0.32 year. Results have indicated that VSD will be feasible for fans of air coolers with a payback period of 4 months.

The air compressor at Qarun is a reciprocating compressor. The compressor discharge is connected to the receiver air storage vessel. It works on start and stops cycles. When the receiver tank pressure decreases, the compressor starts and keeps running until the pressure achieves the set high pressure in the receiver tank. Receiver tanks play a significant role in compressor operation, minimizing the compressor's start and stopping as an air reservoir. In addition, it is redundant for peak demands from the air that exceeds compressor output. Energy savings in a reciprocating compressor is not achieved directly as reducing rotation speed does not have any energy reduction in compression energy. Fortunately, from Eq. (9), reducing receiver tank pressure will reduce energy consumption. But reducing receiver tank air pressure will increase the start and stop cycles for the compressor. Here is the function of VSD, we could decrease the compressor rotation speed to minimize start and stop cycles at reduced receiver tank pressure. For the current operating conditions of the compressor and air distribution system, the pressure of the air receiver tank could be reduced from 120 psi to 90 psi without interrupting operation. VSD will regulate the compressor's rotation speed to keep the start and stop

cycles within acceptable limits. Energy consumption was reduced by 15% and saved 58 MWh/year. The payback period is 6.2 years, which is not attractive, especially when funds are limited.

Table 4. Economic evaluation for energy savings with VSD.

Equipment	No. of VSD Units installed	VSD price in USD/KW	VSD Cost (USD)	Energy savings MWh/year	Payback period (year)	Emissions reduction kg/year
Pump shipping	3	110	148500	2551	1.17	1,146,214
Pump-disposal	1	110	82500	2144	0.77	963,342
Open drain pumps	1	90	900	4	4.5	1,796
DSD	2	90	3780	59	1.29	26,509
Heater A	2	90	10080	350	0.58	157,262
Heater B	2	90	10080	314	0.64	141,086
Heater C	2	90	10080	429	0.47	192,757
Utility	2	90	8100	218	0.75	97,951
Potable	2	90	2700	122	0.44	54,817
Air blower	11	150	4950	110	0.9	49,426
Air cooler	6	90	13500	845	0.32	379,675
Compressor	2	90	18000	58	6.2	26,061
Total			313170	7204	0.9	3,236,896

*Payback period was calculated on industrial electric prices of 50 USD / MWh. * Emissions reductions include carbon dioxide and sulfur and nitrogen oxides.

CONCLUSION

Oil processing and refining plants have great potential for energy saving by widely applying VSD to electric motors. An energy audit was done on the Qarun oil processing plant, and energy-saving calculations were performed on applying VSD. Applying VSD to all equipment will save 7,204 MWh/year, 360,150 US$/year, and reduce GHG total emissions by 3,236,896 kg/year or 67% of current emissions. The average payback period is about 0.87 years. The calculation procedures used could be applied to any refinery unit or oil processing facility, considering the process limitations of operating variables like operation schedules, pressures, and flow rates.

ACKNOWLEDGMENTS

The author would like to thank all Qarun Petroleum Company personnel who provided data and technical support for the case study.

REFERENCES

[1] E. Worrell, M. Corsten, C. Galitsky, Energy Efficiency Improvement and Cost Saving Opportunities for Petroleum Refineries, US Environmental Protection Agency, Washington, (2015) p. 66. https://www.energystar.gov/sites/default/files/tools/ENERGY_STAR_Guide_Petroleum_Refineries_20150330.pdf.

[2] V.K. Arun Shankar, S. Umashankar, S. Paramasivam, H. Norbert, Appl. Energy 181 (2016) 495–513. https://doi.org/10.1016/j.apenergy.2016.08.070.

[3] E. da Costa Bortoni, R.A. de Almeida, A.N.C Viana, Energy Effic. 1 (2008) 167–173. https://doi.org/10.1007/s12053-008-9010-1.

[4] R. Saidur, S. Mekhilef, M.B. Ali, A. Safari, H.A. Mohammed, Renewable Sustainable Energy Rev. 16 (2012) 543–550. https://doi.org/10.1016/j.rser.2011.08.020.

[5] J. Saxena, B.K. Choudhury, K.M. Agrawal, Encycl. Renewable Sustainable Mater. 3 (2020) 534–544. https://doi.org/10.1016/b978-0-12-803581-8.11010-0.

[6] A.T. De Almeida, F.J.T.E. Ferreira, D. Both, IEEE Trans. Ind. Appl. 41 (2004) 136–144. https://doi.org/10.1109/icps.2004.1314992.

[7] A.S. Tamez, MSc. Thesis, Utrecht University, (2019) P. 21. https://studenttheses.uu.nl/handle/20.500.12932/33582.

[8] T. Walski, K. Zimmerman, M. Dudinyak, P. Dileepkumar, Proced. World Water Environ. Resour. Congr. 2003 (2003) pp. 1–10. https://ascelibrary.org/doi/abs/10.1061/40685(2003)137.

[9] B. Coelho, A.G. Andrade-Campos, J. Hydraul. Re. 54 (2015) 586–593, https://doi.org/10.1080/00221686.2016.1175521.

[10] R. Saidur, Renewable Sustainable Energy Rev. 14 (2010) 877–898. https://doi.org/10.1016/j.rser.2009.10.018.

[11] US DOE, Adjustable Speed Drive Part-Load Efficiency, Washington, DC (2012) p. 1. https://www.energy.gov/sites/prod/files/2014/04/f15/motor_tip_sheet11.pdf.

[12] A.J.H. Nel, D.C. Arndt, J.C. Vosloo, M.J. Mathews, J. Clean. Prod. 232 (2019) 379–390. https://doi.org/10.1016/j.jclepro.2019.05.376.

[13] IPEICA, Electric Motors, https://www.ipieca.org/resources/energy-efficiency-solutions/efficient-use-of-power/electric-motors/ (accessed Jan. 09, 2021).

[14] SIEMENS, Cost Considerations When Selecting Variable Frequency Drive Solution, SIEMENS, (2018) 1–10. https://assets.new.siemens.com/siemens/assets/api/uuid:064ed3aa-0d92-4c5b-9f7a-1aeb094518a8/cost-considerations-whitepaper1.pdf

[15] G.E. Du Plessis, L. Liebenberg, E.H. Mathews, Appl. Energy 111 (2013) 16–27. https://doi.org/10.1016/j.apenergy.2013.04.061.

[16] R. Carlson, IEEE Trans. Ind. Appl. 36 (2000) 1725–1733. https://doi.org/10.1109/28.887227.

[17] D. Kaya, P. Phelan, D. Chau, H.I. Sarac, Int. J. Energy Res. 26 (2002) 837–849. https://doi.org/10.1002/er.823.

[18] EA Abdelaziz, R. Saidur, S. Mekhilef, Renewable Sustainable Energy Rev. 15 (2011) 150–168. https://doi.org/10.1016/j.rser.2010.09.003.

[19] EIA, EIA-State Electricity Profiles, https://www.eia.gov/electricity/state/unitedstates/ (accessed Jan. 10, 2021).

MOHAMED SADEK[1]
REHAB M. EL-MAGHRABY[2]
MOHAMED FATHY[3]

[1]Egyptian Natural Gas Company GASCO, New Cairo, Cairo, Egypt

[2]Faculty of Petroleum and mining engineering, Suez University, Egypt

[3]Egyptian Refining Company (ERC), Mostorod, Cairo, Egypt

NAUČNI RAD

EVALUACIJA POGONA SA PROMENLJIVOM BRZINOM ZA POBOLJŠANJE ENERGETSKE EFIKASNOSTI I SMANJENJE EMISIJA GASOVA: STUDIJA SLUČAJA

Pogoni sa promenljivom brzinom su najperspektivnija tehnika za smanjenje potrošnje energije elektromotora. U ovom radu se govori o uštedi energije ugradnjom pogona sa promenljivom brzinom za upravljanje rotirajućim motorima opreme, kao što su pumpe, kompresori, duvaljke i ventilatori u postrojenjima za preradu nafte. Pored uštede energije, pogoni sa promenljivom brzinom će poboljšati ukupnu efikasnost opreme, povećati pouzdanost i smanjiti emisije gasova sa efektom staklene bašte. Energetski pregled je urađen na studiji slučaja da bi se ispitala potrošnja energije za sve elektromotore. Razmotrena su tehnička i operativna ograničenja za ugradnju i rad pogona sa promenljivom brzinom. Instalacija zahteva prilagođavanje rasporeda i parametara rada kako bi se smanjila potrošnja energije. Studija slučaja je ilustrovala kako izračunati uštedu energije za cevovode, hladnjake za vazduh, ventilatore za peći, pumpe sa promenljivim protokom i klipne sisteme za kompresiju. Pogoni sa promenljivom brzinom su tehnički i ekonomski prihvaćeni u vazdušnim duvaljkama, ventilatorima i pumpama. Potrošnja energije i emisija gasova sa efektom staklene bašte smanjeni su za 67%. Period otplate za ceo projekat je kraći od godinu dana, osim za klipne kompresore čiji period otplate je 6,2 godine.

Ključne reči: energetska efikasnost, optimizacija pumpi, emisije gasova staklene bašte, pogoni sa promenljivom brzinom.

CI&CEQ
Chemical Industry & Chemical Engineering Quarterly

Available online at
Association of the Chemical Engineers of Serbia AChE
www.ache.org.rs/CICEQ

Chem. Ind. Chem. Eng. Q. 29 (2) 119–128 (2023) CI&CEQ

WALAA MAHMOUD SHEHATA[1]
MOHAMED GALAL HELAL[2]
FATMA KHALIFA GAD[1]

[1]Department of Petroleum Refining and Petrochemical Engineering, Faculty of Petroleum and Mining Engineering, Suez University, Suez, Egypt

[2]Khalda Petroleum Company, Salam Gas Plant, Western Desert, Egypt

SCIENTIFIC PAPER

UDC 665.61:628.3:66

ENERGY SAVING IN OILFIELDS BY USING WASTE HEAT IN THE DISPOSED WATER

Article Highlights

- Heating brackish water used in desalter increased the desalting rate
- Heating the crude oil before shipping reduces the power of the shipping pump
- The optimum heating temperature for brackish water and crude oil was determined
- An economic study was applied to calculate the capital cost of the new heat exchangers used for heating

Abstract

The present work aims to retrofit an existing Egyptian oilfield plant to improve desalter performance and reduce the power of crude oil shipping pumps. In this work, waste heat in disposed water that represents a value is used in heating brackish water injected over desalter and in heating crude oil before shipping. ASPEN HYSYS version 11 simulation software was used. The retrofit of the considered oilfield plant is based on the implementation of two new heat exchangers to recover waste heat in the disposed water. The results showed that using waste heat to heat the brackish water in the desalter from 30 °C to 71.11 °C will increase the operating temperature of the desalter and thus increase the sedimentation and separation rate. On the other hand, using waste heat in heating the crude oil before shipping from 37.78 °C to 71.11 °C reduces the oil viscosity from 1.536 cSt to 0.9735 cSt. Reducing the viscosity of the crude oil will reduce the pressure drop of the shipping pumps, and therefore the power required to pump the oil will be reduced. The presented retrofit design can be used as a guide in upgrading existing plants and plants under the design phase.

Keywords: desalter, viscosity reduction, shipping pumps, crude oil, simulation.

Heavy crude oil production is considered uneconomic due to the intensive recovery cost from transportation, refining, and low market value. However, improved crude oil transportation using pipelines can be achieved by reducing the viscosity of the crude oil to enhance the followability of oil via pipelines. Several techniques have been demonstrated to improve the crude oil flow properties through pipelines by reducing crude viscosity [1–5]. These techniques are as follows: blending and dilution with light hydrocarbons; using core annular flow; drag reduction additives; lowering the oil pour point by using depressants (PPD); using solvent or emulsification through the formation of oil in water emulsion; heating the crude oil and the pipeline.

The blending and the dilution technique is based on decreasing the viscosity of heavy crude oil by mixing the oil with another oil having a lower viscosity. The diluent may be light crude oil [6–8], naphtha [9,10], alcohol [7,9], condensate [10,11], or kerosene [6].

The core annular flow technique is based on oil-water two-phase. First, the pipeline wall is lubricated with water. Then, the crude oil in the pipeline is surrounded by water. The water absorbs the shear stress between the pipeline wall and the oil. The water has a viscosity lower than oil, so it goes to the pipeline

Correspondence: W.M. Shehata, Department of Petroleum Refining and Petrochemical Engineering, Faculty of Petroleum and Mining Engineering, Suez University, Suez, Egypt.
E-mail: walaashahata78@yahoo.com
Paper received: 1 December, 2021
Paper revised: 30 May, 2022
Paper accepted: 7 August, 2022

https://doi.org/10.2298/CICEQ211201019S

wall, which has high shear stress. The crude oil is the core, while the water is the annulus. This technique decreases the pressure drop through the pipeline [5,12,13].

Drag reduction additives are used to reduce the high frictional loss produced due to the high viscosity of the heavy crude oil for turbulent flow. The high frictional loss leads to much energy being applied to transport the heavy crude oil to compensate for the wasted energy consumed by this frictional loss [5]. The additives used for drag reduction may be surfactants [5,14], fibers, and polymers [15,16].

Heavy crude oil is composed of asphaltenes macromolecules and liquid material. These macromolecules are deposited in crude oil and contribute to its high resistance to flow in pipelines. The pour point depressants (PPD) can decrease the deposition of asphaltenes and improve oil flow properties. The pour temperature of the oil is the lowest temperature at which the oil cannot flow. Copolymers such as polymethacrylate, methacrylate, etc., are the most pour point depressants used. These copolymers can inhibit the precipitation of the asphaltenes and increase the flowability of the crude oil through the pipeline [4,17]. Waxy crude oil behaves as asphaltenes crude oil, and the PPD is used in waxy crude oil to decrease the wax deposition.

Emulsification through oil formation in water emulsion technique is the latest technology used to reduce the viscosity of heavy crude oil in pipeline transportation. First, heavy crude oil is emulsified in water and stabilized with the help of surfactants. Then, the oil is dispersed in water as droplets with the help of surfactants, and a stable oil-in-water emulsion with low viscosity is produced [1,2,4,18]. The surfactant is used to prevent the separation of the oil and water phase into two phases in the pipeline.

Heating the crude oil and the pipeline technique is the most popular for transporting heavy crude oil through pipelines [5]. This technique decreases the viscosity of heavy crude oil by increasing its temperature. Heating decreases the resistance of heavy crude oil to flow. Heating the crude oil and heating the pipeline is required due to the energy loss to the surrounding along the pipeline during transportation. Heating the pipeline is done by implementing heating stations along the pipeline [1,18].

As Santos *et al.* [6] presented, heat losses can be reduced by insulating the pipeline. Insulating the pipeline for short distances to reduce heat losses is effective in contrast with long distances. Ghannam and Esmail [19] reported that by heating medium crude oil to 30 °C, the viscosity of the crude oil decreased from 700 cP to 300 cP. However, the heating technique has high capital and operating costs, as presented by Sanier *et al.* [4] and Chang *et al.* [20], since this technique requires many heating and pumping stations along the pipeline. Heating the heavy crude oil at pumping stations is done using fired heaters, as mentioned by Martinez-Palou *et al.* [3].

A large variety of opportunities exist in the petroleum industry to reduce energy consumption while maintaining plant productivity. Studies conducted by several companies have shown the potential for energy savings in utilities. The energy efficiency improvement in the utility area has reached 30%, the heater burning area is 20%, the process improvement area is 15%, the heat exchanger area is 15%, the engine utilization area is 10%, and other areas are 10% [21]. In addition, several innovation trends are taking shape in the oil and gas industry to address sustainable energy opportunities [22–24].

No existing plants always achieve the processing goals that would be more economically beneficial. Other plants do not achieve the performance they were originally designed, which may be due to changes in feed conditions (flow, temperature, pressure, configurations), aging equipment and wear and tear, or fluctuation in production and pipeline demand. It is possible to work on retrofitting old technologies to be a profit and operational flexibility tool. The retrofit design must be based on actual operating conditions in the field. Retrofit is more complex than designing a new plant. Retrofit is centered around existing equipment as much as possible to reduce the overall cost of the retrofit design. For choosing an appropriate retrofit, it is better to try to achieve the end user's desired retrofit performance goals with a low impact on the existing plant.

In this work, an existing oilfield plant will be retrofitted to increase the performance of the desalter by increasing its operating temperature, which will increase the salt deposition rate inside the desalter unit. Also, with this retrofit, the energy consumption used in the shipping pumps will be reduced by reducing the viscosity of the oil pumped into the pipeline and the pressure drop of the shipping pumps.

Case study

The proposed retrofits have been applied to an existing oilfield plant in the western desert of Egypt. The crude oil produced from oilfields contains salts in addition to other impurities as a result of the presence of the formation water. Due to the corrosive effects of the salts on metals damage pipelines and upstream and downstream facilities, it is therefore essential to reduce the salts and water content of the crude oil

before being delivered through the crude pipeline for exporting. As described in Figure 1, the feed from different wells flows through oil flow lines to Free Water Knock-Out Drum (FWKOD) system installed upstream inlet separators to improve the facility's performance and provide bulk gas and water separation. Gases in the free water knockout drum are directed to gas compression for compression and shipping in the gas pipeline. The oil flow is separated into six processing trains, A, B, C, D, E, and F, to separate the emulsion water in the oil to achieve the product specifications. The following equipment is used for each train; indirect heater, separator, heater treater, and oil feed pump. The indirect heater is a water bath heater used to heat process fluid received from the manifold to improve downstream three-phase separation efficiency to separate the emulsion water in the three-phase separator. Flashed gases from the separator will be directed to the fuel gas system, and excess gases will be flared at the flare stack. Separated water will be directed to water disposal into disposal wells. The oil from the three-phase separator is directed to the heater treater to further separate the emulsion water in the oil.

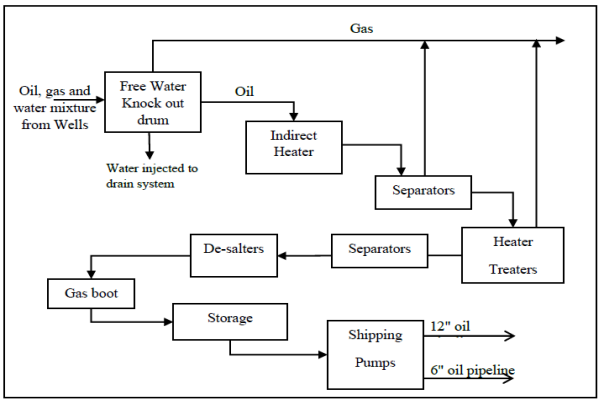

Figure 1. Case study block flow diagram.

The heater treater is used to remove the water from the oil from the production separator package unit to improve its quality and send it to the desalter package unit. The heater treater typically combines the following components inside a heater, free water knockout and oil/gas separator. The heater treater unit extracts the maximum possible water from the water/oil mixture by heating. It is designed to heat the oil and water mixture to 65 °C and to dehydrate the produced crude oil to a level of water content in oil of 3%vol. Outlet oil is pumped by an oil feed pump to desalter packages for oil desalting. Oil feed pumps are centrifugal pumps used to deliver the treated oil from the heater treater to the desalter package at a pressure that guarantees no vapor formation in the desalter to protect the transformer from ruining.

The Desalting process consists of two desalter packages. A brackish water skid feeds the two packages. Brackish water is used to wash the solid salts from the crude oil inside the desalter. Desalted oil will be flashed slightly above atmospheric pressure at the gas boot to separate dissolved gas in the desalted oil before exiting from desalters. The gas boot allows the product crude oil stream to degas to the maximum extent before flowing to the metering tanks and then exported through the pipeline to the required destination. The fluids from the desalters enter the standpipe gas boot, where gases are separated and directed to the existing flare system. Liquids are discharged through a bottom nozzle and a liquid seal to guarantee no vapor formation in the metering tanks.

Storage tanks are used to receive the daily crude oil production to provide a convenient storage volume for the product crude oil to be exported. We have six existing storage tanks that will be operated; one tank will be filled while another will be used in shipping (each cycle takes approximately 12 h). Meanwhile, the other tanks will be used for settling.

The shipping pump is sized for a differential pressure of 1034 kPa. There are two shipping pipelines with a diameter of 6" and 12", respectively, and the total shipping pipeline length is 110 km. The two pipelines are equipped with a pig launcher and receiver to enable pipeline pigging. In addition, drag-reducing agents are injected over the pipelines to increase their capacity to handle the load.

The crude oil in this case study has a high pour point of 18.33 °C which needs to be stored at a higher temperature of 60 °C to overcome the freezing problem and pipeline stoppage. But storage at a higher temperature releases gas above storage tanks, which is unsafe in the plant as storage tanks contain pig stock. Adding naphthenic base condensate will improve the pour point and save the heating cost and drag reducer injected into the oil shipping pipeline. Still, condensate is not available in this plant.

In this work, a simple retrofit of the case study was made. The crude oil that left storage tanks was heated before shipment using waste heat in the water, leaving the free water knockout drum. It will improve the oil's viscosity and keep the pipeline operating temperature above the pour point with an appropriate safety factor. In addition, this will save energy consumed by the shipping pumps and can reduce the required drag dose reducer injection.

Retrofit methodology

The proposed retrofits in the presented case study are based on implementing two new heat exchangers to utilize the waste heat in the water separated from the

free water knockout drum going to disposal wells at 48.89 °C. The first heat exchanger is used to heat the brackish water injected over desalter packages. It will increase the performance of desalters by increasing the efficiency of the separation of dissolved salts and reducing the time required to achieve product specifications. Heat exchange is applied between the brackish water used in the desalter and the water leaving the free water knockout drum. The second new heat exchanger is used to heat the crude oil before shipment in the pipeline. It will reduce the viscosity of the crude oil being pumped and thus reduce the energy consumption of the shipping pumps. Heat exchange is applied between the pumped crude oil and the water separated from the crude oil from the free water knockout drum. Figure 2 shows the proposed retrofits.

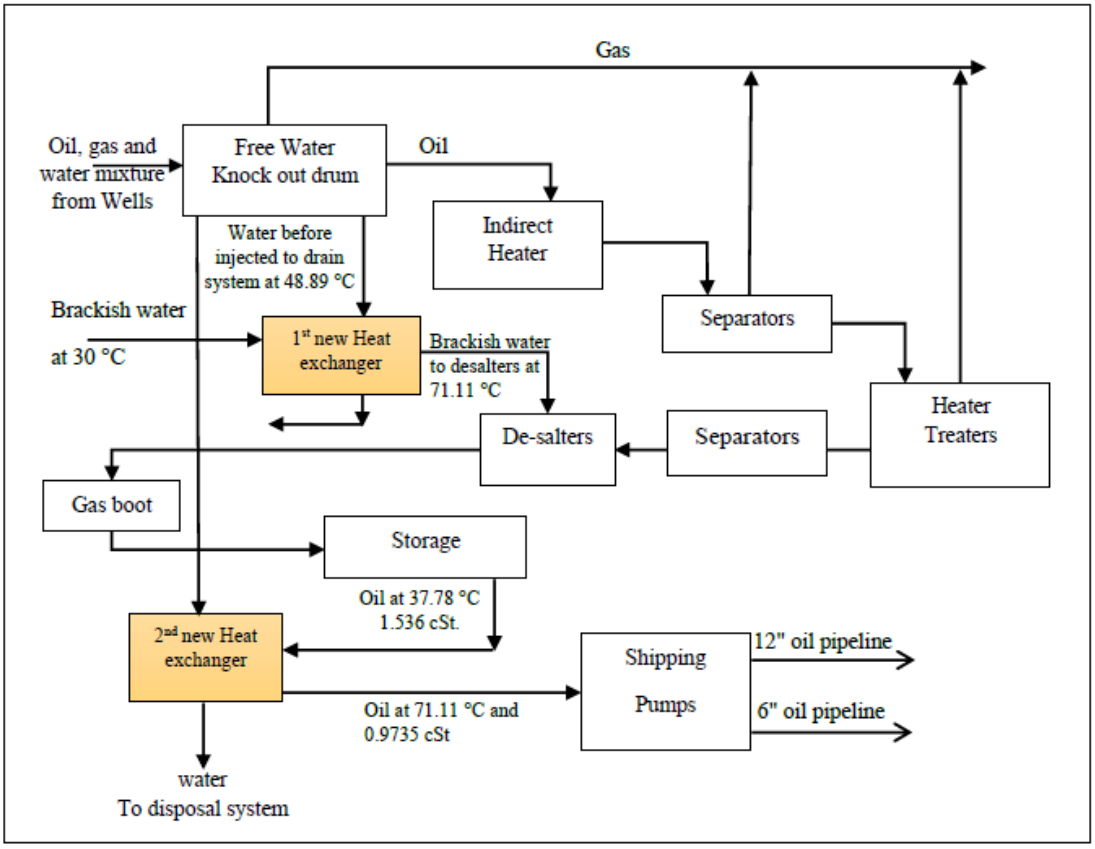

Figure 2. Case study block flow diagram with the proposed modification.

Decreasing the power of the shipping pump

In this work, decreasing the power consumption of the shipping pumps is based on decreasing the discharge pressure or the pressure drop of the shipping pump due to decreasing the kinematic viscosity of the pumped crude oil. There is a relationship between the power consumption of the pump and the kinematic viscosity according to the following equations [25–28]:

$$Power = 18.18\frac{\Delta P}{\eta} \quad (1)$$

where ΔP is the pressure drop of the pump and η is the efficiency of the pump, which is assumed to be 80%.

It is noted from Eq. (1) that the main factor affecting the power consumption is the pump's pressure drop, which is calculated according to Eq. (2).

$$\Delta P = 4\tau\frac{1}{d} \quad (2)$$

where τ is the shear stress in the pump (dyne/cm^2), and d is the pipeline's diameter (cm). The shear stress and the shear rate (γ, 1/s) are calculated from equations (3) and (4), respectively.

$$\tau = -\mu\gamma \quad (3)$$

$$\gamma = \frac{8V}{d} \quad (4)$$

where μ is the dynamic viscosity (cP), and V is the crude oil velocity (cm/s). The dynamic viscosity is obtained from the kinematic viscosity as illustrated in Eq. (5):

$$\mu = \nu\rho \quad (5)$$

where ν is the kinematic viscosity (cSt) and ρ is the

crude oil density (g/cm^3).

From the previous equations, there is a direct relation between the pressure drop of the pump and the kinematic viscosity of the pumped crude oil, as presented in Eq. (6), when all the other variables (V, ρ, d) are unchanged.

$$\Delta P = 32\left(\frac{V}{d^2}\right)\rho\nu \tag{6}$$

By decreasing the kinematic viscosity of the pumped crude oil, the pressure drop of the pump will decrease. Therefore, the pump's power consumption will decrease, too, according to Eq. (7):

$$Power = (18.18\times 32)\left(\frac{V}{d^2}\right)\frac{1}{\eta}\rho\nu \tag{7}$$

RESULTS AND DISCUSSION

The commercially available software ASPEN HYSYS version 11 was used to model the oil plant. Peng-Robinson equation of state has been used as it is suitable in this case. The present work aims to modify an existing oil plant to benefit from waste heat in the disposal water and study the effect of this modification on the desalter performance and power consumption of the shipping pumps. The feed stream operating conditions and composition are illustrated in Table 1. Figure 3 shows the simulated process flow diagram of the plant under study. Table 2 illustrates the simulated process's conditions of all streams.

Table 1. Feed stream compositions and specifications.

FEED composition	Mole fraction	FEED composition	Mole fraction
H_2O	0.9233	n-Pentane	0.0011
H_2S	0.0000	n-Hexane	0.0027
CO_2	0.0019	Methyl cyclopentane	0.0003
Nitrogen	0.0001	Benzene	0.0000
Methane	0.0244	Cyclohexane	0.0007
Ethane	0.0077	n-Heptane	0.00000
Propane	0.0030	n-Octane	0.00000
i-Butane	0.0006	n-Nonane	0.00000
n-Butane	0.0013	n-Decan	0.00000
i-Pentane	0.0009	C7+	0.03200
FEED conditions			
Temperature, °C		48.89	
Pressure, kPa		721.9	
Mass flow, kg/h		1008881.9035	

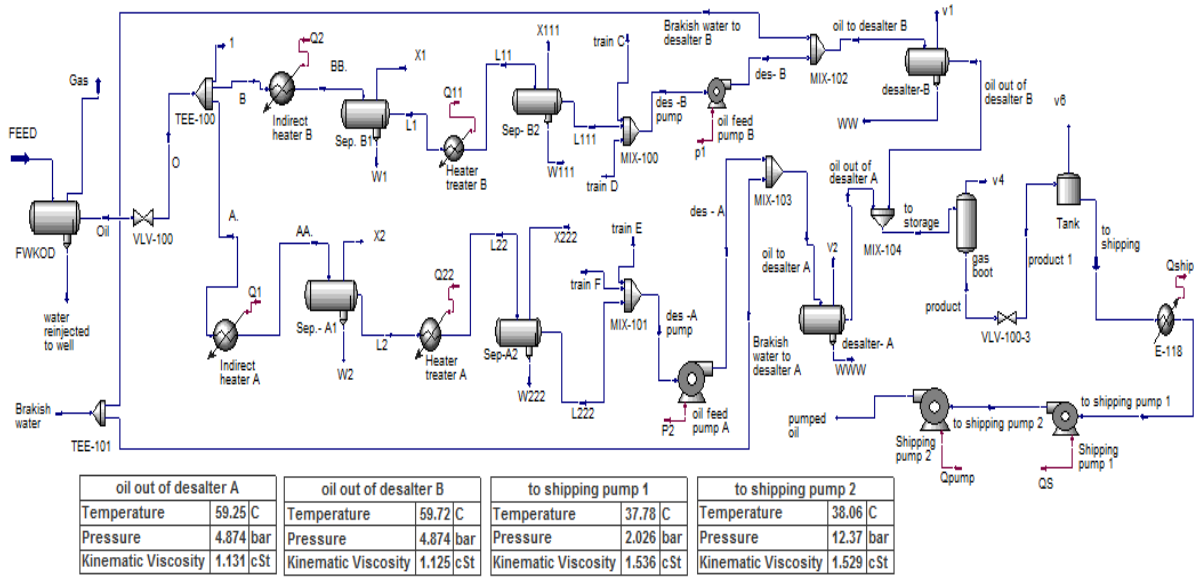

oil out of desalter A		
Temperature	59.25	C
Pressure	4.874	bar
Kinematic Viscosity	1.131	cSt

oil out of desalter B		
Temperature	59.72	C
Pressure	4.874	bar
Kinematic Viscosity	1.125	cSt

to shipping pump 1		
Temperature	37.78	C
Pressure	2.026	bar
Kinematic Viscosity	1.536	cSt

to shipping pump 2		
Temperature	38.06	C
Pressure	12.37	bar
Kinematic Viscosity	1.529	cSt

Figure 3. Case study simulated process flow diagram without retrofit.

Table 2. Material balance for the streams of the process shown in Figure 3.

Stream No.	T (°C)	P (kPa)	Flowrate (kg/h)	Stream No.	T (°C)	P (kPa)	Flowrate (kg/h)	Stream No.	T (°C)	P (kPa)	Flowrate (kg/h)
FEED	48.89	721.85	1008881.9	W222	65.00	73.69	0.00	V2	59.25	487.38	0.0
Gas	48.89	721.85	36231.00	train C	62.66	73.69	28095.74	WWW	59.25	487.38	7906.57
B	48.33	342.64	58695.77	train D	62.66	73.69	42143.62	to storage	59.49	487.38	254655.15
BB.	56.66	273.69	58695.77	des -B pump	63.71	73.69	127590.42	v4	59.49	487.38	0.00
W1	56.66	273.69	0.00	des- B	63.86	487.38	127590.42	product	59.49	487.38	254655.15
L1	56.66	273.69	58233.27	train E	62.66	73.69	56191.49	v6	59.62	219.86	0.0
X1	56.66	273.69	462.50	train F	62.66	73.69	42143.62	1	48.33	342.64	178755.29
X2	56.66	273.69	231.25	des -A pump	63.19	73.69	127010.63	A.	48.33	342.64	29347.88
L2	56.66	273.69	29116.63	des - A	63.33	487.38	127010.63	AA.	56.66	273.69	29347.88
W2	56.66	273.69	0.00	Brackish water to desalter B	48.89	517.08	7933.37	water reinjected into well	48.89	721.85	705851.96
L11	65.00	73.69	58233.27	Brackish water to desalter	30	517.08	7933.37	to shipping	59.62	219.86	254655.15
L22	65.00	73.69	29116.63	oil to desalter B	59.72	487.38	135523.79	to shipping pump 2	38.06	1237.03	254655.15
X111	65.00	73.69	882.20	oil to desalter A	59.25	487.38	134944.00	Oil	48.89	721.85	266798.94
L111	65.00	73.69	57351.07	oil out of desalter B	59.72	487.38	127617.72	O	48.33	342.64	266798.94
W111	65.00	73.69	0.00	WW	59.72	487.38	7906.07	product 1	59.62	219.86	254655.15
L222	65.00	73.69	28675.53	v1	59.72	487.38	0.00	to shipping pump 1	37.78	202.63	254655.15
X222	65.00	73.69	441.10	oil out of desalter A	59.25	487.38	127037.43	pumped oil	40.05	8824.03	254655.15
Brackish water	30	517.08	15866.74								

The heat exchanger is valuable process equipment in an energy-saving field. The importance of a heat exchanger in processing is to recover waste heat in some processing streams and optimize energy consumption. Disposed water has a temperature of 48.89 °C. Energy will be lost with the disposed water injected underground without reusing this energy. Therefore, it will be beneficial if we recover waste heat from produced water exiting the free water knockout drum to the disposal system to be used in heating some process and utility streams as follows:

Heating brackish water used to wash oil in desalters

According to the stock's relation, a reduction in oil viscosity would increase the velocity of the dispersed phase and the efficiency of the two-phase separation. However, an increase in temperature would result in slippage of water droplets, limiting their binding and causing shrinkage. The settling rate of salts in desalter depends highly on temperature as liquid density and viscosity decrease with increasing temperature. It means that increasing the operating temperature will increase the settling rate and therefore increase separation. Separation improvement means a larger quantity can be desalted simultaneously in a given desalter. Heating decreases the viscosity, thickness, and cohesion of the film surrounding the water droplets in the oil. Excessive heating might lead to evaporation which would result in a loss in oil volume, but the reduction in price results from API decrease [29,30]. Heating the brackish water used to wash oil in desalters is achieved through the new heat exchanger 1 (new H. Ex. 1), as presented in Figure 4. It is heated from 30 °C to 71.11 °C by heat exchange with the water outlet from the free water knockout drum. Heating the brackish water to a temperature of 71.11 °C will increase the

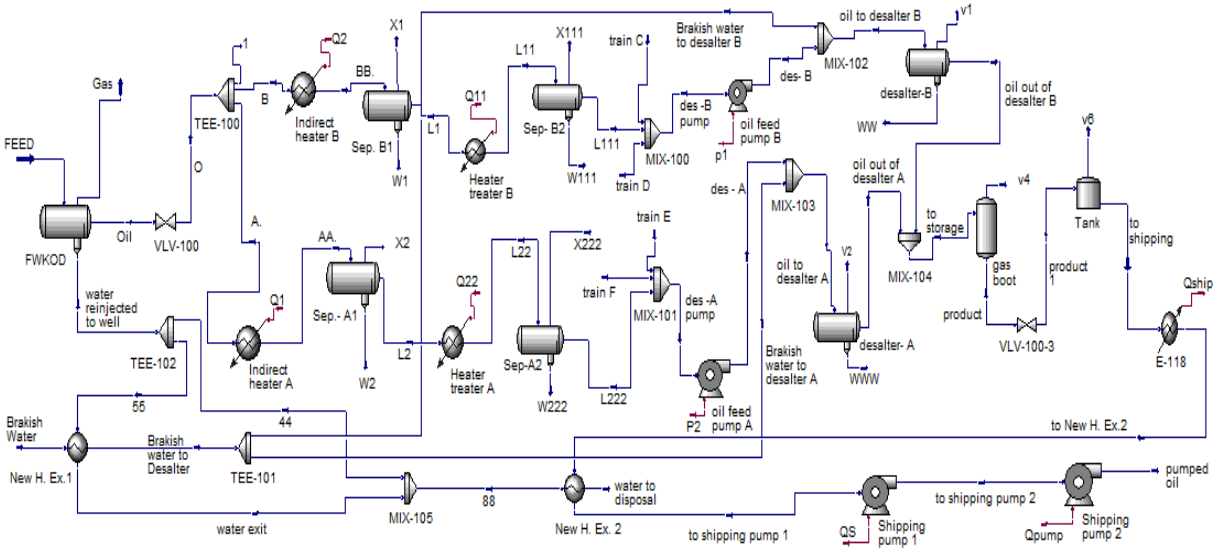

oil out of desalter A		
Temperature	64.03	C
Pressure	487.4	kPa
Kinematic Viscosity	1.062	cSt

oil out of desalter B		
Temperature	64.49	C
Pressure	487.4	kPa
Kinematic Viscosity	1.058	cSt

to shipping pump 1		
Temperature	71.11	C
Pressure	197.6	kPa
Kinematic Viscosity	0.9735	cSt

to shipping pump 2		
Temperature	71.31	C
Pressure	851.9	kPa
Kinematic Viscosity	0.9710	cSt

Figure 4. Case study simulated process flow diagram with proposed retrofit.

desalter operating temperature from 59.25 °C to 64.03 °C for desalter A and from 59.72 °C to 64.49 °C desalter B. Also, the viscosity is lowered from 1.131 cSt to 1.062 cSt. for desalter A and from 1.125 cSt to 1.058 cSt. for desalter B. As a result, the salt's settling rate will increase, and the required retention time inside the desalters will decrease.

Heating crude oil before shipping

The free water out of the knockout drum (FWKOD) is separated into two parts. The first is used to exchange with the brackish water in new H. Ex. 1. The other part is mixed with the first part out of the new H. Ex. 1 to give stream 88. A second new heat exchanger (new H. Ex. 2), as illustrated in Figure 4, is implemented and used to exchange the oil before shipping (to the new H. Ex. 2 stream) with the water stream 88. As a result, the oil temperature before the shipping stream increased from 37.78 °C to 71.11 °C, and the viscosity decreased from 1.536 cSt to 0.9735 cSt. This decrease in viscosity reduced the pressure drop of shipping pump 1 from 1034 kPa to 654.3 kPa. Also, the pressure drop of shipping pump 2 decreased from 7586.51 kPa to 4820 kPa. Therefore, the power consumption of these two shipping pumps decreased. The power consumption of shipping pump 1 decreased from 114.653 kW to 75.135 kW, and the power consumption of shipping pump 2 decreased from 840.1965 kW to 552.101 kW. The power energy savings for shipping pump 1 and shipping pump 2 reached 39.518 kW and 288.0955 kW, with a saving percentage of 34.47% and 34.29%, respectively. Table 3 illustrates the conditions of all streams in the retrofitted simulated process of Figure 4.

Optimization of the retrofitted case study

The optimizer in the HYSYS program is used to get the optimum heating temperatures of the outlet streams of the new heat exchanger 1 (brackish water to desalter) and the new heat exchanger 2 (to shipping pump 1). The objective function is to minimize the power consumption of the shipping pumps. The kinematic viscosity of to shipping pump stream is used as a constraint. It is adjusted below 1.0 cSt. The optimization results showed that the optimum temperature of the outlet streams from the new heat exchangers 1 and 2 is 71.11 °C. An economic study of the proposed retrofit is applied to calculate the capital cost of the new heat exchangers and the saving in operating costs.

Economic study

The economics analyzer in Hysys simulation program V.11 is used to calculate the capital and the operating costs of the case study before and after the retrofit. The results are illustrated in Table 4. In the retrofit design, two shell and tube heat exchangers are installed. This type of heat exchanger is used because most heat exchangers in the oilfield are shell and tube-type exchangers. They are relatively inexpensive and easy to maintain because tube bundles can be removed, cleaned, or replaced if needed [31]. The

Table 3. Material balance for streams of the modified process shown in Figure 4.

Stream No.	T (°C)	P (kPa)	Flowrate (kg/h)	Stream No.	T (°C)	P (kPa)	Flowrate (kg/h)	Stream No.	T (°C)	P (kPa)	Flowrate (kg/h)
FEED	48.89	721.85	1008881.9	W222	65.00	73.69	0.00	V2	64.03	487.38	0.00
Gas	48.89	721.85	36231.00	train C	62.66	73.69	28095.74	WWW	64.03	487.38	7901.15
B	48.33	342.64	58695.77	train D	62.66	73.69	42143.62	to storage	64.26	487.38	254666.06
BB.	56.66	273.69	58695.77	des -B pump	63.71	73.69	127590.42	v4	64.26	487.38	0.00
W1	56.66	273.69	0.00	des- B	63.86	487.38	127590.42	product	64.26	487.38	254666.06
L1	56.66	273.69	58233.27	train E	62.66	73.69	56191.49	v6	64.39	219.86	0.00
X1	56.66	273.69	462.50	train F	62.66	73.69	42143.62	1	48.33	342.64	178755.29
X2	56.66	273.69	231.25	des -A pump	63.19	73.69	127010.63	A.	48.33	342.64	29347.88
L2	56.66	273.69	29116.63	des - A	63.33	487.38	127010.63	AA.	56.66	273.69	29347.88
W2	56.66	273.69	0.00	Brackish water to desalter B	71.11	512.10	7933.37	water reinjected to well	48.89	721.85	705851.96
L11	65.00	73.69	58233.27	Brackish water to desalter A	71.11	512.10	7933.37	to shipping	64.39	219.86	254666.06
L22	65.00	73.69	29116.63	oil to desalter B	64.49	487.38	135523.79	to shipping pump 2	71.31	851.9	254666.06
X111	65.00	73.69	882.20	oil to desalter A	64.03	487.38	134944.00	Oil	48.89	721.85	266798.94
L111	65.00	73.69	57351.07	oil out of desalter B	64.49	487.4	127623.21	O	48.33	342.64	266798.94
W111	65.00	73.69	0.00	WW	64.49	487.38	7900.58	product 1	64.39	219.86	254666.06
L222	65.00	73.69	28675.53	v1	64.49	487.38	0.00	to shipping pump 1	71.11	197.60	254666.06
X222	65.00	73.69	441.10	oil out of desalter A	64.03	487.4	127042.85	pumped oil	63.70	6216.25	254666.06
Brackish water to Desalter	71.11	512.10	15866.74	Brackish Water	30	517.10	15866.74	water exit	47.039	716.85	352925.98
to New H. Ex.2	37.78	202.63	254666.06	44	48.89	721.85	352925.98	55	48.89	721.85	352925.98
88	47.96	716.85	705851.96	water to disposal	42.36	711.85	705851.96				

Table 4. Economic study of the original and the modified case study.

Cost item	Case study before retrofit	Case study after retrofit
Power of shipping pumps	114.653 kW for shipping pump 1	75.135 kW for shipping pump 1
	840.1965 kW for shipping pump 2	552.101 kW for shipping pump 2
Operating cost, $/y	2,247,070	2,026,460
Saving in operating cost, $/yr	220,610	
Total capital cost, $	9,068,420	9,858,630
Increasing in capital cost, $ (new capital needed)	790210	

capital cost of the two new heat exchangers in the proposed retrofit design is estimated from the HYSYS program. Their cost was $790,210. The payoff from the proposed retrofit can be seen in savings in operating costs ($220,610/year), reduced pipeline drag dose, and reduced retention time for crude oil within desalters to reach required specifications.

Reliability of the proposed retrofit

The reliability of the proposed modification depends on the continuous hot water feeding rate and the choice of materials from which the equipment is manufactured as follows: The rate of water produced by FWKOD is large and has a suitable temperature sufficient to heat the brackish water and the oil coming out of the storage tanks, and this ensures that our needs are covered by the rate of hot current; The temperature difference between the hot stream and the cold stream realizes the process of heat transfer; With the aging of production wells, the rate of water production increases and the rate of oil production decreases, and this will make the process more reliable with more water available; The selection of materials from which the devices are manufactured must be taken into account at the design stage so that the heat exchanger, pipes, and control system are suitable for the service fluid to avoid corrosion problems.

CONCLUSION

Using waste heat in water before being reinjected into wells in oilfield plants represents economic value in heating facilities. This paper makes a retrofit to an existing oilfield plant to increase the desalting unit's performance and reduce the facilities' operating costs. The retrofit was based on implementing two new heat exchangers to heat brackish water used in desalters and heat crude oil before shipping. The use of waste heat in brackish water heating was studied to improve the desalters' operating temperature and separation conditions. The results showed an increase in the brackish water temperature and an increase in the operating temperature of the desalter. In addition, it will reduce the viscosity of the oil and improve the sedimentation rate. On the other hand, the waste heat in the disposed water was used to heat the crude oil before shipping. The results showed that the viscosity of the oil decreased. The decrease in viscosity reduced the pressure drop of the shipping pumps and the power consumed to pump oil into the pipeline. Moreover, the drag dose injected through the pipeline will be reduced.

REFERENCES

[1] A. Hart, J. Pet. Explor. Prod. Technol. 4 (3) (2014) 327–336. https://doi.org/10.1007/s13202-013-0086-6.

[2] Y. Al-Roomi, R. George , A. Elgibaly, A. Elkamel, J. Pet. Sci. Eng. 42 (2-4) (2004) 235–243. https://doi.org/10.1016/j.petrol.2003.12.014.

[3] R. Martinez-Palou, M.D.L. Mosqueira, B. Zapata-Rendon, E. Mar-Juarez, C. Bernal-Huicochea, J. de la Cruz Clavel-López, J. Aburto, J. Pet. Sci. Eng. 75 (3–4) (2011) 274–282. https://doi.org/10.1016/j.petrol.2010.11.020.

[4] A. Saniere, I. Henaut, J.F. Argillier, Oil Gas Sci. Technol. 59 (5) (2004) 455–466. https://doi.org/10.2516/ogst:2004031.

[5] R.I. Ibrahim, M.K. Odah, A. Al-Mufti, IOP Conf. Ser.: Mater. Sci. Eng. 579 (1) (2019) 012054. https://doi.org/10.1088/1757-899X/579/1/012054.

[6] R.G. Santos, W. Loh, A. C. Bannwart, O. V. Trevisan, Braz. J. Chem. Eng. 31 (3) (2014) 571–590. https://doi.org/10.1590/0104-6632.20140313s00001853.

[7] S.W. Hasan, M.T. Ghannam, N. Esmail, Fuel 89 (5) (2010) 1095–1100. https://doi.org/10.1016/j.fuel.2009.12.021.

[8] B.M. Yaghi, A. Al-Bemani, Energy Sources 24 (2) (2002) 93–102. https://doi.org/10.1080/00908310252774417.

[9] P. Gateau, I. Henaut, L. Barre, J. F. Argillier, Oil Gas Sci. Technol. 59 (5) (2004) 503–509. https://doi.org/10.2516/ogst:2004035.

[10] M.S. Rana, V. Sa´mano, J. Ancheyta, J.A.I. Diaz, Fuel 86 (2007) 1216–1231. https://doi.org/10.1016/j.fuel.2006.08.004.

[11] N. Shigemoto, R.S. Al-Maamari, B.Y. Jibril, A. Hirayama, Energy Fuels 20 (6) (2006) 2504–2508. https://doi.org/10.1021/ef060074h.

[12] J.J. Wylde, D. Leinweber, D. Low, G. Botthof, A.P. Oliveira, C. Royle, C. Kayser, Proc. World Heavy Oil Congr., Aberdeen, Scottland, Canada Inc (2012).

[13] A. Bensakhria, Y. Peysson, G. Antonini, Oil Gas Sci. Technol. 59 (5) (2004) 523–533. https://doi.org/10.2516/ogst:2004037.

[14] T. Zhou, K.C. Leong, K.H. Yeo, Int. J. Heat Mass Transfer 49 (7-8) (2006) 1462–1471. https://doi.org/10.1016/j.ijheatmasstransfer.2005.09.023.

[15] S.N. Milligan, R.L. Johnston, T.L. Burden, W.R. Dreher, K.W. Smith, DRAG Harris, U.S. Patent Application 8,022,118 B2 (2011). https://patentimages.storage.googleapis.com/dd/4e/8d/8725cef978517d/US8022118.pdf.

[16] Z. Matras, T. Malcher, B. Gzyl-Malcher, Thin Solid Films 516 (24) (2008) 8848–8851. https://doi.org/10.1016/j.tsf.2007.11.057.

[17] R.A. Soldi, A.R.S. Oliveira, R.V. Barbosa, M.A.F. Cesar-Oliveira, Eur. Polym. J. 43 (8) (2007) 3671–3678. https://doi.org/10.1016/j.eurpolymj.2006.07.021.

[18] J. Jing, R. Yin, Y. Yuan, Y. Shi, J. Sun, M. Zhang, ACS Omega 5 (2020) 9870–9884. https://doi.org/10.1021/acsomega.0c00097.

[19] M.T. Ghannam, N. Esmail, Pet. Sci. Technol. 24 (8) (2006) 985–999. https://doi.org/10.1081/LFT-200048166.

[20] C. Chang, Q.D. Nguyen, H.P. Rønningsen, J. Non-Newtonian Fluid Mech. 87 (2–3) (1999) 127–154. https://doi.org/10.1016/S0377-0257(99)00059-2.

[21] E. Worrell, C. Galitsky, Energy Efficiency Improvement in the Petroleum Refining Industry, ACEEE Summer Study on Energy Efficiency in Industry, NY, August (2005) 158–169. https://doi.org/10.2172/862119.

[22] M. Mahinroosta, Review on Energy Efficiency Improvement methods for Oil and Gas Industries, In Proceedings of the

2nd Conference on Emerging Trends in Energy Conservation, Tehran, Iran (2013). https://www.researchgate.net/publication/301221524_A_Review_on_Energy_Efficiency_Improvement_methods_for_Oil_and_Gas_Industries.

[23] E. Yanez, A. Ramírez, A. Uribe, E. Castillo, A. Faaij, J. Cleaner Prod. 176 (2018) 604–628. https://doi.org/10.1016/j.jclepro.2017.12.085.

[24] W. Ping, X. Changfang, X. Shiming, G. Yulin, Procedia Environ. Sci. 12 (2012) 387–393. https://doi.org/10.1016/j.proenv.2012.01.294.

[25] F.M. White, Fluid Mechanics, 7th ed., McGraw-Hill, a business unit of The McGraw-Hill Companies, Inc. (2011). http://ftp.demec.ufpr.br/disciplinas/TM240/Marchi/Bibliografia/White_2011_7ed_Fluid-Mechanics.pdf.

[26] W.S. Janna, Introduction to Fluid Mechanics, 4th ed. CRC Press, Taylor & Francis Group, LLC., (2010). https://doi.org/10.1201/b18979.

[27] S. Sarbjit, Experiments in Fluid Mechanics, 2nd ed., PHI Learning Pvt. Ltd, New Delhi, (2012). ISBN: 9788120345119, 8120345118.

[28] R.I. Ibrahim, M.K. Oudah, A.F. Hassan, J. Pet. Sci. Eng. 156 (2017) 356–365. https://doi.org/10.1016/j.petrol.2017.05.028.

[29] L. Vafajoo, K. Ganjian, M. Fattahi, J. Pet. Sci. Eng. 90–91 (2012) 107–111. https://doi.org/10.1016/j.petrol.2012.04.022.

[30] B.Y. Kim, J.H. Moon, T.-H. Sung, S.-M. Yang, J.-D. Kim, Sep. Sci. Technol. 37 (6) (2002) 1307–1320. https://doi.org/10.1081/SS-120002613.

[31] A.J. Kidnay, W.R. Parrish, D. G. McCartney, Fundamentals of Natural Gas Processing, 3rd ed., CRC Press, Taylor & Francis Group, LLC. (2019). https://doi.org/10.1201/9780429464942.

WALAA MAHMOUD SHEHATA[1]
MOHAMED GALAL HELAL[2]
FATMA KHALIFA GAD[1]

[1]Department of Petroleum Refining and Petrochemical Engineering, Faculty of Petroleum and Mining Engineering, Suez University, Suez, Egypt

[2]Khalda Petroleum Company, Salam Gas Plant, Western Desert, Egypt

NAUČNI RAD

UŠTEDA ENERGIJE NA NAFTNIM POLJIMA KORIŠĆENJEM TOPLOTE OTPADNE VODE

Ovaj rad ima za cilj rekonstrukciju postojećeg egipatskog naftnog postrojenja kako bi se poboljšale performanse odsoljivanja i smanjila snaga pumpi za transport sirove nafte. Toplota otpadne vodi koristi se za zagrevanje slane vode koja se ubrizgava preko odsoljivača i zagrevanje sirove nafte pre otpremanja. Korišćen je softver za simulaciju ASPEN HISIS verzije 11. Rekonstrukcija razmatranog naftnog postrojenja zasniva se na implementaciji dva nova izmenjivača toplote za rekuperaciju otpadne toplote u otpadnoj vodi. Rezultati su pokazali da će korišćenje otpadne toplote za zagrevanje slane vode u odsoljivaču podići radnu temperature sa 30 °C na 71,11 °C i time povećati brzinu sedimentacije i separacije. S druge strane, korišćenje otpadne toplote za zagrevanje sirove nafte pre otpremanja sa 37,78 °C na 71,11 °C će smanjiti viskozitet naftesa 1,536 cSt na 0,974 cSt. Smanjenje viskoziteta sirove nafte će smanjiti pad pritiska pumpi za transport, a samim tim i snagu potrebna za pumpanje nafte. Stoga se predstavljena rekonstrukcija može koristiti kao vodič u nadogradnji postojećih postrojenja i postrojenja u fazi projektovanja.

Ključne reči: odsoljivač, smanjenje viskoziteta, pumpe za transport, sirova nafta, simulacija.

CI&CEQ
Chemical Industry & Chemical Engineering Quarterly

Available online at
Association of the Chemical Engineers of Serbia AChE
www.ache.org.rs/CICEQ

Chem. Ind. Chem. Eng. Q. 29 (2) 129–139 (2023) CI&CEQ

FELIPE ZAULI DA SILVA
IZABELLA CARNEIRO BASTOS

Federal University of Alfenas, Institute of Science and Technology, Poços de Caldas, Minas Gerais, Brazil

STUDY ON HEAT EXCHANGERS AND INDUSTRIAL ABSORPTION COLUMN FOR DRYING POLYETHYLENE TEREPHTHALATE

Article Highlights

- The work consisted of an industrial-scale technical investigation
- The industrial process had no impact on product quality or production rate
- The study aimed at industrial optimization
- The results found can be used as a reference in other processes (diagrams)

Abstract

This study proposes the use of mass balance and the method of McCabe-Thiele in the absorption column for the removal of drying air humidity with ethylene glycol and energy balances in heat exchangers for the determination of the optimum operating conditions of a factory to produce recycled polyester fibers from polyethylene terephthalate (PET) flakes. The evaluation of these machines involved the combination of variables such as temperature, flow rate, specific heat, and operational efficiency to guarantee the correct adjustment of the physicochemical properties of the fluids and materials of the process. The efficiency of the absorption column was determined at 25%, and a diagram correlating ethylene glycol humidity, the dew point of the drying air, and the efficiency of humidity removal from the PET flake dryer were constructed to define what is the most appropriate configuration for operation. By the graph curves, it was found that the humidity of ethylene glycol for absorption should be inferior to 1% (w/w) to guarantee a dew point < -27 °C at 175 °C of the drying air introduced in the dryer, which would finally promote a removal with efficiency superior to 91% of the PET flake humidity for values < 0.005% (w/w).

Keywords: humidity, dew point, PET flakes, polyester, McCabe-Thiele.

SCIENTIFIC PAPER

UDC 678:66.047:678.742.2

The production of recycled polyester fibers (PES) occurs in three steps. Initially, the polyethylene terephthalate (PET) bottles are processed post-consumption in a line for decontamination and granulometry adjustment to obtain the PET flakes. Subsequently, the material undergoes extrusion and spinning and draws and cuts the fiber filaments [1–3].

Before PET flake extrusion, the crystallization and drying of the material must be performed to avoid hydrolytic degradation of the polymer molecules. The residence time required by the polymer in the crystallizer and dryer for thermal treatment to be sufficient to meet the operational requirements, and adjustment of the molecular properties must be enough for the removal of PET flake humidity at levels below 0.005% w/w for extruders without vacuum adjustment, and inferior to 0.05% w/w for extruders with this additional vacuum adjustment [4–5].

The adjustment of the PET drying process must be properly configured to guarantee the removal of humidity from the polymer particles to acceptable levels, especially because of the hygroscopic characteristic of PET and the formation of intermolecular bonds between water molecules and the polymer chain [6]. In Figure 1, the schematic representation of the removal of water molecules that penetrated the PET flake or pellet can be observed following an appropriate drying process.

Correspondence: F.Z. da Silva, Federal University of Alfenas, Institute of Science and Technology, José Aurélio Vilela Road 11999, km 533, Zip Code 37715-400, Poços de Caldas, MG, Brazil.
E-mail: fzaulisilva@gmail.com
Paper received: 22 June, 2021
Paper revised: 8 January, 2022
Paper accepted: 15 August, 2022

https://doi.org/10.2298/CICEQ210622020S

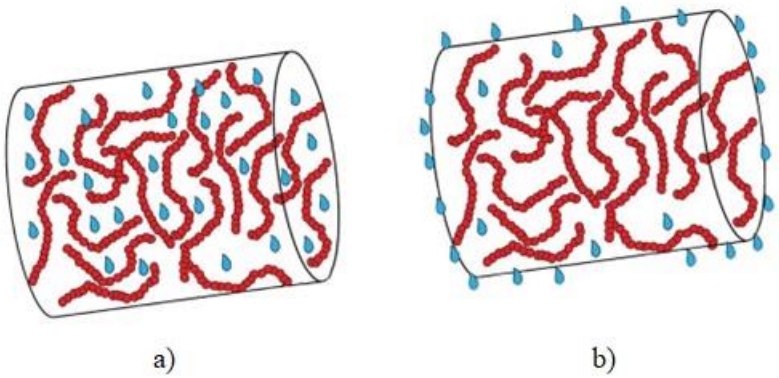

Figure 1. Water molecules penetrated the PET polymeric chain (a) and molecular process of polymeric chain drying (b) according to Plastics Technology® [7].

Virgin PET or recycled PET flakes must be dried immediately before fusion. Four fundamental parameters must be verified: temperature, dew point, drying air flow rate, and operation time. With the temperature rise, water molecules lose attraction to the polymer chains and become prone to migrate to the atmosphere. Nevertheless, the temperature range must be appropriate since the excessive rise favors parallel degradation and thermal oxidation reactions. The dew point is the indirect measurement of air humidity and indicates the temperature of saturation in which the air-water vapor will condense into the first drop of liquid. The lower the dew point, the lower the relative humidity of the drying air; consequently, the higher the drying capacity and efficiency according to the mass transference principles [8–10].

Drying air flow must be properly dimensioned for compatibilization with the dimensions of the system. An insufficient air flow will be unable to transfer the necessary heat in the whole extension of the dryer, thus reducing process efficiency. In contrast, an excessive flow will cause an overload in drying temperature and around the equipment. The PET particles will not absorb this excess heat, and the energy costs and drying performance will not be optimized under this condition. The ideal air flow must provide the system with a vertical profile of homogeneous temperature in the equipment, as presented in Figure 2 [10,11].

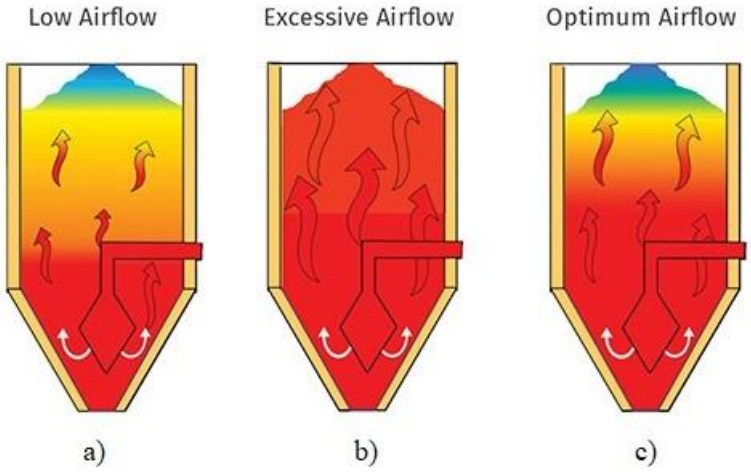

Figure 2. (a) Insufficient airflow will not maintain the necessary heat to dry the PET particles; (b) excessive airflow will provide more heat than PET can absorb, resulting in high air temperatures, unsatisfactory performance of the desiccant, and waste of energy; (c) ideal airflow develops a vertical temperature profile which provides the optimized amount of heat for drying while it uses the cold PET particles as a heat sink to cool the return air coming out of the dryer according to Plastics Technology® [7].

Additionally, the processing time must be high enough since PET drying does not occur instantly. When heat transfer starts on the surface of the material, sufficient time must be provided for internal heat transfer and subsequent elimination of water molecules, which usually occurs between 3 and 5 hours [11,12].

In work on the recycled PET extrusion on an

industrial scale, Elamri [4] used a drying system with air at the temperature of 170 °C and dew point below -20 °C for 4 h, obtaining post-drying PET with humidity of 0.05% (the value was relatively high because of the operation conditions and compensated by the vacuum system coupled to the extruder; otherwise the hydrolytic degradation would reach detrimental levels). On the other hand, Whitehead [12] worked with temperatures varying between 150 °C and 200 °C, a dew point of -20 °C, and an operation time of close to 5 h.

Given the context presented for PET flake drying, the operational conditions of the air to be used in the dryer, especially temperature and humidity, must also be considered for industrial projects. In large-scale installations, heat exchangers and absorption columns for temperature and humidity adjustments can be used, following proper equations and scaling. By definition, heat exchangers are designed for heat exchange between distinct fluids or even between fluids of the same nature, which promote direct or indirect contact among fluids of interest and favor energy transfer [13]. In contrast, absorption columns are based on mass transfer among the components used [14].

The study of polyethylene terephthalate is consolidated in the literature, which is noted by the many studies on this important polymer. However, new approaches and experiments can be found despite being a classic material to study. Furthermore, and within the segment of the present work performed, the PET humidity issue is always a critical variable to be considered for the processing of interest, mainly because of the characteristic molecular degradation that happens in the chains of this polymer when melted in wet conditions [15–17].

In the present work, the projecting and scaling-up equations of heat exchangers and an absorption column were studied for the treatment of the air of a PET flake dryer for polyester production on an industrial scale aiming at evaluating the variables of the operation line of the factory without process interruption. Furthermore, for the studies on mass transfer, experiments to compare the optimum operation conditions were also performed, considering the humidity of the fluid for humidity removal, the dew point of the drying air, and the humidity of the PET flakes before the extruder without a vacuum system.

The main contributions of this work are related to the practical results found on an industrial scale after the execution of the procedures. Typically, pilot scale or laboratory scale studies are found in the literature for this type of evaluation. In summary, the application of chemical engineering models could be observed in industrial operations and provide a view of the behavior of the related principles.

EXPERIMENTAL

A detailed description of the process

The process consisted of receiving amorphous recycled PET flakes (with dimensions inferior to 9 mm) directed to a supply silo by transportation in the compressed air tubing. The material was sequentially transported to the crystallizer by vacuum, where, by gravity, the flakes flowed into the equipment. By the action of temperature and agitator shear stress, crystallization occurred. The heating was derived from hot air at (160 ± 10) °C. At the outlet of the crystallizer, there was a blower to direct the material to the dust removal system, composed of one cyclone and bag filter for the filtration of air and retention of contaminating particles.

The material flow of the dust removal system was transported in a vacuum line to two serial feed silos on top of the dryer, designed to keep the constant flow in the drying step and avoid feeding failure. After the dryer outlet, the material followed the gravimetric measurement system, which had four dosing points loaded with different materials, such as masterbatches for pigmentation of molten polymer and specific additives according to the type of polyester to be processed before passing through the extruder.

The extruder was basically composed of the feeding zone, six zones for heating with electrical resistances varying between 255 °C and 280 °C, a shear bolt, and a rotary polymer filter to retain unwanted impurities for the next spinning process. The feeding system was continually cooled with cold water at 5 °C to prevent softening and possible adsorption of the flakes on the inner walls of the feeding zone. In the horizontal extent of the extruder, the heating system should be increasing, with the recommendation of 10 °C below the melting temperature of (250 ± 5) °C in the first zone, the temperature in the melting range of (260 ± 5) °C in the second zone, and from the third zone, 10 °C above the melting temperature of (275 ± 5) °C. This temperature profile aimed at avoiding backflow at the extruder inlet and favoring the screw shear stress, considering that this extruder model did not have a vacuum system for the transportation and flow of the molten material [18].

The molten polymer was directed to the spinning machines by metering pumps, which distributed the polymeric mass evenly for the passage by compression through 20 filter devices containing spinnerets with up to 1804 holes on the order of 2.5×10^{-4} m in diameter to obtain polyester filaments. Immediately after the spinnerets, there was a fast cooling of the threads with compressed air for the solidification of the material [19].

Subsequently, the spun material was taken to the drawing stage for molecular chain orientation with steam at (175 ± 5) °C because the fast cooling in the spinning caused the molecular disorientation of the polymer. In the drawing process, the polyester threads were pulled to shape the material's mechanical properties and cut to lengths from 32 mm to 64 mm for final product shaping.

In Figure 3, an overview of the process of obtaining polyester fibers by recycling PET bottles is presented as a highlight for the dryer, described in detail in the following study section on mass and energy exchange.

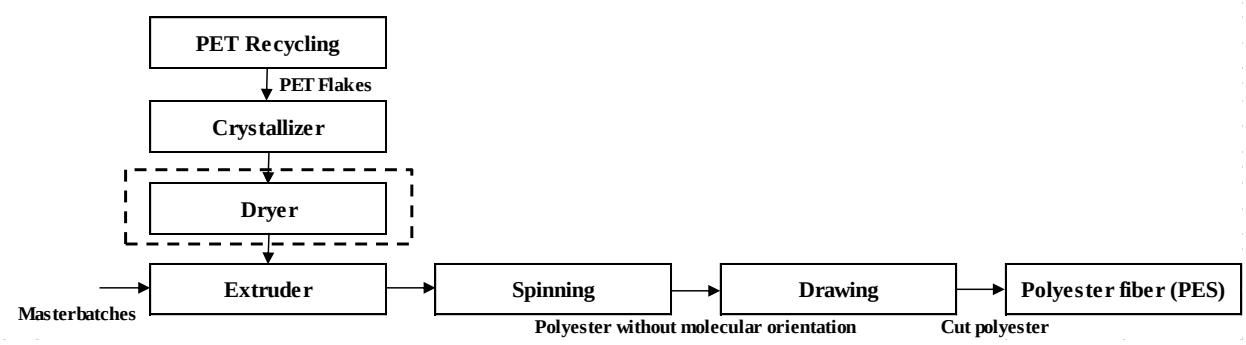

Figure 3. General description of the process of obtaining polyester fibers from PET flakes with the highlight for the dryer where the studies on mass exchange and energy exchange were performed.

Operation parameters for drying PET flakes

To improve the performance of filament spinning, the material underwent treatments before being extruded and receiving the pigmentation of masterbatches, which were the crystallization of the flakes (until ~35%) and drying at (175 ± 25) °C [11].

The dryer had a total volume of 10 m^3, the mass flow of PET flake operation in (700 ± 200) kg/h, and airflow at (1080 ± 30) kg/h at (175 ± 25) °C and with a dew point of approximately (-35 ± 7) °C. The air of the process circulated in a closed circuit, with occasional periodic replacements in cases of pressure drop.

From the dryer outlet, the humid air at about (75 ± 10) °C passed through a cyclone and a paper filter element to remove coarse particles and proceeded to an absorption column for washing with ethylene glycol spray. Ethylene glycol was refluxed at (3000 ± 50) kg/h with a tubular heat exchanger (the cold fluid was cold water at (5 ± 1) °C) to keep the temperature at (10 ± 1) °C, and ethylene glycol had replacement every time the dew point of the drying air was greater than -20°C.

The outlet air from the absorption column, with a temperature of (15 ± 5) °C, was directed to a demister. The contaminants were discarded as overflow, and the airflow was left through the top of the equipment. Then, the purified air passed through a blower and was directed to a heat exchanger of the type shell and tubes, with saturated steam at (210 ± 10) °C as heating fluid, before its dew point was measured by a sensor (RHT-WM sensor from Novus®) and it passed by the dryer. Finally, the humid air after drying was reused for cycle restart (around 75 °C).

Figure 4 presents the simplified block diagram of the drying air system used in the process. In this diagram, it is possible to visualize all the interconnections of the plant's operational streams (flow of PET flakes for extrusion, closed circuit drying air, and ethylene glycol reflux). Additionally, when the diagram is observed, it is possible to understand the applicability of this energy integration study and how to design the equipment and flows.

The process setups can be seen in Table 1, with a summary of the conditions adopted in each step and the possible acceptable variations in operation. In addition, the parameters calculated by the project equations and determined by the dimensioning studies as a function of the plant's operating assumptions were also indicated.

Sizing of the heat exchanger

The equations of Incropera [13] were used to calculate the operation parameters of the heat exchangers, highlighting the considerations for energy balance.

$$Q = \dot{m} \cdot c_p \cdot \Delta T \quad (1)$$

where Q is the heat transfer rate (J/s), $\dot{m}$ is mass flow (kg/s), c_p is the specific heat (J/(kg °C)), and ΔT is the temperature variation of the hot fluid (reference fluid) (°C), Also,

$$Q = U \cdot A \cdot \Delta T_{LMTD} \quad (2)$$

where U is the overall heat transfer coefficient (J/(s m^2 °C)), A is the heat exchange area (m^2), and ΔT is the logarithmic mean temperature difference of

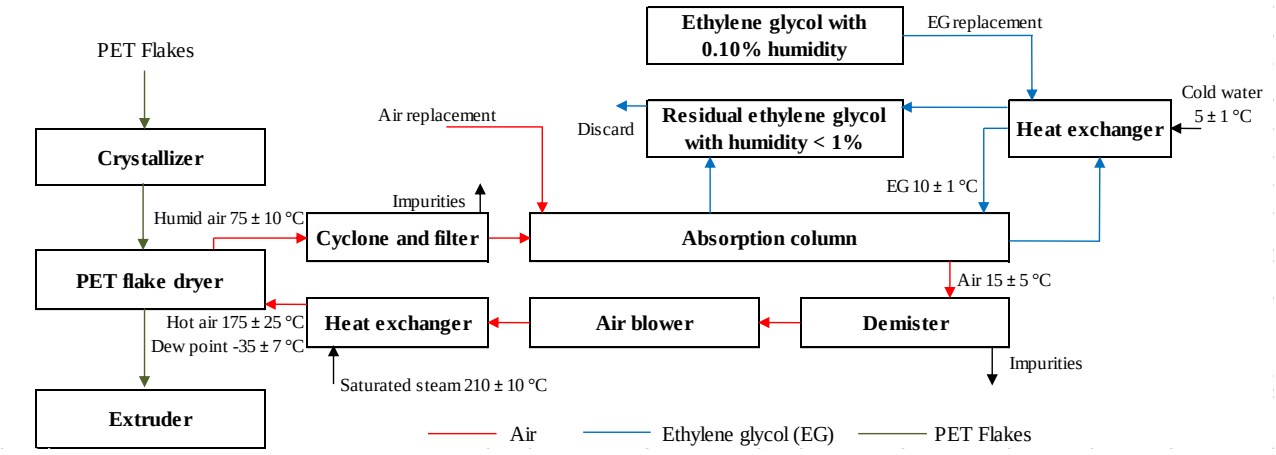

Figure 4. Simplified block diagram of the drying air system.

Table 1. Summary of the conditions adopted in each step and acceptable variations in operation.

Equipment	Parameter	Acceptable Variance + Uncertainty
Crystallizer	Flow - PET Flakes (kg/h)	700 ± 200
	Temperature (°C)	160 ± 10
Dryer	Flow - PET Flakes (kg/h)	700 ± 200
	Flow - Air (kg/h)	1080 ± 30
	Air Temperature at the inlet (°C)	175 ± 25
	Air Dew point at the inlet (°C)	-35 ± 7
	Air Temperature at the outlet (°C)	75 ± 10
Extruder	Flow - PET Flakes (kg/h)	700 ± 200
	Temperature - First Zone (°C)	250 ± 5
	Temperature - Second Zone (°C)	260 ± 5
	Temperature - Third Zone (°C)	275 ± 5
Absorption Column	Flow - Ethylene glycol (kg/h)	3000 ± 50
	Flow - Air (kg/h)	1080 ± 30
	Ethylene glycol Temperature at the inlet (°C)	10 ± 1
	Ethylene glycol Dew point at the inlet (°C)	< -20°C
	Ethylene glycol Temperature at the outlet (°C)	Determined in the dimensioning study
	Air Temperature at the inlet (°C)	75 ± 10
	Air Temperature at the outlet (°C)	15 ± 5
	Heat exchange area (m^2)	15.0 ± 0.5
Bitubular Heat exchanger	Flow - Ethylene glycol (kg/h)	3000 ± 50
	Flow - Water (kg/h)	Determined in the dimensioning study
	Temperature cold fluid water at the inlet (°C)	5 ± 1
	Temperature hot fluid Ethylene glycol at the outlet (°C)	10 ± 1
	Ethylene glycol Dew point at the outlet (°C)	< -20°C
	Flow - Air (kg/h)	1080 ± 30
Shell and tubes Heat exchanger	Flow - Saturated steam (kg/h)	Determined in the dimensioning study
	Air Temperature at the inlet (°C)	15 ± 5
	Saturated steam Temperature at the inlet (°C)	210 ± 10
	Air Temperature at the outlet (°C)	175 ± 25
	Saturated steam Temperature at the outlet (°C)	Determined in the dimensioning study
	Heat exchange area (m^2)	Determined in the dimensioning study
Boiler	Saturated steam production capacity (kg/h)	Up to 1260

the system involving the hot fluid and the cold fluid (°C).

The correction factors based on algebraic equations that consider the fluid temperatures and the counter-current flow operation could also be applied and the heat transfer rates of the exchangers could be determined using the method E-NTU (effectiveness) consulting the tables and graphs available in Incropera [13] for tubular and shell and tubes heat exchangers. The correction factor must be applied to shell and tube heat exchangers with more than one pass in the shell

or tubes because, depending on the design of the equipment, the fluid may sometimes be in counter-current flow and, at other times, in co-current flow. Because counter-current flow is the most efficient heat exchange compared to co-current flow, the correction factor will be applied to correct the energy balance in the counter-current heat exchanger equation when the flow is co-current [13].

Sizing of the absorption column

To determine the theoretical and actual plates of the absorption column to remove air humidity using a chain of ethylene glycol, the mass balance from Eq. (3), cited by Welty [14], and the method of McCabe-Thiele, were employed:

$$L'\left(\frac{x_0}{1-x_0}\right)+V'\left(\frac{y_{n+1}}{1-y_{n+1}}\right)=L'\left(\frac{x_n}{1-x_n}\right)+V'\left(\frac{y_1}{1-y_1}\right) \quad (3)$$

where L is the liquid flow in the absorption column (kmol/(h m^2)), V is the flow of steam or gas (kmol/(h m^2)), and x and y are molar fractions of the contaminants to be removed in the respective phases.

The dew point measurement was performed to evaluate the efficiency of removal of air humidity by the absorption column, where the lowest value indicated the highest removal of moisture (water) by mass exchange with ethylene glycol. Additionally, other evaluations performed were the measurement of PET flake humidity by the method of gravimetry before and after the dryer to correlate humidity removal from the polymer with the different conditions of the drying air dew point and also to correlate the drying air dew point with ethylene glycol humidity in the column (the last was analyzed by an automatic titrator using the Karl Fischer solution) [19–22].

PET flake humidity was analyzed after weighing (10.00 ± 0.50) g of sample in stainless steel capsule and leaving it in a convection oven for 180 min at (175 ± 1) °C. Eq.(4) indicates the calculation to quantify this parameter [6,23].

$$Humidity\,(\%)=\frac{m_{ca}-m_{cv}}{m_{ca}-m_{cas}}\cdot 100 \quad (4)$$

where m_{ca} is the mass of the capsule with the wet sample (g), m_{cv} is the mass of the empty capsule (g) and m_{cas} is the mass of the capsule with the dry sample (g).

At the end of the study, a mass correlation curve was also determined between the dew point and the amount of water vapor per cubic meter of air, considering the characteristics of the drying system, such as atmospheric pressure, relative humidity, and room temperature, using a measurement system integrated to the operation line. For this analysis, the air was left to reflux without renewal, so its humidity increased during the test [24].

RESULTS AND DISCUSSION

Sizing of heat exchangers

An important premise to be considered in the studies is that all dimensioning and data collection were performed in the industry. Therefore, the repetition of experimental conditions simulating different variations was not performed not to impact productivity and quality control of the finished goods (differently than in a laboratory where the data could be varied without loss of productivity).

Nevertheless, all the variation in the data and variables presented in the results section was appropriately statistically analyzed. In addition, the associated measurement uncertainty variation was reported, which was also considered in the factory production standards for monitoring by the production operators. For all the temperatures cited, measuring sensors of the Pt-100 type (Novus model® N1030-pr Pt100) were used to confirm the data obtained by the design equations.

According to Figure 4, presented in the experimental section, the present work was performed in a high-productivity industrial factory with interconnection between the process steps. The first stage of drying air heat exchange after passing through the dryer occurred directly in the absorption column since the contact with ethylene glycol promoted thermal exchange between the fluids. Although the absorption column was not designed as the heat exchanger, we can do an energy balance and determine what mean temperature the air should have at the outlet of the column and allow a comparison with the measurements of the process sensors. The process measurements indicated that the air left the dryer at a flow rate of (1080 ± 30) kg/h at (75 ± 10) °C (called moist air), whereas the counterflow of ethylene glycol in the column was (3000 ± 50) kg/h at (10 ± 1) °C. At the end of the heat exchange, the air left the absorption column at (15 ± 5) °C, and ethylene glycol stayed at (20 ± 5) °C.

The process flow rates were used to calculate the theoretical fluid temperatures for analyzing the absorption column as a heat exchanger. First, after comparing the sensors' measurements, the parameters of the heat exchange area and overall heat transfer coefficient were estimated. Then, performing the necessary balances and considerations, such as energy losses to the environment, temperature variation during the day, the sensitivity of the measurement sensors, and starting from a theoretical heat exchange area of (15.0 ± 0.5) m^2 (according to the

column dimensions) and overall heat transfer coefficient at (50 ± 2) J/(s m^2 °C), the theoretical air outlet temperature should be (20 ± 5) °C. In contrast, ethylene glycol should leave the process at around (18 ± 5) °C [25].

There was a difference of 5 °C between the theoretical and actual outlet air temperatures, which could be attributed to the heat exchange area and, indirectly, to the overall heat transfer coefficient since it is also a function of the area. An iteration method showed that the heat exchange area inside the column could be up to 40% higher than the estimated initial value, which, in practical terms, represents the possibility of increasing the flow rate of fluids in the drying process in case there is a higher production demand at the factory. For ethylene glycol, a difference of 2 °C was verified. After iterations, this difference was 1 °C, which could be attributed to this fluid's higher heat capacity than the air [13].

Evaluating the tubular heat exchanger applied to maintain ethylene glycol in the range of 10 °C, cold water at 5°C was used to perform this energy exchange. In this analysis node, once more, the area of heat exchange and overall heat transfer coefficient could be analyzed; nevertheless, since this equipment is designed for heat exchange, more in-depth studies began since the area, in this case, would be intrinsic to the number of tubes and passes inside the exchanger. Thus, aiming to expand the vision of operation engineering of the factory, energy balances were performed to determine the cold-water flow at 5 °C that should be fed to the heat exchanger to cool the ethylene glycol outlet in the absorption column to return its temperature to 10 °C before entering the absorption column again.

As a premise of the previous analysis, it was also considered that the water leaving the heat exchanger could be reused in another activity of the factory, such as the preparation of process additives, whose ideal temperature of applicability was 20 °C. In an initial evaluation, it can be concluded that the final water temperature should reach the initial temperature of ethylene glycol, which would imply that even if the specific heats of these fluids are different, the water flow should be lower when compared to the flow of ethylene glycol air [13]. Transforming this empirical analysis to numbers from the energy balance, the water flow should be (1164 ± 20) kg/h (ethylene glycol was (3000 ± 50) kg/h), which is equivalent to 1.16 m^3 of water per hour of production.

Finally, for the last heat exchanger to heat the air before the drying process, there was an exchanger of the shell and tube type (with 1 pass in the shell and 2 passes in the tubes), in which the hot fluid available was steam saturated at (210 ± 10) °C from a boiler with a capacity of up to 1260 kg/h of steam. For this evaluation, we aimed to determine what area of minimum heat exchange should be available in this equipment for steam to remain in the saturation condition and with a temperature between 170 °C and 180 °C, which would allow its outflow to be directed to the step of drawing the polyester fibers and orientation of the filaments [26]. Therefore, combining all process considerations and limitations, it was calculated that the equipment should have a heat exchange area of at least 5.9 m^2, the flow rate of the steam saturated at (210 ± 10) °C should be (1115 ± 18) kg/h, and its outlet temperature for use in the drawing stage should be (175 ± 5) °C.

Evaluation of mass transfer in the absorption column

As previously mentioned, there was a heat exchange between the drying air and ethylene glycol in the absorption column. Nevertheless, the column's primary function was removing humidity from the dryer outlet air before its reuse in a new drying cycle in combination with the new air derived from the blower. Ethylene glycol, used in the absorption column for the removal of air humidity, is a highly desiccant agent because of its hygroscopicity (the solubility of ethylene glycol in water at 10 °C is close to 1 g/ml, which gives a degree of solubility of approximately 100%) [27]. Furthermore, ethylene glycol has a relatively high boiling temperature (197.3 °C), which allows the subsequent separation from water in a distillation column or reuse of this raw material in processes in which humidity is not a determining factor [28].

Pure ethylene glycol presented in its mean composition around 0.1% (w/w) of water (humidity), and during the experiments, an output current with up to 8% (w/w) of humidity was observed. Using the mass balance equation for the absorption column and with the flow rates used for process operation, it was possible to estimate the efficiency of the plates in the absorption column using the method of McCabe-Thiele [14] comparing the number of actual plates in relation to the theoretical amount for the development found in the experiment. After drawing the operation curves and counting the degrees of the curves and molar fractions of water in the air and ethylene glycol currents, the mean efficiency determined for the column was 25% [29].

In addition to the calculation of the efficiency of the plates in the absorption column, we performed the analysis of the optimum operation conditions regarding the amount of humidity in ethylene glycol, the effects on the measurements of the drying air dew point, and, mainly, what are the effects on PET flake humidity at

the dryer outlet. During the experiment, 11 different conditions of ethylene glycol humidity were tested, with interruption of the replacement with pure material for higher humidities, maintaining only the reflux. Furthermore, PET flake humidity was measured using a gravimetry method, ethylene glycol humidity with an automatic titrator using the Karl Fischer solution, and the dew point of the drying air was continually measured with process sensors [4].

As cited by Elamri [4] and Jabarin and Lofgren [5], the humidity of PET-based polymers before passing by the extrusion process must be at levels inferior to 0.005% (w/w) in case they pass through extruders without vacuum adjustment to avoid molecular degradation. In a thermodynamic analysis, according to studies presented by Silva [17], PET flakes, after going through the extrusion process, can lose up to 0.200 dl/g of intrinsic viscosity (approximately 25% decrease compared to the original PET flake used as raw material) due to thermal and oxidative molecular reactions. However, this viscosity reduction can be higher. Moreover, an additional decrease of 0.010 dl/g happens for each 0.002% moisture content, which impairs the quality of the final product, mainly because of adjustments in the mechanical properties of polyester fibers (especially tenacity and toughness).

With the PET humidity reference during the drying process to be achieved to ensure polymer quality, it was experimentally determined that the humidity of ethylene glycol should be inferior to 1% (w/w) to obtain the air outlet current with a dew point below -27 °C, so that at the end of the drying process, with all flow rates established in the study, the PET flakes in the dryer output current had humidity inferior to 0.005% (w/w), which, considering the PET flakes input current, corresponding to an efficiency of removal of humidity superior to 91%.

Visualization of the humidity removal efficiency of PET flakes in the dryer (superior to 91% if the best experimental condition is used) as a function of the dew point of the drying air, a summary of different experimental conditions can be seen in Table 2. It is important to note that each condition of drying air was obtained by a different condition of the ethylene glycol used in the absorption column (by the concept of mass exchange, the more humid the ethylene glycol, the highest the dew point of the drying air and consequently the lower the drying efficiency of the PET flakes). The ethylene glycol humidity was measured with an automatic titrator with Karl Fisher's solution, the dew point was measured with an RHT-WM sensor from Novus®, the humidities of the PET flakes were calculated using Eq. (4), and the humidity removal efficiency of the PET flakes was a comparison between before and after the dryer.

Table 2. Evaluation of humidity removal efficiency of PET flakes as a function of drying air conditions.

Run	Ethylene glycol humidity (%)	Air Dew point (°C)	Humidity Flakes before the Dryer (%)	Humidity Flakes after Dryer (%)	Humidity Removal Efficiency of PET flakes (%)
1	8.02 ± 0.03	-3.35 ± 0.07	0.057 ± 0.002	0.012 ± 0.001	78.1 ± 2.8
2	6.78 ± 0.03	-4.53 ± 0.07	0.055 ± 0.002	0.010 ± 0.001	80.3 ± 2.8
3	6.03 ± 0.03	-6.35 ± 0.07	0.055 ± 0.002	0.009 ± 0.001	82.3 ± 2.9
4	5.55 ± 0.03	-9.52 ± 0.07	0.055 ± 0.002	0.008 ± 0.001	83.9 ± 2.0
5	3.07 ± 0.03	-17.97 ± 0.11	0.049 ± 0.002	0.007 ± 0.001	84.9 ± 2.1
6	2.85 ± 0.03	-23.27 ± 0.11	0.049 ± 0.002	0.006 ± 0.001	86.2 ± 2.2
7	1.74 ± 0.03	-25.42 ± 0.11	0.055 ± 0.002	0.005 ± 0.001	89.5 ± 2.2
8	1.10 ± 0.03	-27.85 ± 0.11	0.058 ± 0.002	0.004 ± 0.001	91.6 ± 2.3
9	0.65 ± 0.03	-32.32 ± 0.13	0.053 ± 0.002	0.004 ± 0.001	91.9 ± 2.3
10	0.48 ± 0.03	-34.30 ± 0.13	0.053 ± 0.002	0.004 ± 0.001	92.2 ± 2.4
11	0.10 ± 0.03	-38.37 ± 0.13	0.052 ± 0.002	0.003 ± 0.001	93.2 ± 2.4

For graphical visualization and synthesis of the information, we can observe from the graphs in Figure 5 that the lower the ethylene glycol humidity in the absorption column, the lower the dew point of the drying air that will leave the absorption column after the counter-current and consequently the better the moisture removal efficiency of the PET flakes in the dryer.

Figure 5 verifies that the rise in ethylene glycol humidity increased the air dew point and reduced the efficiency of PET flake drying. Since it was possible to reuse ethylene glycol in another process in which humidity did not cause detrimental effects to the product, discarding and renovating this component was an essential factor in process control. Nonetheless, it is worth highlighting that other parameters influence the

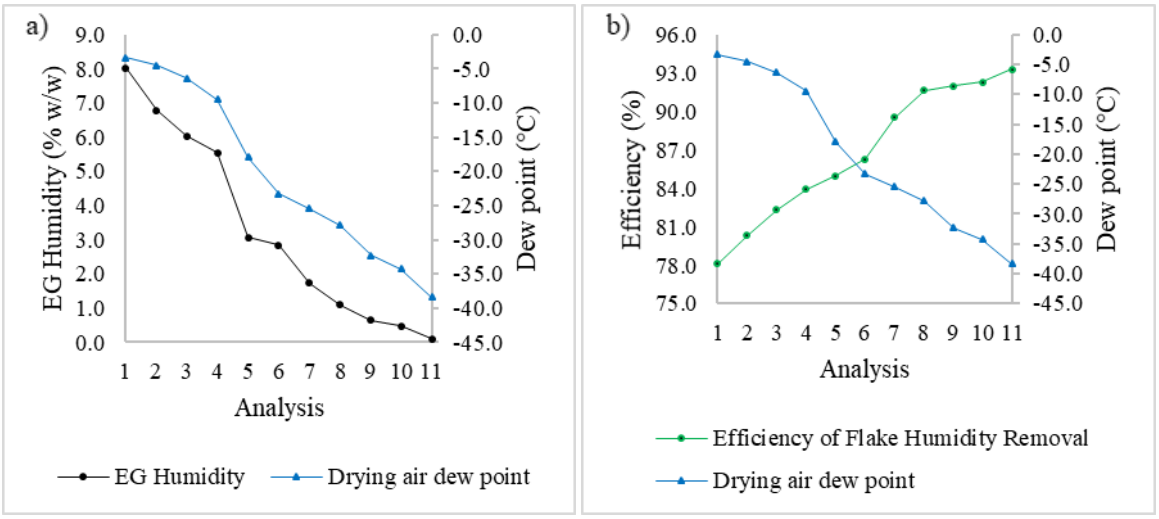

Figure 5. Correlations between (a) ethylene glycol humidity and drying air dew point; (b) drying air dew point and efficiency of PET flake humidity removal.

dew point, such as air temperature, pipe impurities, and the efficiency of the column's mass exchange [14].

Finally, after the energy and mass balances of the proposed study, the construction of a curve between the dew point and the amount of water vapor per cubic meter of air was performed at 175 °C considering a relative air humidity between 40% and 50% at an altitude of approximately 1260 m above sea level (Figure 6). This study provided data that enable equating the mass balance of PET flake humidity removal by the drying action of hot air and with low dew point, besides proving with mass data why a drying air with low dew point (lower amount of water present) presents higher efficiency of humidity removal from solid particles even being at high temperatures [24].

Figure 6 shows the model described by Eq. (5), allowing the extraction of the water vapor present in the air depending on the dew temperature of the drying air. The combination of heating and a low dew point of the drying air will promote a process of mass transfer from the particle to be dried from the mass exchange with the air [14]. In the case of PET, when the flakes are surrounded by air with a dew point < -27 °C at 175 °C, the vapor pressure differential between the surface of the flakes and the drying air will be strengthened, and once the polymer is heated and the attraction between the water molecules and the polymer chains is sufficiently reduced, the water molecules will be released, starting the migration toward the surface of the flakes, which are rapidly dragged through the air:

$$Mass\ of\ steam\ in\ the\ air\left(g/m^3\right) = 4.437e^{0.067 \cdot T_{dp}} \quad (5)$$

where the mass of steam in the air is obtained in g/m^3, T_{dp} is the temperature of the dew point of the air (°C)

For the developed model, it becomes possible to compare the saturated vapor, relative humidity, and absolute humidity equations to obtain the amount of water vapor in the drying air under the drying condition studied. Furthermore, comparing with the correlations, models, and tables presented in the ASHRAE Handbook of Fundamentals [30], it was possible to verify that Eq.(5) is in accordance with the thermodynamic models present in the literature, that is, it can be used within the conditions studied for determining the amount of vapor in the air.

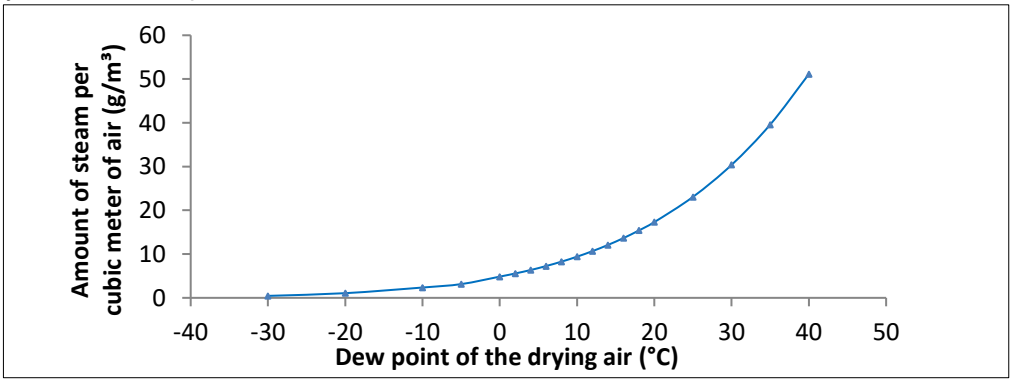

Figure 6. Correlation between dew point and amount of steam per cubic meter of air.

CONCLUSION

In this work, it was possible to apply the concepts of mass and energy transfer in the study of the process variables of a factory for the production of recycled polyester fibers. By analyzing the heat exchangers and absorption column, temperature, flow rates, and operational efficiencies were obtained to guarantee the properties of the PET flakes used as process raw materials. As important points, the efficiency of the absorption column plates was determined at 25%. Furthermore, the humidity of ethylene glycol for absorption should be inferior to 1% (w/w) to guarantee a dew point < -27 °C at 175 °C of the drying air introduced in the dryer, which finally promoted the removal of 91% of PET flake humidity for values < 0.005% (w/w). Finally, a model to determine the amount of water vapor present in the drying air was also obtained as a function of its dew point temperature, which provided data for a future mass balance equation considering the mass exchange between the PET flakes and the drying air.

ACKNOWLEDGMENTS

This study was financed in part by the Coordenação de Aperfeiçoamento de Pessoal de Nível Superior – Brazil (CAPES) – Finance Code 001.

REFERENCES

[1] A.M. Al-Sabagh, F.Z. Yehia, G. Eshaq, A.M. Rabie, A.E. ElMetwally, Egypt. J. Pet. 25 (2016) 53–64. https://doi.org/10.1016/j.ejpe.2015.03.001.

[2] J.C.T. Picazo, J.G.L. Bárcenas, A.G. Chávez, R.G. Nuñez, A.B. Petriciolet, C.A. Castillo, Fibers Polym. 15 (2014) 547–552. https://doi.org/10.1007/s12221-014-0547-7.

[3] J. Scheirs, T.E. Long, Modern Polyesters: Chemistry and Technology of Polyesters and Copolyesters, John Wiley & Sons Ltd, Chichester (2003), p. 44–54. ISBN: 978-0-471-49856-8.

[4] A. Elamri, K. Abid, O. Harzallah, A. Lallam, Am. J. Nano Res. Appl. 3 (2015) 11–16. https://doi.org/10.11648/j.nano.s.2015030401.13.

[5] S.A. Jabarin, E.A. Lofgren, J. Appl. Polym. Sci. 32 (1986) 5315–5335. https://doi.org/10.1002/app.1986.070320607.

[6] H. Lobo, J.V. Bonilla, Handbook of Plastics Analysis, Marcel Dekker, Inc. New York (2003), p. 101–105. https://doi.org/10.1201/9780203911983.

[7] Plastics Technology, How to Dry PET for Container Applications,(2014). https://www.ptonline.com/articles/how-to-dry-pet-for-container-applications.

[8] B. Demirel, A. Yaraş, H. Elçiçek, BAÜ Fen Bil. Enst. Dergisi Cilt 13 (2011) 26–35. https://acikerisim.bartin.edu.tr/bitstream/handle/11772/1592/33-52-1-SM.pdf?sequence=1.

[9] M. Zanin, S. D. Mancini, Resíduos plásticos e reciclagem: aspectos gerais e tecnologia, EdUFSCar, São Carlos, (2015), p. 82–87. https://doi.org/10.7476/9788576003601.

[10] J.D. Seader, E.J. Henley, D.K. Roper, Separation Process Principles: Chemical and Biochemical Operations, 3th Ed., John Wiley & Sons, (2011), p. 111–113. https://imtk.ui.ac.id/wp-content/uploads/2014/02/Separation-Process-Principles-Third-Edition.pdf.

[11] A.S. Mujundar, Handbook of Industrial Drying, 4th Ed., CRC Press New Jersey (2015), p. 204–207, https://doi.org/10.1201/b17208.

[12] B.D. Whitehead, Ind. Eng. Chem. Process Des. Dev. 16 (1977) 341–346. https://doi.org/10.1021/i260063a017.

[13] F.P. Incropera, D.P. Dewitt, T.L. Bergman, A.S. Lavine, Fundamentos de Transferência de Calor e de Massa, LTC, (2012), p. 427–430. http://ftp.demec.ufpr.br/disciplinas/TMEC030/Prof_Luciano/Fundamentos-de-transferencia-de-calor-e-de-massa-incropera.pdf.

[14] J.R. Welty, C.E. Wicks, R.E. Wilson, G.L. Rorrer, Fundamentals of Momentum, Heat, and Mass Transfer, John Wiley & Sons, (2008), p. 142–150. ISBN: 978-0470128688.

[15] C. Lambré, J.M.B. Baviera, C. Bolognesi, A.Chesson, P.S. Cocconcelli, R.Crebelli, D.M. Gott, K. Grob, M. Mengelers, A. Mortensen, G. Rivière, I.-L. Steffensen, C. Tlustos, H. Van Loveren, L. Vernis, H. Zorn, V. Dudler, M.R. Milana, C. Papaspyrides, M. de Fátima Tavares Poças, A. Lioupis, R. Marano, E. Lampi, EFSA J., 19 (2021) 6791–6804. https://doi.org/10.2903/j.efsa.2021.6791.

[16] I.S. Al-Haydari, H.S. Al-Haidari, IOP Conf. Ser.: Mater. Sci. Eng. 870 (2020) 1–9. https://doi.org/10.1088/1757-899X/870/1/012073.

[17] F.Z. Silva, I.C. Bastos, R.F. Perna, S.A.V. Morales, Chem. Ind. Chem. Eng. Q. 27 (2021) 289–298. https://doi.org/10.2298/CICEQ200121047Z.

[18] M. Ahani, M. Khatibzadeh, M. Mohseni, Nanocomposites 2 (2016) 29–36. https://doi.org/10.1080/20550324.2016.1187966.

[19] A. Telli, N.J. Özdil, J. Eng. Fibers Fabr. 10 (2015) 47–60. https://doi.org/10.1177/155892501501000206.

[20] E. Tavcar, E. Turk, S. Kreft, J. Anal. Methods Chem. (2012) 379724. https://doi.org/10.1155/2012/379724.

[21] M. Margreth, R. Schlink, A. Steinbach, Water Determination By Karl Fischer Titration. Analysis and Pharmaceutical Quality, John Wiley & Sons, (2010), p. 22–24. https://doi.org/10.1002/9780470571224.pse415.

[22] E. Scholz, Karl Fischer Titration Determination of Water, Springer-Verlag Berlin Heidelberg, (1984), p. 31–33. https://doi.org/10.1007/978-3-642-69989-4.

[23] M. Saçak, N. Bastug, M. Talu, J. Appl. Polym. Sci. 50 (1993) 1123–1129. https://doi.org/10.1002/app.1993.070500702.

[24] M.G. Lawrence, Am. Meteorol. Soc. (2005) 225–233. https://doi.org/10.1175/BAMS-86-2-225.

[25] M. Olbricht, A. Luke, Heat Mass Transfer 55 (2019) 81–93. https://doi.org/10.1007/s00231-018-2363-x.

[26] K. Senthilkumar, I. Siva, J.J.T. Winowlin, M. Vikneshwararaj, J. Chem. Pharm. Sci. 7 (2015) 172–174. http://www.jchps.com/specialissues/Special%20issue%207/43%20MITNC-48%20K.%20Senthilkumar%20172-174.pdf.

[27] W.M. Haynes, T.J. Bruno, D.R. Lide, CRC Handbook of

Chemistry and Physics, CRC Press/Taylor and Francis (2016), p. 2520. https://doi.org/10.1201/9781315380476.

[28] T.K. Ibrahim, R.K. Abdulrahman, F.H. Khalaf, I.M Kamal, J. Chem. Eng. Process Technol. 8 (2017) 1000337. https://doi.org/10.4172/2157-7048.1000337.

[29] B. Mishra, A. Srivastava, K. Yadav, Heat Mass Transfer 56 (2020) 1153–1169. https://doi.org/10.1007/s00231-019-02759y.

[30] Yount FS. et. al. (2021) ASHRAE Handbook of Fundamentals. SI Edition. ASHRAE, Atlanta, USA. https://www.ashrae.org/technical-resources/ashrae-handbook/description-2021-ashrae-handbook-fundamentals.

FELIPE ZAULI DA SILVA
IZABELLA CARNEIRO BASTOS

Federal University of Alfenas, Institute of Science and Technology, Poços de Caldas, Minas Gerais, Brazil

NAUČNI RAD

STUDIJA O IZMENJIVAČIMA TOPLOTE I INDUSTRIJSKOJ APSORPCIJSKOJ KOLONI ZA SUŠENJE POLIETILENTEREFTALATA

Ova studija predlaže korišćenje bilansa mase i Makejb-Tileove (McCabe-Thiele) metode u apsorpcionoj koloni za uklanjanje vlažnosti vazduha sa etilen glikolom i energetskih bilansa u izmenjivačima toplote za određivanje optimalnih uslova rada fabrike za proizvodnju recikliranih poliesterskih vlakana od pahuljica polietilen tereftalata (PET). Procena ovih mašina je uključivala kombinaciju veličina, kao što su temperatura, brzina protoka, specifična toplota i operativna efikasnost, kako bi se garantovalo ispravno podešavanje fizičko-hemijskih svojstava fluida i procesnih materijala. Utvrđena je efikasnost apsorpcione kolone od 25%. Konstruisan je dijagram koji povezuje vlažnost etilen glikola, tačku rose vazduha za sušenje i efikasnost uklanjanja vlage iz sušare za sušenje PET pahuljica radi definisanja najprikladnije operativne konfiguracija. Na osn ovu grafikona, utvrđeno je da vlažnost etilen glikola za apsorpciju treba da bude niža od 1% (v/v) da bi se garantovala tačka rose < -27 °C pri temparturi vazduha na ulazu u sušaro od 175 °C, što bi konačno promovisalo uklanjanje sa efikasnošću koja je veća od 91% i vlažnošću PET pahuljica < 0,005% (v/v).

Ključne reči: vlažnost, tačka rose, PET pahuljice, polyester, Makejb-Tileov metoda.

CI&CEQ
Chemical Industry & Chemical Engineering Quarterly

Available online at
Association of the Chemical Engineers of Serbia AChE
www.ache.org.rs/CICEQ

Chem. Ind. Chem. Eng. Q. 29 (2) 141–148 (2023) CI&CEQ

NIKOLETA LUGONJA[1]
VESNA MARINKOVIĆ[2]
BILJANA MILIČIĆ[3]
JELENA AVDALOVIĆ[1]
MIROSLAV VRVIĆ[4]
SNEŽANA SPASIĆ[1]

[1]University of Belgrade, Institute of Chemistry, Technology and Metallurgy, National Institute of the Republic of Serbia, Belgrade, Serbia

[2]Institute of Neonatology, Belgrade, Serbia

[3]University of Belgrade, School of Dentistry, Department of Statistics, Belgrade, Serbia

[4]Brem Group, Ltd., Belgrade, Serbia

SCIENTIFIC PAPER

UDC 613.2-053.32:612

EFFECT OF STORAGE PROCESS ON NUTRITIVE PROPERTIES OF PRETERM HUMAN MILK

Article Highlights

- Storage and pasteurization change the lipid and protein properties of preterm human milk
- Lipid content is additionally reduced when milk is pasteurized after freezing
- A fortifier can compensate for deficiencies in preterm milk after storage and pasteurization

Abstract

Freeze storage and pasteurization of human milk are common treatments in milk banks. However, thermal treatment changes milk quality for preterm infants' nutrition. Therefore, this paper aimed to examine preterm human milk's nutritional profile and antioxidant potential after storage, pasteurization, and after supplementation with a fortifier. The effects of storage processes were estimated on the mature preterm milk of 30 breastfeeding women. Total proteins, lipids, and lactose were determined after thermal processing and supplementing mature preterm milk with a fortifier. The ferric-reducing antioxidant potential method and lipid peroxidation inhibition assay determined the antioxidant capacity. Protein concentration decreased after frozen storage and pasteurization ($p<0.05$). Pasteurization further reduced the lipid concentration after freezing. The ferric-reducing antioxidant potential decreased after thermal treatments ($p<0.05$). Supplementing mature milk with a fortifier increased the concentration of proteins, lipids, and lactose. Our findings demonstrated that storage and pasteurization processes affect preterm human milk's basic nutritional composition and antioxidant capacity. To ensure adequate nutrition for preterm infants with preterm human milk, supplementation, especially with high concentrations of proteins and lipids, is necessary after thermal treatments.

Keywords: preterm human milk, pasteurization, freeze storage.

The use of human milk in feeding premature babies is very important and in accordance with the WHO recommendations for using human milk or pasteurized donor milk in feeding early premature babies, which begins in neonatal units [1]. Feeding premature infants with the breast milk of mothers of premature infants are associated with numerous beneficial effects, and it is a key component in the strategy of enteral nutrition for premature babies. In addition to nutritional components, human milk contains biologically important ingredients, such as immunoglobulin, enzymes, immune factors, growth factors, and hormones that can affect growth and development [2,3]. Furthermore, when the mother is separated from the child, she can still secrete milk and store it for later feeding a sick or premature infant. Preterm infants spend the first weeks of their lives in special neonatal units, where human milk nutrition is very important and which supports the storage of milk in milk banks [4,5]. However, storage methods, parameters, and heating processes can affect the quality of human milk's nutritional components [6].

Correspondence: N. Lugonja, University of Belgrade, Institute of Chemistry, Technology and Metallurgy, National Institute of the Republic of Serbia, Njegoseva 12, Belgrade, POB 473.
E-mail: nikoleta.lugonja@ihtm.bg.ac.rs; nikoleta@chem.bg.ac.rs
Paper received: 17 January, 2022
Paper revised: 23 August, 2022
Paper accepted: 30 August, 2022

https://doi.org/10.2298/CICEQ220117021L

The antioxidant concentration is a very important factor for determining the quality of the milk used in the nutrition of premature infants [7]. Premature infants are exposed to oxidative stress after birth, and it is considered that supplementation with enzymatic and non-enzymatic antioxidants can prevent the development of diseases, affect the immune system of the newborn and increase neonatal vitality [8]. In addition to enzymatic systems, many small molecules participate in the prevention of oxidative stress, such as carotene, lipoic acid, enzyme inhibitors, antioxidants, enzyme cofactors, and transition metal chelators [9,10].

Lipid peroxidation is an indicator of oxidative stress in cells and tissues. Peroxides of polyunsaturated fatty acids generate malondialdehyde (MDA) and 4-hydroxyalkenals (HAE) after decomposition, and MDA and HAE levels can be used as lipid peroxidation indicators [11].

Ferric reducing antioxidant potential (FRAP) indicates the levels of antioxidants that act as reductants in redox methods. FRAP depends on the degree of conjugation and the number of hydroxyl groups in the milk [12].

However, preterm infants' intake of macronutrients can be inadequate due to differences in the individual components of human milk. In fact, a premature infant diet consisting exclusively of preterm breast milk over a longer period can be associated with lower growth and progression and the development of nutritional deficit, compared to an infant fed with milk supplemented with fortifier or infant formula for prematurely born children [2,3].

Milk fortifier for human milk supplementation has been introduced to support breastfeeding in premature infants' diets. Fortifiers increase the nutritional value of the milk by adding proteins, vitamins, minerals, and energy, which helps cater to the high nutritional needs of these fast-growing babies [13,14]. Since the composition of human milk can be altered by storage and pasteurization, these are important factors for milk management by milk banks. The nutritional management of high-risk infants using human milk requires individualized, adaptive, or targeted strategies for fortification based on the measurement of milk composition and growth monitoring [15].

This study aimed to examine milk quality from lactating mothers of preterm infants after Holder pasteurization and storage at -20 °C. The nutritional components (protein, fat, and carbohydrate concentrations) and antioxidant capacities related to nutrient activity were determined for that purpose.

EXPERIMENTAL

Study design

Thirty healthy mothers of preterm infants were included in the study conducted at the milk bank of the Institute of Neonatology, Belgrade, Serbia, approved by Institutional Ethics Committee N82401/4 (April 18, 2014). Informed consent was obtained from all participants. Exclusion factors for the study were smoking, and medicaments contraindicated for breastfeeding. The mean age of participants was 27 ± 3 years, and their mean body mass index, mean infant birth weight, and mean gestation week were 23 ± 3.6, 1560 ± 418 g, and 31 ± 2, respectively. Milk samples were collected during different lactation phases: colostrums (4 days postpartum) and transient and mature milk (14 and 21 days after delivery, respectively). The effects of storage and pasteurization were studied in mature milk only. Mature milk samples were examined for each treatment 1: Mature milk, as freshly expressed, homogenized mature milk; 2: Pasteurized milk, mature milk after Holder pasteurization (62.5 °C for 30 min); 3: Milk after seven days storage at -20 °C; 4: Milk after seven days storage at -20 °C, and pasteurized; 5: Milk after 30 days storage at -20 °C; 6: Milk after 30 days storage at -20 °C, and pasteurized. Before measurement, all milk samples were homogenized by an Ultrasonic homogenizer Sonopuls 2000.2 (Bandelin, Berlin, Germany). Fresh milk samples were analyzed immediately after collection, while storage, freezing, and pasteurization effects were examined after thawing and homogenization.

Multicomponent fortifier (FF), produced in Serbia and designed for preterm infants, was used to supplement human milk (5 g FF was added to 100 ml human milk). The fortifier had the following declared basic nutritional information: proteins, 20.8%; carbohydrates, 64.3%; and fat, 4.4%, with ingredients: maltodextrin, prolactal, mineral and vitamin premix, micronutrient premix, refined edible soybean oil, and lecithin [16].

Analyses of nutritional parameters in human milk samples

Human milk samples were analyzed for total protein concentration using the Bradford method [17]. Total fat concentration in milk samples was determined by the Weibull-Berntrop gravimetric method (ISO 8262-1|IDF 124-1:2005) for infant foods [18]. Lactose concentration was determined using Megazyme, Ireland (K-LACGAR), with the assay performed according to the guidelines supplied by the producer [19]. The total carbohydrate concentration was assessed based on the difference between protein,

fat, water, and ash calculated values. The energy content was also calculated, expressed as kJ/100 mL or kcal/100 mL [20]. All nutritional parameters, protein, fat, lactose, and total carbohydrates were expressed as g/100 mL of milk sample. Ferric reducing antioxidant potential (FRAP), as a direct method for measuring the total antioxidant power of biological fluids, was assessed according to Benzie and Strain. The results were expressed as FRAP values (μmol Fe^{2+}/L) [21]. Lipid peroxidation inhibition assay (ILP) was used as an indicator of oxidative stress in milk samples for screening and monitoring lipid peroxidation and non-enzymatic antioxidant activity in milk samples [22]. Malondialdehyde formed by the dissolution of unsaturated fatty acids serves as an index for determining the strength of the peroxidation reaction. It was detected by the thiobarbituric acid assay; the product was determined at 535 nm and expressed in μmol MDA/L.

Statistical analysis

All statistical analyses were performed using Statistical Package for Social Science (SPSS software package, version 25.0; SPSS Inc., Chicago, IL, USA). The results were expressed as mean ± standard deviation (SD). The normality of distributions was tested using the Koglomorov-Smirnov test. If the data were normally distributed, RM ANOVA was used. Non-parametric data were analyzed using the Friedman test. The Pearson correlation coefficient was used to examine the relationship between two observed parameters. All reported p values were two-sided; p values less than 0.05 were considered significant.

RESULTS AND DISCUSSION

The nutritional profile of human milk in different phases of lactation and after storage

The nutritional profiles of human milk in different phases of lactation are presented in Figure 1A. The mean protein concentration in the human milk was significantly different ($p < 0.05$) in the different lactation stages. Preterm colostrums had a higher protein concentration than transient and mature milk, with maximum mean differences occurring in the first few days after birth ($p < 0.05$). There were no statistically significant differences in protein concentration between transient and mature milk. Lipid concentrations of colostrums were statistically different from those of transient and mature human milk samples, while there was no difference between transient and mature milk lipid concentrations ($p > 0.05$). Total carbohydrates in colostrum were significantly lower than in human milk after 14 and 21 days after birth. There was no statistical difference in total carbohydrate concentration between transient and mature milk ($p = 0.130$), while lactose contents differed during the lactation period ($p < 0.05$). Significant differences ($p < 0.05$) in fat and total carbohydrate concentration were observed between colostrum and transient and mature milk examined directly after the milk was expressed at room temperature. However, the Bonferroni pairwise comparison test indicated no significant difference ($p > 0.05$) between transient and mature human milk at room temperature.

Figure 1B shows changes in protein, fat, lactose, and total carbohydrate concentration after mature milk storage at -20 °C for 7 and 30 days and after pasteurization. Protein content slightly decreased and differed after storage at -20 °C for 7 and 30 days and after pasteurization ($p < 0.05$). The mean lipid concentration in milk after frozen storage and pasteurization was lower than in fresh milk ($p < 0.05$). Pasteurization reduced the lipid concentration of mature milk compared to that of fresh mature milk (6%). Freezing at -20 °C for 7 or 30 days did not statistically affect the lipid concentration of mature milk (3-4%; $p > 0.05$). However, storage by freezing for 7 and 30 days and pasteurization immediately before analysis significantly reduced the mean lipid concentration in milk compared to fresh mature milk and mature milk stored by freezing at -20 °C ($p < 0.05$). Freezing changes the physicochemical properties of human milk components. As milk proteins precipitate, casein micelles destabilize, and protein structure changes. Thawing and homogenization do not entirely decompose protein aggregates or lipid globules, especially when manual homogenization is performed. Holder pasteurization increases the effect of freezing on protein and lipid structure, leading to enzyme activity modifications and increased lipolysis [23]. There was no significant change in the lactose concentration of preterm milk after frozen storage and pasteurization. Freezing and pasteurization preserved the mean carbohydrate concentration in the mature milk, and the mean carbohydrate concentration in the stored mature milk did not differ statistically from that of fresh mature milk. There was no significant change in the lactose concentration of mature milk after freezing (compared with lactose levels in fresh mature milk).

The total energy content of preterm milk increased during lactation phases: colostrum 49.9 kcal/100 mL, transient milk 67.5 kcal/100 mL, and mature milk 69.6 kcal/100 mL (Figure 2a). Pasteurization after 7 or 30 days of storage at -20 °C additionally decreased the energy content of human milk ($p < 0.05$), while only storage at -20 °C did not affect the energy content of preterm milk ($p > 0.05$, Figure 2b).

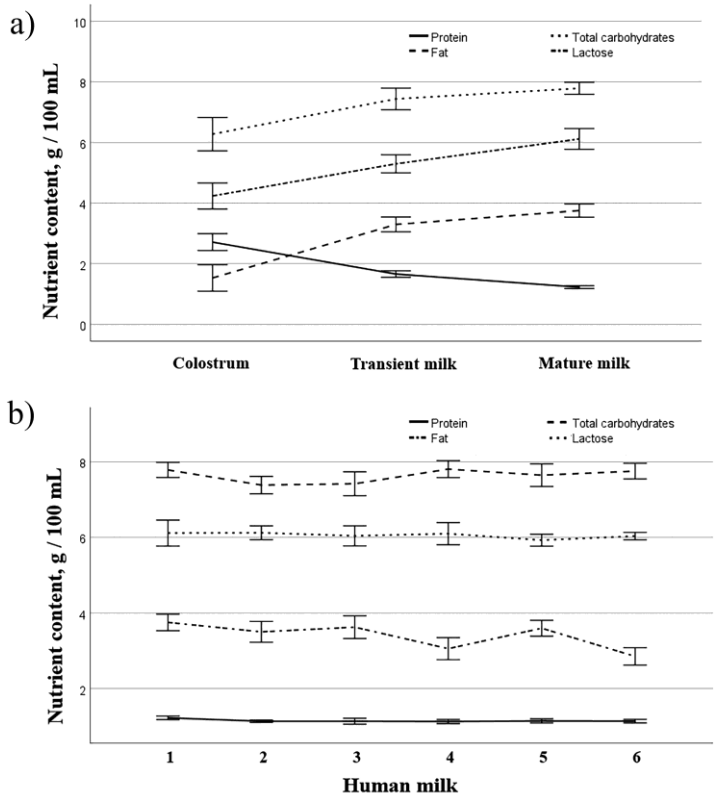

Figure 1. The nutritional profile of human milk in different phases of lactation (A) and after storage and pasteurization treatments (B) A: Colostrum, Transient and Mature milk; B: Human milk samples: 1: Mature milk, 2: Pasteurized milk, 3: Milk after seven days storage at -20 °C, 4: Milk after seven days storage at -20 °C, and pasteurized, 5: Milk after 30 days storage at -20 °C, 6: Milk after 30 days storage at -20 °C, and pasteurized.

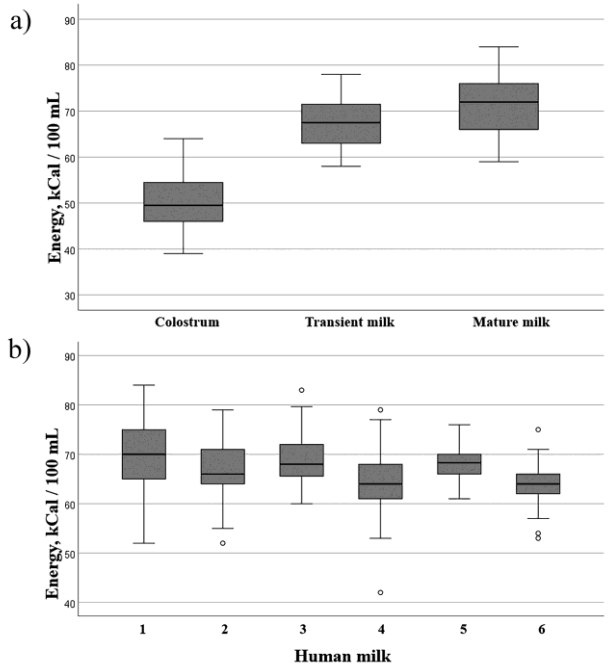

Figure 2. The total energy content of human milk in different phases of lactation (A) and after storage and pasteurization treatments (B) A: Colostrum, Transient and Mature milk; B: Human milk samples: 1: Mature milk, 2: Pasteurized milk, 3: Milk after seven days storage at -20 °C, 4: Milk after seven days storage at -20 °C, and pasteurized, 5: Milk after 30 days storage at -20 °C, 6: Milk after 30 days storage at -20 °C, and pasteurized.

The antioxidant profile of human milk in different phases of lactation and after storage and pasteurization

Figure 3 shows the ILP antioxidant profile of human milk determined by the thiobarbituric acid assay. The concentration of MDA differed slightly according to the lactation phase (p> 0.05), while there was no statistically significant difference due to storage and pasteurization. Fresh mature milk and mature milk after freezing and pasteurization did not show any significant level of lipid peroxidation. The antioxidants in milk likely contributed to the minimal degradation of lipids and proteins. Freezing and pasteurization reduced lipid peroxidation while freezing slightly increased the concentration of MDA but not significantly.

The ferric-reducing antioxidant potential is a biochemical indicator of the antioxidant capacity of human milk in different stages of lactation (Figure 4A). During the lactation period, there was a statistically significant difference (p = 0.029) in FRAP activity between colostrum and transient and mature milk, while there was no difference in FRAP activity between the transient and matured milk (p >0.05). Pasteurization did not affect FRAP compared to raw mature milk. However, the FRAP's antioxidant capacity was significantly reduced after seven days of storage at -20 °C and pasteurization (p <0.05) compared to unprocessed milk. Furthermore, the deleterious effects of pasteurization on FRAP became significant after seven days of storage and pasteurization, while there was no significant difference in FRAP between mature milk and milk after 30 days of storage and pasteurization (Figure 4B).

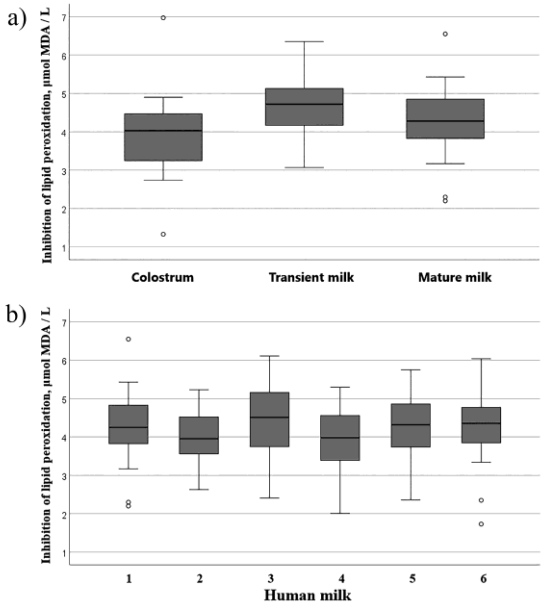

Figure 3. The antioxidant profile of human milk in different phases of lactation (A) and after storage and pasteurization treatments (B) determined by lipid peroxidation inhibition assay (ILP). Human milk samples after storage: 1: Mature milk, 2: Pasteurized milk, 3: Milk after seven days storage at -20 °C, 4: Milk after seven days storage at -20 °C, and pasteurized, 5: Milk after 30 days storage at -20 °C, 6: Milk after 30 days storage at -20 °C, and pasteurized.

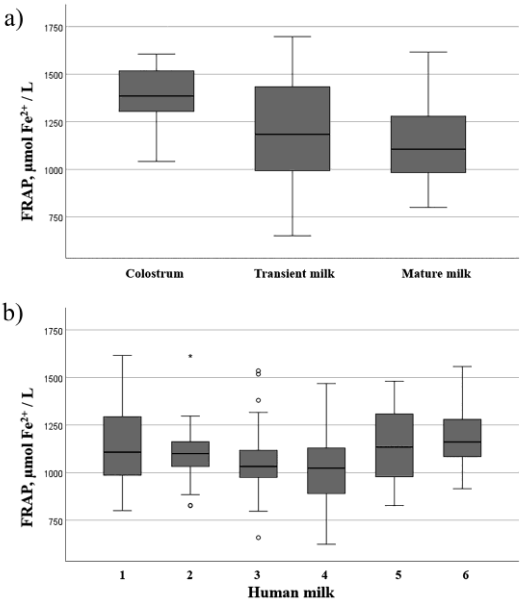

Figure 4. The antioxidant profile of human milk in different phases of lactation (A) and after storage and pasteurization treatments (B) determined by ferric reducing antioxidant potential (FRAP) method. Human milk samples after storage: 1: Mature milk, 2: Pasteurized milk, 3: Milk after seven days storage at -20 °C, 4: Milk after seven days storage at -20 °C, and pasteurized, 5: Milk after 30 days storage at -20 °C, 6: Milk after 30 days storage at -20 °C, and pasteurized.

Table 1 compares the nutritional parameters of the preterm mature milk and the preterm milk supplemented with a fortifier. Supplementing preterm mature milk with the fortifier increased the nutritional value of milk in accordance with the recommendations for preterm infants [15]. Fortifier increased energy by 24% and concentration of protein, lipid, and lactose by 42.0%, 5.2%, and 12.7%, respectively. However, the preterm infant diet in neonatal units was based on the milk stored at -20 °C, which was pasteurized and supplemented with the fortifier immediately before feeding. Storage and pasteurization reduce the antioxidant activity, change the protein and lipid composition and reduce protein and lipid concentrations, so supplementation is necessary. Fortifier increased the nutritional parameters, including the antioxidant activity of non-enzymatic components (by 45-50%; Table 1). In addition, supplementation of preterm milk with fortifier showed an increased FRAP capacity (p< 0.05) and increased concentration of MDA

Table 1. The nutritional profile of preterm mature milk and preterm mature milk supplemented with fortifier.

Nutritional parameters	Preterm mature milk Mean (SD)	Preterm mature milk with fortifier Mean (SD)
Energy, kJ/100 mL	291 (33)	367 (34)
Energy, kcal/100 mL	69.6 (6.7)	87.6 (8.0)
Proteins, g/100 mL	1.23 (0.25)	2.30 (0.13)
Lipids, g/100 mL	3.75 (0.36)	3.95 (0.59)
TC*, g/100 mL	7.78 (0.90)	10.91 (0.53)
Lactose, g/100 mL	6.12 (0.63)	7.51 (0.41)
FRAP, µmol Fe^{2+}/L	1127 (179)	2069.1 (366)
ILP, µmol MDA/L	4.29 (0.89)	10.05 (0.23)

*TC -Total carbohydrates

($p < 0.05$) compared to mature milk.

The composition of human milk during the lactation period varies between mothers and even in individuals during a single day. These multidimensional variations in the composition are due to the mother's adaptation to the infant's needs, the geographical region, and the mode of nutrition [24]. Protein concentration decreased in the preterm milk during lactation stages, and all types of storage affected a slight decrease in the protein concentration of the mature milk. However, there was a difference in the protein concentration in the mature milk samples that underwent different types of storage and pasteurization. Holder's pasteurization deactivated the enzymes and denatured whey proteins, which was in line with previous studies. A previous meta-analysis showed that a high concentration of proteins in the colostrum and early lactation phases resulted from the reduced whey protein concentration, in which lactalbumin, IgA, lactoferrin, and lysosomes were found [25]. The mean lipid concentration of preterm milk increased during lactation, while after freezing, it was lower due to the change of the lipid membrane structure because the fat adheres to the walls of the bottle, as well as due to the inactivation of lipase in the milk, in accordance with the previous studies [26,27].

Preterm milk behaves differently after storage and freezing in relation to full-term milk due to its chemical composition, stability of components, and factors that affect the composition. Therefore, it is subject to different transformations in relation to full-term milk. Preterm infants require an energy-rich diet compared to full-term infants, so human milk is mostly supplemented with fortifiers. The storage process influences the nutritional properties of human milk. This study compared the major nutrient contents in preterm mature milk and preterm mature milk after fortification with a multicomponent fortifier to evaluate the optimization of the nutrient quality of human milk. In addition to nutritional values, the quality of human milk also depends on its antioxidant capacity. The antioxidant capacity of human milk was the greatest in the first weeks of lactation. It was associated with an increased level of oxidative stress that occurs in the mother's body [27,28]. Therefore, total antioxidant capacity measured in the milk samples during lactation and after storage showed the protective role of human milk associated with non-enzymatic antioxidants. Freezing and pasteurizing preterm milk decreased ferric-reducing antioxidant potential and did not affect the lipid peroxidation process. Effects on nutritional and antioxidant properties of milk caused by pasteurization and freezing can be compensated for by supplementing the milk with a fortifier. Fortification of preterm milk should be based on individual milk analysis after thermal treatments.

CONCLUSION

The breast milk given by mothers to preterm infants provides important nutritional components for infant growth and protects against the effects of free radicals, reactive oxygen species, and oxidative stress. Fresh breast milk, especially colostrum, has the required quality and antioxidant properties. When fresh human milk is unavailable, freezing retains human milk's nutritional and antioxidant properties. Freezing is a better storage option than freezing, followed by pasteurization after thawing, especially for preserving the lipid content. Although freezing followed by pasteurization procedures are common in milk banks, they negatively affect the quality of the milk. Therefore, in milk banks, individual milk supplementation with quality fortifiers should provide adequate nutritional components, especially a greater lipid content and a higher concentration of antioxidant components, both of which are required for normal infant development.

ACKNOWLEDGMENTS

The authors would like to thank the Ministry of Education, Science and Technological Development of the Republic of Serbia (Grant No: 451-03-68/2022-14/200026) for financial support.

REFERENCES

[1] World Health Organization. Guidelines on optimal feeding of low birth-weight infants in low- and middle-income countries. Retrieved from https://www.who.int/maternal_child_adolescent/documents/infant_feeding_low_bw/en/ [accessed 21 April 2021].

[2] H.G. Kanmaz, B. Mutlu, F.E. Canpolat, O. Erdeve, S.S. Oguz, N. Uras, U. Dilmen, J. Hum. Lactation 29 (2013) 400–405. https://doi.org/10.1177/0890334412459.

[3] B. Lonnerdal, Nutrition 16 (2000) 509–511. https://doi.org/10.1016/S0899-9007(00)00363-4.

[4] M. A. Underwood, Pediatr. Clin. North Am. 60(1) (2013) 189–207. https://doi.org/10.1016/j.pcl.2012.09.008.

[5] J. Kim, S. Unger, Paediatr. Child Health 15(9) (2010) 595–598. https://doi.org/10.1093/pch/15.9.595.

[6] C. Pound, S. Unger, B. Blair, Paediatr. Child Health 25(8) (2020) 549–550. https://doi.org/10.1093/pch/pxaa118.

[7] C. Hanson, E. Lyden, J. Furtado, M. Van Ormer, A. Anderson-Berry, Nutrients 8 (2016) 681. https://doi.org/10.3390/nu8110681.

[8] Y. Ozsurekci, K. Aykac, Oxid. Med. Cell. Longevity (2016) ID 2768365. https://doi.org/10.1155/2016/2768365.

[9] C. Matos, M. Ribeiro, A. Guerra, J. Appl. Biomed. 13 (2015) 169–180. https://doi.org/10.1016/j.jab.2015.04.003.

[10] D. Huang, B. Ou, RL Prior, J. Agric. Food Chem. 23 (2005) 1841–1856. https://doi.org/10.1021/jf030723c.

[11] I.F. Benzie, J.J. Strain, Methods Enzymol. 299 (1999) 15–27. https://doi.org/10.1016/S0076-6879(99)99005-5.

[12] K. Jomova, M. Valko, Toxicology 283 (2011) 65–87. https://doi.org/10.1016/j.tox.2011.03.001.

[13] C. Agostini, G. Buonocore, V.P. Carnielli, M. De Curtis, D. Darmaun, T. Decsi, M. Domellöf, N.D. Embleton, et al., J. Pediatr. Gastroenterol. Nutr. 50 (2010) 85–91. https://doi.org/10.1097/MPG.0b013e3181adaee0.

[14] A. Choi, G. Fusch, N. Rohow, C. Fusch, Plos One 11(2) (2016) e0148941. https://doi.org/10.1371/journal.pone.0148941.

[15] S. Arslanoglu, G.E. Moro, E.E. Ziegler, J. Perinat. Med. 38(3) (2010) 233–238. https://doi.org/10.1515/jpm.2010.073.

[16] N. Lugonja, D. Stankovic, B. Milicic, S. Spasic, V. Marinkovic, M.M. Vrvic, Food Chem. 240 (2018) 567–572. https://doi.org/10.1016/j.foodchem.2017.07.164.

[17] N. Kamizakea, M. Gonçalves, T.B.V. Cássia, C. Zaia, D. Zaia, J. Food. Compost. Anal. 16 (2003) 507–516. https://doi.org/10.1016/S0889-1575(03)00004-8.

[18] EN ISO 8262-1|IDF 124-1: Milk products and milk-based foods – Determination of fat content by the Weibull-Berntrop gravimetric method (Reference method) – Part 1: Infant foods (2005). https://www.iso.org/standard/42070.html.

[19] H.O. Beutler, in Methods of Enzymatic Analysis, Bergmeyer, H. U. Ed., VCH Publishers (UK.) Ltd, Cambridge, UK, (1988), p. 104. ISBN 978-0-12-091302-2.

[20] FAO, in Food Energy - Methods of Analysis and Conversion Factors; Food and Agriculture Organization of the United Nations: Rome, Italy, (2003), p.77. ISBN 92-5-105014-7.

[21] I.F. Benzie, J.J. Strain, Anal. Biochem. 239 (1996) 70–76. https://doi.org/10.1006/abio.1996.0292.

[22] R.D. Janero, Free Rad. Biol. Med. 9 (1990) 515–540. https://doi.org/10.1016/0891-5849(90)90131-2.

[23] N. García-Lara, D. Vieco, D.J. Cruz-Bértolo, D. Lora, N. Ureta-Velasco, C. Pallás-Alonso, J. Pediatr. Gastroenterol. Nutr. 57(3) (2013) 377–382. https://doi.org/10.1097/MPG.0b013e31829d4f82.

[24] O. Ballard, A.L. Morrow, Pediatr. Clin. North Am. 60 (2013) 49–74. https://doi.org/10.1016/j.pcl.2012.10.002.

[25] C.A. Butts, D.I. Hedderley, T.D. Herath, G. Paturi, S. Glyn-Jones, F. Wiens, B. Stahl, P. Gopal, Nutrients 10(9) (2018) 1231. https://doi.org/10.3390/nu10091231.

[26] L. Lamport, C. Hartman, C. Codipilly, B. Weinberger, R. Schanler, J. Parenter. Enteral Nutr. 43 (2018) 809–814. https://doi.org/10.1002/jpen.1470.

[27] A.A. Vieira, F.V. Soares, H.P. Pimenta, D. Abranches , E. Moreira, Early Hum. Dev. 87(8) (2011) 577–580. https://doi.org/10.1016/j.earlhumdev.2011.04.016.

[28] V. Marinković, M. Ranković-Janevski, S. Spasić, A. Nikolić-Kokić, N. Lugonja, D. Djurović, S. Miletić, M. Vrvić, I. Spasojevic, J. Pediatr. Gastroenterol. Nutr. 62 (2016) 901–906. https://doi.org/10.1097/MPG.0000000000001090.

NIKOLETA LUGONJA[1]
VESNA MARINKOVIĆ[2]
BILJANA MILIČIĆ[3]
JELENA AVDALOVIĆ[1]
MIROSLAV VRVIĆ[4]
SNEŽANA SPASIĆ[1]

[1]Univerzitet u Beogradu, Institut za hemiju, tehnologiju i metalurgiju, Institut od nacionalnog značaja za Republiku Srbiju, Beograd, Srbija

[2] Institut za neonatologiju, Beograd, Srbija

[3] Univerzitet u Beogradu, Stomatološki fakultet, Odsek za statistiku, Beograd, Srbija

[4]Brem Group, d.o.o., Belgrade, Serbia

NAUČNI RAD

UTICAJ PROCESA SKLADIŠTENJA NA NUTRITIVNA SVOJSTVA MLEKA MAJKI PREVREMENO ROĐENE DECE

Zamrzavanje i pasterizacija humanog mleka su uobičajeni tretmani u bankama mleka. Termička obrada menja kvalitet mleka za ishranu prevremeno rođene dece, stoga je značaj ovog rada da istraži nutritivni sastav i antioksidativni potencijal mleka majki prevremeno rođene dece nakon skladištenja i pasterizacije i nakon suplementacije obogaćivačem majčinog mleka. Efekti procesa skladištenja su ispitivani na zrelom mleku 30 žena koje su se prevremeno porodile. Nakon termičke obrade i suplementacije majčinog mleka obogaćivačem ispitivan je sadržaj ukupnih proteina, lipida i laktoze. Antioksidativni kapacitet je određen metodom baziranom na reakciji antioksidanasa sa Fe (III)-kompleksom i metodom inhibicije lipidne peroksidacije. Nakon skladištenja zamrzavanjem i pasterizacije opada koncentracija proteina ($p< 0.05$). Pasterizacija nakon skladištenja zamrzavanjem dodatno smanjuje koncentraciju lipida. Antioksidativni potencijal, određen metodom baziranom na reakciji antioksidanasa sa Fe (III)-kompleksom, smanjuje se nakon termičke obrade ($p< 0.05$). Suplementacija zrelog mleka obogaćivačem povećava koncentraciju proteina, lipida i laktoze. Naši rezultati su pokazali da procesi skladištenja i pasterizacije utiču na osnovni nutritivni sastav i antioksidativni kapacitet mleka majki prevremeno rođene dece. Da bi se obezbedila adekvatna ishrana prevremeno rođene dece, neophodna je suplementacija mleka, posebno visokim koncentracijama proteina i lipida, nakon termičke obrade.

Ključne reči: mleko majki prevremeno rođene dece, pasterizacija, skladištenje zamrzavanjem.

CI&CEQ
Chemical Industry & Chemical Engineering Quarterly

Available online at
Association of the Chemical Engineers of Serbia *AChE*
www.ache.org.rs/CICEQ

Chem. Ind. Chem. Eng. Q. 29 (2) 149–160 (2023) CI&CEQ

MAJA MILIJAŠ[1]
DRAGOLJUB CVETKOVIĆ[2]
ALEKSANDAR SAVIĆ[1]
ANA VELEMIR[1]
LJILJANA TOPALIĆ-TRIVUNOVIĆ[1]
SAŠA PAPUGA[1]

[1]Faculty of Technology, University of Banja Luka, Banja Luka, Republic of Srpska

[2]Faculty of Technology, University of Novi Sad, Novi Sad, Serbia

SCIENTIFIC PAPER

UDC 638.167:544.:663

EFFECTS OF ADDING DIFFERENT QUANTITIES OF YEAST AND CHOKEBERRY JUICE ON FERMENTATION OF MEAD

Article Highlights

- Adding chokeberry juice improved the antioxidant properties of the final product
- Adding chokeberry juice positively affected the course of the fermentation of mead
- A statistically significant difference between the samples containing different quantities of yeast
- The model foresaw a fairly good overlap of curves with the experimentally obtained data
- The addition of aronia juice affects the antimicrobial activity of meads

Abstract

Honey is a product of high nutritional value, used as a raw material for obtaining mead. However, adding fruit juices, including chokeberry juice, can improve mead quality. This paper aims to assess the effects that adding different quantities of chokeberry juice, with the variation of 3 amounts of inoculated yeast, has on the fermentation and physicochemical, antioxidant, and antimicrobial properties of mead. The parameters analyzed are the dry matter content, pH value, and content of volatile acids, ethanol and methanol, total phenols and flavonoids, FRAP, DPPH, and ABTS tests, and antimicrobial properties. The results obtained in this paper show that adding chokeberry juice improves the antioxidant properties of the final product and positively affects the course of mead fermentation, i.e., it has led to an increase in the maximum concentration of ethanol. Regarding the chemical composition of mead, there is no significant difference, except in the obtained ethanol content, which is the highest in samples with 10% of added chokeberry juice. Furthermore, the control sample showed the best antimicrobial activity, while the sample with 5% added chokeberry juice showed the weakest effect. Finally, the strongest effect was seen in the sample with 20% of added chokeberry juice.

Keywords: antimicrobial activity, antioxidant activity, aronia, fermentation rate, kinetic model, mead.

Honeydew honey comes mainly from the excretions of plant-sucking insects (Hemiptera) on the living parts of plants or their secretions [1]. A particular characteristic of this type of honey is its high antioxidant [2] and antimicrobial activity [3].

Mead is a traditional alcoholic beverage that contains between 8 and 18 vol.% produced by the alcoholic fermentation of diluted honey under the influence of yeast cells [4]. Mead positively affects human metabolism, especially digestion, and reduces the risk of chronic diseases [5].

Numerous studies focus not only on traditional mead but also on mead with the addition of fruit juices, fruits, herbs, and spices [6]. Melomel is a special type of mead. It is obtained by adding fruits or juices to a honey solution [7]. These additives accelerate and ameliorate the fermentation process, increase alcohol yield, and improve the characteristics of the final product [8,9]. Due to the high nutritional value of berries and their antioxidant properties and specific taste, chokeberry (*Chokeberry melanocarpa*) is a fruit raw

Correspondence: M. Milijaš, Faculty of Technology, University of Banja Luka, Bulevar Vojvode Stepe Stepanovića 73, 78000 Banja Luka, Republic of Srpska.
E-mail: maja.milijas@tf.unibl.org
Paper received: 25 March, 2022
Paper revised: 8 July, 2022
Paper accepted: 30 August, 2022

https://doi.org/10.2298/CICEQ220325022M

material used in the food industry more and more often [10]. Adding chokeberry to a honey solution might affect the antioxidant and antimicrobial properties of mead because its berries are a rich source of polyphenolic compounds and other bioactive components (proanthocyanidins, anthocyanins, flavonoids, phenolic acids, etc.), and the antimicrobial effect of chokeberry is demonstrated on a wide spectrum of microorganisms [11]. Besides, these components also have anti-inflammatory and antiviral activity [12].

Several mathematical models describing the process kinetics were used to achieve better control of the fermentation process. Generally, kinetic models of alcoholic fermentation provide a mathematical description of the processing speed under different conditions of temperature, pH value, aeration, mixing, parameters correction, regulation of the level of foam, etc. It enables the reduction of production costs and increases the quality of the final product. The Gompertz mathematical model can be applied to predict different substrates' fermentation kinetics [13].

This paper aims to examine the effect of adding different quantities of chokeberry juice in fermentation solutions, with a variation of 3 quantities of inoculated yeast, on the fermentation and physiochemical, antioxidant, and antimicrobial properties of mead.

EXPERIMENTAL

For the needs of this experiment, honeydew honey produced in 2018 in the Banjaluka region, Republic of Srpska, was used, as well as cold-pressed chokeberry juice produced by "Natural Agro" from Prnjavor, Republic of Srpska. In this experiment, the sample of the honeydew honey was kept in glass containers at 4 °C, and the chokeberry juice in plastic bottles at -18 °C.

Honeydew honey must preparation

Honeydew honey was stirred with water in a ratio of 1:3 (honeydew honey/water). The resultant wort was pasteurized at 65 °C for 10 min, cooled, and poured into fermentation flasks. Aronia juice was also pasteurized at 65 °C for 10 min, cooled, and poured into fermentation flasks in amounts required for this study. Four samples were prepared: control wort without added Aronia juice (sample 1) and three worts with added Aronia juice in the amount of 5% (sample 2), 10% (sample 3), and 20% (sample 4) of fermentation wort volume. Into all samples, yeast energizer (VitaFerm Ultra F3, Erbslöh, Geisenhein, Germany) was added in an amount of 0.267 g/L. Commercial yeast Fermol Lager (AEB Group, Italy), a selected dry yeast strain of *Saccharomyces pastorianus*, was rehydrated in distilled water at 35 °C–40 °C for 30 min and added in the amount of 0.15 (label A), 0.30 (label B) and 0.6 (label C) g/L of wort. The process of alcoholic fermentation was conducted at 25 °C for 21 days. All fermentations were carried out in triplicate using a system consisting of 250 mL flasks containing 190 mL of wort mixture and fitted with an airlock to release CO_2 produced during fermentation. The dynamics of the fermentation processes were controlled based on weighing the flasks in time on a scale every 24 h throughout the alcoholic fermentation [14].

General oenological parameters

At the end of fermentations, the oenological parameters of mead: pH value, volatile acidity, and dry matter content, were measured [15].

The content of ethanol and methanol in mead was determined by the GC-FID method at Clarus 680 Perkin Elmer instrument with the FID detector, Elite-Wax L 60 m column, ID 0.32, DF 0.5, absolute ethanol and methanol standards, with acetonitrile as the internal standard. The injector and detector temperature of 250 °C, a sample volume of 0.5 µL, and a temperature regime of 45 °C (2 min), 45 °C/min to 245 °C (1 min). The total duration was 7.44 min, and the flow was 3 mL/min [16].

Determination of antioxidant activity

The total phenolic content in meads was measured spectrophotometrically according to the Folin-Ciocalteu method [17]. The results were expressed as total phenolic equivalent to gallic acid (mg GAE/mL).

The total flavonoid content in meads was measured using the method of Ordoñez *et al.* [18]. The results were expressed as flavonoid content to gallic acid (mg GAE/mL). 2,2-Diphenyl-1-picrylhidrazyl (DPPH) radical scavenging assay was determined by the method of Brand-Williams *et al.* [19]. The results were expressed in µgTrolox equivalent/mL-(µg TE/mL). 2,2′-Azino-bis-(3 - ethylbenzothiazoline - 6- sulphonic acid) (ABTS) radical scavenging assay was performed [20]. The results were expressed in mg TE/mL. Finally, ferric reducing/antioxidant power (FRAP) was performed as described by Banzie and Strain [21]. The results were expressed in mmol Fe^{2+}/mL.

Antibacterial activity

The following bacterial cultures: *Escherichia coli* ATCC 25922, *Pseudomonas aeruginosa* ATCC 10145, *Staphylococcus aureus* ATCC 25923, and *Bacillus cereus* ATCC 7004 were used. The cultures were grown in a Nutrient broth (Liofilchem, Italy) and incubated for 24 h at 37 °C, after which they were inoculated and grown on Nutrient agar (Liofilchem,Italy)

for the next 24 h at 37 °C. Agar wells and agar dilution methods for determining the minimum inhibitory concentration (MIC) and the minimum bactericidal concentration (MBC) [22,23]. The concentration of the mead in the medium was 40%, 30%, and 20% (v/v). The highest dilution of the tested mead to inhibit the visible growth of bacteria was considered the MIC value. From the plates showing no visible sign of growth in MIC determination, test microorganisms were inoculated onto sterile Mueller Hinton agar (Liofilchem, Italy) plates. The plates were then incubated at 37 °C for 24 h. The lowest concentration that did not show test organism growth was considered the MBC. The antimicrobial activity of meads was performed in eight replicates for the agar wells method and two replicates for the MIC/MBC method. The results were expressed as the mean ± SD for the agar wells method and in % (v/v) of mead. The antibiotic susceptibility discs Ampicillin (10 μg), Gentamicin (10 μg), Erythromycin (15 μg), and Ciprofloxacin (5 μg) were used as a positive control. The manufacturer of antibiotic discs is Mast Group, UK.

Statistical analysis

All tests were performed in two or three replicates (except the agar wells method), and the results were expressed as means ± standard deviation (except for MIC/MBC values). Analysis of variance (ANOVA) was applied to test significant differences between mead samples. Tukey's test was used to identify differences between mean values obtained in meads ($p \leq 0.05$). Characteristic kinetic parameters of alcoholic fermentation were obtained by fitting the measured values of ethanol production into a modified Gompertz equation, performing nonlinear regression analysis. The statistical analysis of the developed mathematical relations was done by applying linear regression analysis and Fisher's statistical test.

RESULTS AND DISCUSSION

The fermentation process kinetics was monitored based on measuring the changes in the mass of the bottles in certain time intervals, and it was expressed as a cumulative mass (g) of the ethanol produced in a specific time interval. The production of CO_2 during alcoholic fermentation represents an indirect measure of the consumption of fermentable carbohydrates [14]. Figures 1, 2, and 3 show the kinetics of ethanol production in the fermentation process for 12 samples. A great similarity can be noticed between the curves representing the fitted curves determined by a model and the curves determined experimentally. The correlation coefficient ranges from 0.984 to 0.999. Furthermore, an exponential increase in the number of yeast cells can be seen in all the samples.

Table 1. Kinetic parameters of the developed mathematical models and corresponding experimental data.

Sample	P_m, g,cumulative mass	$r_{p,m}$, g·h^{-1}	t_1, h	R^2
1A	152.39	0.24	192.44	0.990
	74.31*	0.02*	-	
1B	96.48	0.32	51.66	0.998
	92.40*	0.06*	-	
1C	93.54	0.26	35.34	0.997
	86.33*	0.06*	-	
2A	111.57	0.37	46.18	0.987
	113.47*	0.09*	-	
2B	98.77	0.35	43.95	0.983
	102.44*	0.05*	-	
2C	99.66	0.42	37.52	0.985
	105.12*	0.08*	-	
3A	100.54	0.42	43.20	0.996
	102.41*	0.08*	-	
3B	101.36	0.43	37.09	0.997
	103.29*	0.13*	-	
3C	101.76	0.42	25.22	0.995
	104.45*	0.10*	-	
4A	98.58	0.35	45.79	0.990
	101.39*	0.10*	-	
4B	99.75	0.37	40.31	0.991
	102.70*	0.12*	-	
4C	94.80	0.36	33.43	0.989
	98.56*	0.14*	.	

* - measured values.

Table 1 shows in a parallel manner the values of kinetics parameters of the developed equations and corresponding values calculated based on the experimental data. For all the samples, the predicted values correspond to the measured ones, except for sample 1A. The reason for this deviation could be the lowest amount of yeast added compared to all three control samples. In most samples, the maximum ethanol production rate (R_{pm}) calculated from the experimental data was higher than the predicted values.

The lowest P_m-value (74.31) was obtained from sample 1A, while the highest value (113.47) was obtained from sample 2A. The values of r_{pm} ranged from 0.02. Based on the results shown in Table 1 and Figures 1, 2, and 3, there is a statistically significant difference between the samples containing the same amount of added chokeberry juice, *i.e.*, between

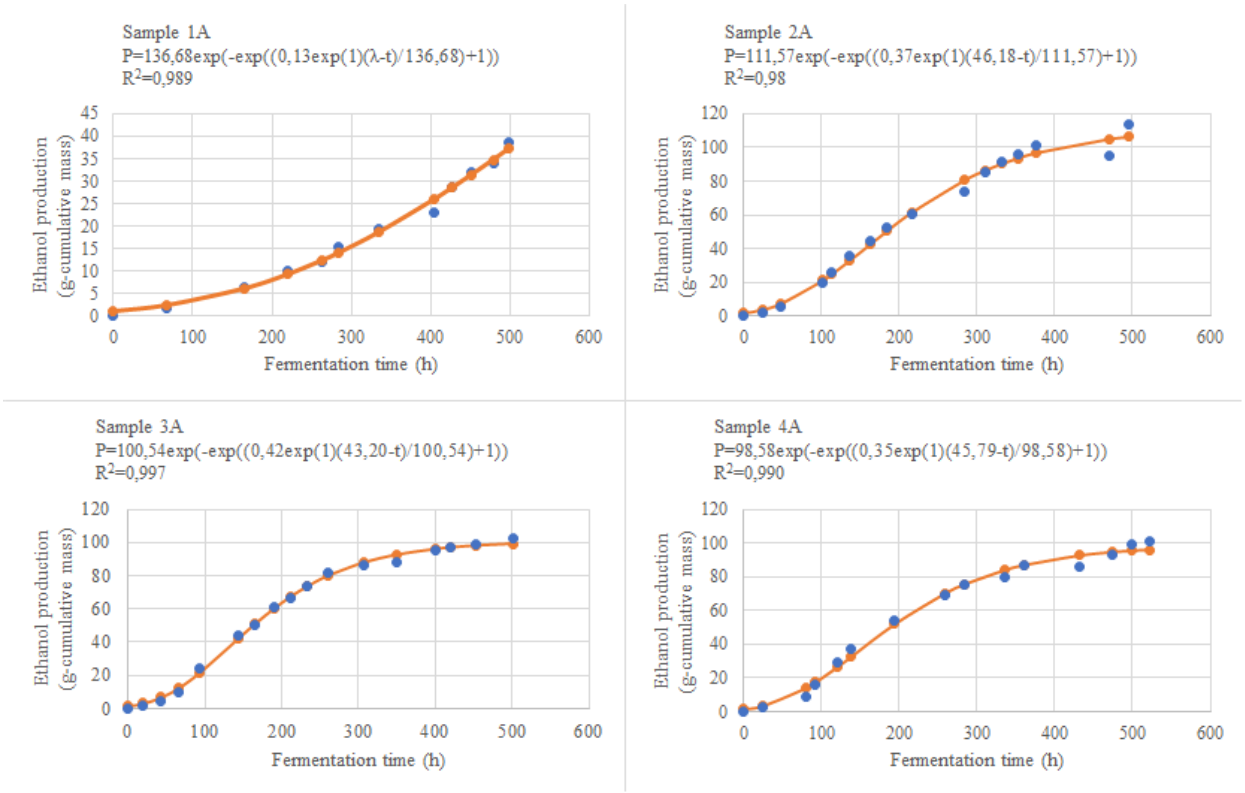

Figure 1. Ethanol production kinetic and results from fitting the experimental data into a modified Gompertz equation (solid line - fitted curve, symbol - experimental data) for samples 1A, 2A, 3A and 4A.

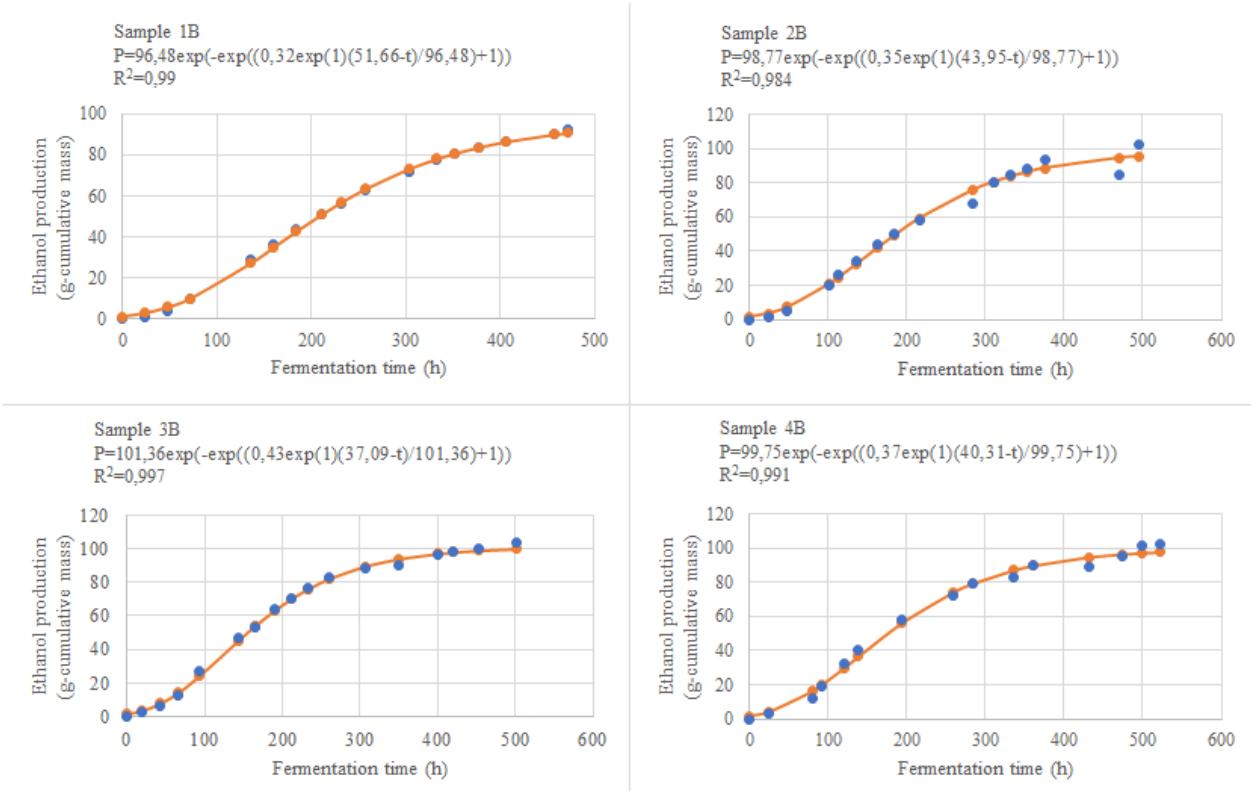

Figure 2. Ethanol production kinetic and results from fitting the experimental data into a modified Gompertz equation (solid line - fitted curve, symbol - experimental data) for samples 1B, 2B, 3B, and 4B

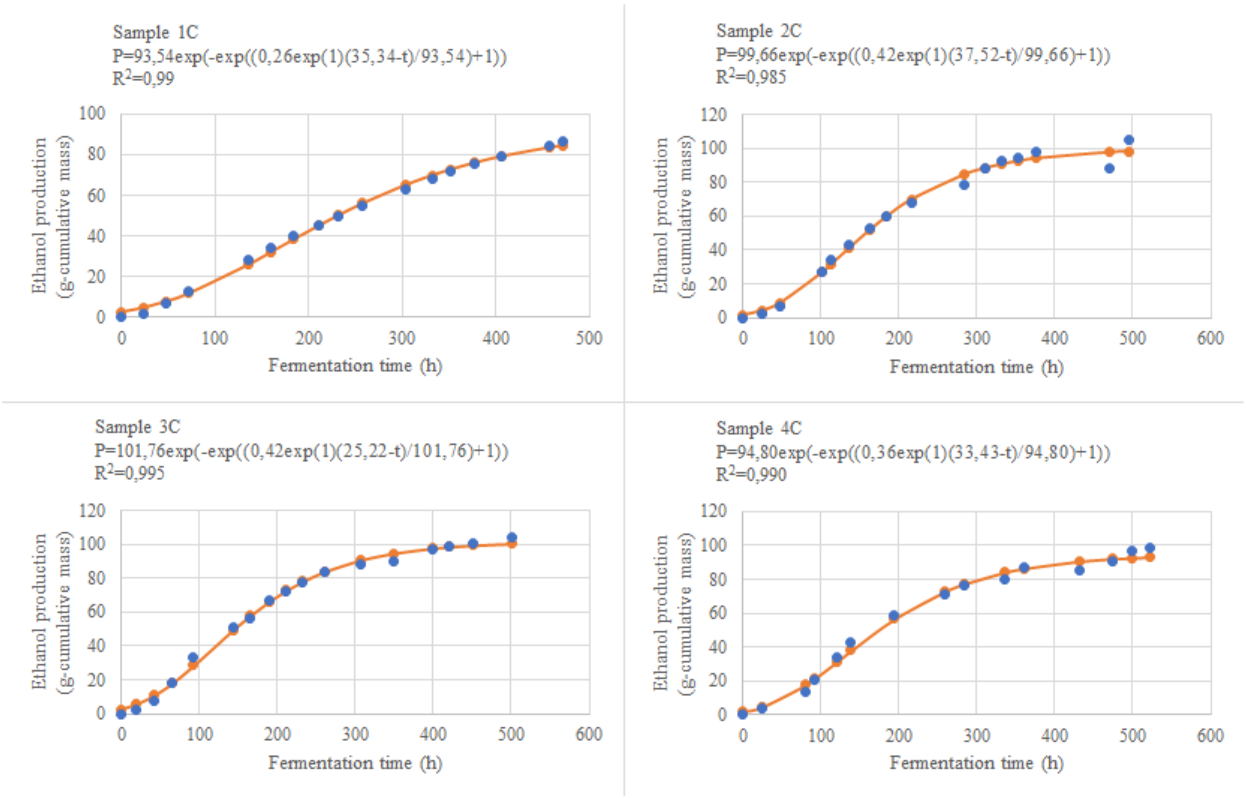

Figure 3. Ethanol production kinetic and results from fitting the experimental data into a modified Gompertz equation (solid line - fitted curve, symbol - experimental data) for samples 1C, 2C, 3C and 4C

different quantities of yeast added to start the fermentation process. for sample 1A, to 0.14 for sample 4C. In addition to these values, a significant difference was noticed in the duration of the lag phase, which was the shortest in sample 3C (25.22 h), while the longest lag phase was measured in sample 1A (192.44 h).

Table 2 shows the results of the dry matter content and pH in stock solutions for fermentation. It can be noticed that the addition of chokeberry juice led to a mild decrease in the dry matter content, from 18.50% in the control sample to 18.00% in the sample with the addition of 20% of chokeberry juice. The fermentation process led to a reduction of the dry matter content, which is shown in Table 3, and once the fermentation was over, it ranged from 7.93% for sample 1B to 9.48% for sample 2B. The statistical analysis showed that in one part of the mead samples, there was no statistically significant difference in the results of the dry matter content with the same quantity of added chokeberry juice. In contrast, for samples 2 and 4, a significant statistical difference was noticed. Based on the obtained results, it can be presumed that mead contains a higher amount of residual sugar that does not participate in the fermentation process [24], *i.e.*, that such dry matter content can be explained by the presence of sugar in the form of disaccharides and oligosaccharides, which cannot be fermented by yeast [25].

Table 2. The results of physicochemical parameters of honey must (pH value and dry matter content).

Parameter/sample	1	2	3	4
Dry matter content (%)	18,50 ± 0,00	18,50 ± 0,00	18,30 ± 0,00	18,00 ± 0,00
pH	3,99 ± 0,00	3,95 ± 0,01	3,91 ± 0,01	3,85 ± 0,01

The pH value of the must prepared by mixing honeydew honey and water was 3.99. By adding chokeberry juice, the pH in all musts decreased. By adding 5%, 10%, and 20% of juice, the pH dropped to 3.95, 3.91, and 3.85, respectively. The decrease in pH could be due to the naturally high acidity of chokeberry juice. Once the fermentation process was over, pH dropped in all samples. The lowest pH of 3.54 was in sample 1B, while the highest value of 3.80 was in sample 4C. Sroka and Satora [26] obtained similar results of pH, where the mead pH was 3.40, while Martínez *et al.* [27] stated that pH ranged from 3.66 to 4.00. In most of the mead samples with the same juice content, there was no significant statistical difference in

pH, indicating that the quantity of yeast does not significantly impact the change of pH in the fermentation process. The trend of changes in pH depends on the acidity derived from fruit juice. In contrast, the decrease in pH during fermentation can be a consequence of the metabolic activity of yeast [28]. A pH decrease after fermentation can also be explained by the weak buffering capacity of honey [29] and by the production of acids by yeast during fermentation [30]. Low pH in fermentation inhibits microbial growth, leading to product spoilage. At the same time, it creates a suitable environment for the growth of microorganisms necessary for the fermentation process [28].

Table 3 shows the results of the physicochemical analysis of mead. Volatile acids in honey are mostly a result of the production of acetic acid during yeast fermentation. This acid, in alcoholic fermentation, is produced by yeast *S. Cerevisiae* in the amount of 0.3 g/L to 0.8 g/L, even though the formation of this compound is undesirable [31]. The content of volatile acids is affected by the type of yeast used, fermentation conditions, and the chemical composition of raw material [32,33]. Based on the results shown in Table 3, it can be noticed that the content of volatile acids in mead significantly differs with the same amount of added chokeberry juice and different concentration of added yeast. Bely *et al.* [34] state that during the fermentation of solutions with higher amounts of sugar, the amount of yeast added did not significantly affect the content of volatile acids in the final product, which is different from the results obtained in this paper. The prolonged fermentation leads to an increase in the content of volatile acids and a decrease in pH [35]. The content of volatile acids in the mead ranged from 0.14 g/L in sample 4A to 0.33 g/L in sample 1C. The content of volatile acids should not be higher than 1.4 g/L [32], following the results obtained in this paper. The production of a larger amount of acetic and succinic acid can slow or even stop fermentation [8].

The ethanol content in the mead ranged from 8.32 vol.% in sample 4B to 11.98 vol.% in sample 3A.

Table 3. The results of physicochemical parameters od meads (pH value, dry matter content, volatile acidity, methanol content and ethanol content).

Sample	Dry matter content (%)	pH	Volatile acidity (g/L)	Methanol content (vol. %)	Ethanol content (vol. %)
1A	$8,10^{a}\pm0,09$	$3,61^{b}\pm0,02$	$0,27^{fg}\pm0,05$	$0,001^{a}\pm0,000$	$8,65^{a}\pm0,35$
1B	$7,93^{a}\pm0,31$	$3,54^{a}\pm0,01$	$0,29^{gh}\pm0,03$	$0,002^{ab}\pm0,001$	$9,19^{a}\pm0,28$
1C	$8,15^{a}\pm0,25$	$3,56^{a}\pm0,02$	$0,33^{h}\pm0,04$	$0,002^{a}\pm0,001$	$9,13^{a}\pm0,53$
2A	$9,33^{de}\pm0,05$	$3,69^{cd}\pm0,01$	$0,21^{cde}\pm0,03$	$0,002^{ab}\pm0,000$	$11,39^{bc}\pm0,14$
2B	$9,48^{e}\pm0,36$	$3,72^{d}\pm0,02$	$0,24^{ef}\pm0,00$	$0,001^{a}\pm0,001$	$11,15^{bc}\pm0,34$
2C	$9,02^{cd}\pm0,34$	$3,72^{d}\pm0,00$	$0,23^{def}\pm0,02$	$0,000^{a}\pm0,000$	$10,79^{b}\pm0,40$
3A	$8,58^{bc}\pm0,08$	$3,66^{c}\pm0,01$	$0,19^{bcd}\pm0,03$	$0,001^{a}\pm0,000$	$11,98^{c}\pm0,19$
3B	$8,62^{bc}\pm0,10$	$3,69^{cd}\pm0,01$	$0,18^{abc}\pm0,00$	$0,001^{a}\pm0,000$	$11,72^{bc}\pm0,31$
3C	$8,62^{bc}\pm0,12$	$3,73^{d}\pm0,01$	$0,21^{cde}\pm0,00$	$0,001^{a}\pm0,000$	$11,66^{bc}\pm0,16$
4A	$8,70^{abc}\pm0,28$	$3,77^{e}\pm0,03$	$0,14^{a}\pm0,02$	$0,004^{bc}\pm0,001$	$8,61^{a}\pm0,15$
4B	$8,60^{b}\pm0,00$	$3,78^{e}\pm0,00$	$0,15^{ab}\pm0,03$	$0,003^{ab}\pm0,002$	$8,33^{a}\pm0,39$
4C	$8,75^{bc}\pm0,08$	$3,80^{e}\pm0,00$	$0,16^{ab}\pm0,03$	$0,006^{c}\pm0,002$	$9,03^{a}\pm0,39$

Higher ethanol content was measured in the samples in which 5% and 10% of chokeberry juice had been added. The ethanol content was lower in the samples without and with 20% added chokeberry juice. Akalin *et al.* [33] presented similar results, recording the ethanol content from 9.20 vol.% to 11.38 vol.%, while Pereira *et al.* [36] recorded from 10.03 vol.% to 10.33 vol.%. The ethanol content in mead depends on the yeast used in the fermentation process and the additives used in its production [37]. Lower ethanol content and a shorter fermentation period can be explained by the poorer response of yeast cells to stress conditions in the fermentation solution [38]. Similar results can be found in the study of Martínez *et al.* [27]. Akalin *et al.* [33] stated that the alcohol content in mead mainly depended on the quantity of honey in the stock solution and its dilution level. Based on the results shown in Table 3, it can be seen that in most samples, there are no statistically important differences in the ethanol content for the mead in which the same amount of juice was added, *i.e.*, in the samples with different concentrations of added yeast. Roni *et al.* [39] stated that adding a higher yeast concentration in the bioethanol production resulted in a higher ethanol concentration, which differed from the results of the present work. Ethanol produced in the fermentation process helps preserve, extract, and absorb phenolic compounds naturally present in honey [40].

The methanol content in mead was very low. In sample 2C, the methanol content was lower than 0.001 vol.%, while in sample 4C, the measured content was 0.006 vol.%. The methanol content in the mead

derives from the added chokeberry juice because the content and esterification degree of pectic matters in fruit can affect the methanol concentration in wines, thus also in mead [41]. Based on the obtained results, it can be seen that there is no significant difference between individual samples and that the addition of chokeberry juice did not significantly affect the increase of methanol in mead.

Table 4 shows the results of the analysis of antioxidant properties, *i.e.*, the total phenolic and flavonoid content and the FRAP, DPPH, and ABTS tests. The total phenolic content in the analyzed samples ranged from 297.61 mg GAE/mL in sample 1C to 715.62 mg GAE/mL in sample 4B. Based on the results shown in Table 4, it can be seen that the increase of the added chokeberry juice led to an increase in the total phenolic content. A similar can be noticed with the flavonoid content, where the flavonoid content was lowest in the control samples (1A, 1B, 1C), in which chokeberry juice had not been added. In contrast, the highest flavonoid content was measured in those samples in which 20% of chokeberry juice had been added (4A, 4B, 4C). The statistical analysis shows that the total phenolic content was different in the same amount of added juice, *i.e.*, there were differences in the phenolic content when adding different yeast concentrations. Unlike the total phenolic content, the flavonoid content in the samples with the same amount of juice and different yeast concentration was not statistically different in most samples, except for the samples with 5% chokeberry juice added. Also, based on the results, it can be concluded that adding fruit or fruit juice to the production of mead leads to an increase in the total phenolic and flavonoid content and the overall antioxidant capacity [42]. Similar results were obtained by Adamenko *et al.* [37], who found that mead with the addition of dogwood juice had a significantly higher total phenolic content than the control samples. The total phenolic content in the samples with the added juice was 898.7 mg GAE/L, which is higher than the results obtained in this paper. Kawa-Rygielska *et al.* [32] analyzed mead by adding grape seeds. It was determined that adding this component to the mead increased the total phenolic content in the final products. The content of polyphenolic compounds affects the quality of food products, especially their color, aroma, bitterness, and antioxidant activity [32]. The phenolic content changes during the technological process of production, especially during fermentation, followed by temperature treatment and storage [43].

Table 4. Total phenolic and flavonoid content and antioxidant activity of meads (FRAP, DPPH and ABTS assays).

Sample	Total phenols (mg GAE/mL)	Total flavonoids (mg GAE/mL)	FRAP (mmol Fe^{2+}/mL)	DPPH (μg TE/mL)	ABTS (mg TE/mL)
1A	$312,75^{a}$±1,61	$177,13^{ab}$ ±4,46	$1,99^{a}$±0,01	$42,54^{a}$ ± 0,42	$11,78^{f}$ ± 0,42
1B	$322,28^{a}$ ± 1,80	$188,67^{ab}$ ± 13,70	$2,02^{a}$ ± 0,09	$39,52^{a}$ ± 0,71	$11,31^{ef}$ ± 0,31
1C	$297,61^{a}$ ± 3,39	$156,33^{a}$ ± 11,99	$1,97^{a}$ ± 0,00	$43,59^{a}$ ± 0,90	$10,40^{e}$ ± 0,16
2A	$391,21^{c}$ ± 6,18	$232,93^{c}$± 5,10	$3,36^{c}$ ± 0,01	$157,13^{b}$ ± 13,19	$6,74^{cd}$ ± 0,38
2B	$359,21^{b}$ ± 4,10	$194,67^{b}$± 4,94	$3,31^{bc}$ ± 0,02	$169,62^{bc}$ ± 11,05	$6,74^{cd}$ ± 0,30
2C	$371,61^{bc}$ ± 7,57	$200,93^{b}$± 5,99	$3,27^{b}$ ± 0,02	$191,16^{c}$ ± 15,04	$5,99^{bc}$ ± 1,30
3A	$466,68^{d}$ ± 3,94	$293,00^{d}$ ± 2,74	$4,48^{d}$ ± 0,06	$362,33^{d}$ ± 14,30	$6,97^{cd}$ ± 0,19
3B	$486,88^{de}$ ± 3,29	$308,13^{d}$ ± 4,30	$4,53^{d}$ ± 0,04	$390,01^{e}$ ± 12,67	$7,02^{d}$ ± 0,16
3C	$499,88^{e}$± 6,07	$316,93^{d}$ ± 1,42	$4,91^{e}$ ± 0,03	$387,37^{d}$ ± 17,38	$5,24^{b}$ ± 0,30
4A	$689,36^{f}$ ± 9,52	$474,88^{e}$ ± 11,05	$5,27^{f}$ ± 0,05	$577,42^{g}$ ± 15,46	$3,77^{a}$ ± 0,61
4B	$715,62^{g}$ ± 13,71	$490,61^{e}$ ± 13,12	$5,72^{g}$ ± 0,05	$513,25^{f}$ ± 21,65	$5,12^{b}$ ±0,23
4C	$705,76^{fg}$ ± 37,83	$471,61^{e}$ ± 37,91	$5,98^{h}$ ± 0,02	$559,23^{g}$ ± 21,88	$5,06^{b}$ ± 0,45

The results of the FRAP test ranged from 1.97 mmol Fe^{2+}/mL for sample 1C to 5.98 mmol Fe^{2+}/mL for sample 4C. The results in Table 4 indicate that by increasing the quantity of added chokeberry juice, the FRAP value also increases, *i.e.*, adding 5%, 10%, and 20% chokeberry juice increases the FRAP value by 1.6 times, 2.33 times, and 2.84 times, respectively. Adamenko *et al.* [37] state that the FRAP value in the samples with added dogwood juice was 8 to 39 times higher than in the control samples, which represents more significant changes compared to the changes achieved in this experiment, while Kawa-Rygielska *et al.* [32] state that the addition of chokeberry juice leads to twice as high FRAP values compared to the control samples, which is very similar to the results of this paper.

The result of the DPPH test was lowest in the control sample 1B (39.52 μg TE/mL), while the highest value was measured in sample 4A (577.42 μg TE/mL). Based on the results of the DPPH test, it can be noticed that the increased amount of the added chokeberry juice leads to an increase in the DPPH value. Kawa-Rygielska *et al.* [32] stated that by adding chokeberry

juice to the fermentation solution, the DPPH value increased significantly, up to 3 times higher than the control sample, which was similar to samples 2 to which 5% of chokeberry juice was added; with 20% of the juice added, the DPPH value increased by about 13 times.

The ABTS test involved the IC50 method, where higher values indicated weaker antioxidant properties of the sample. The highest ABTS values were measured in sample 1A (11.78 mg TE/mL), while the lowest values were measured in sample 4A, 3.77 mg TE/mL. The highest ABTS values were recorded in the control samples, while the lowest values were found in the samples with the highest amount of chokeberry juice added. The total phenolic and flavonoid content, FRAP, DPPH, and ABTS tests showed that adding chokeberry juice improved antioxidant properties. The antioxidant activity of mead depends on the chemical composition of raw material but also on the production technology, chemical composition, and additives (fruits, herbs, and spices), which confirms that the addition of chokeberry juice can affect the total antioxidant capacity of a final product [32]. Adamenko *et al.* [37] showed that mead with added dogwood juice had stronger antioxidant properties measured by the DPPH and ABTS tests than the control mead. Also, the results of the FRAP, DPPH, and ABTS tests were mainly significantly different for samples with the same amount of added juice and different concentrations of yeast. The impact of the yeast concentration on the antioxidant capacities of mead, but also other alcoholic beverages, still has not been researched sufficiently, nor can more significant literature be found, which could represent an idea for future research.

Table 5 shows the results of testing the antibacterial activity of mead by applying the agar-well method and agar dilution method for determining the minimum inhibitory concentration (MIC) and the minimum bactericidal concentration (MBC) [22,23]. The results obtained using the agar-well method showed no inhibitory effect against the tested bacteria. The disadvantage of the agar-well method is the relatively long incubation period necessary to detect an inhibition zone that might lead to the evaporation of volatile or the degradation of thermally unstable agents, as well as a small amount of mead used for testing (30 µL), which probably caused the absence of the antibacterial effects of the tested mead. Also, it is impossible to quantify the amount of the antimicrobial agent diffused into the agar medium due to the gradient and matrix network of the agar used for the assay [22]. Because the agar is an aqueous preparation, non-polar compounds will not diffuse as well as polar compounds. Eloff *et al.* [44] have shown that the intermediate polarity compounds have the highest antimicrobial activity. The agar-diffusion method could be useful with a single compound with a known polarity. Even in such a case, if the positive control's polarity differs much from the single compound, comparisons may not be valid [45].

On the other hand, MIC and MBC values showed accurate, reproducible, and reliable results. The MIC and MBS values of mead concerning four bacteria are shown in Table 5. In most cases, sample 1 (the control sample) showed the best antimicrobial activity, while sample 2 (with 5% added chokeberry juice) showed the weakest effect. Following the control sample, the sample with 20% of added chokeberry juice showed the strongest effect, which still indicates the impact the quantity of added juice has on the antimicrobial effect of mead. The obtained results are not in compliance with the results of measuring the antimicrobial effect, where it has been found that adding chokeberry juice positively affected the antioxidant properties of mead. In the available literature, there is not much data on the antimicrobial effect of mead. Still, data on the antimicrobial effect of similar products, such as beer, wine, and related products, are available. The influence of different factors has been tested with these products, such as the type and quantity of raw materials used, amount of alcohol, acidity, the content of phenolic compounds, etc. A lot of data on the antimicrobial effect of honey and chokeberry, the raw material used in this paper, can be found in the literature. Stojković *et al.* [46] tested the antibacterial effect of honeydew honey, processed through various treatments, on four bacteria also used in this paper. This study showed that G (-) bacteria were more strongly inhibited than G (+) bacteria, which is not in line with the results from many authors [47,48]. The results of this study are interesting because of the phenolic content of sample 4, which showed that the strongest antibacterial effect was among the lowest measured, similar to mead without added chokeberry juice. Hence, it follows that the antimicrobial properties of honeydew honey could be attributed to the individual or synergetic effects of different factors, not only from phenolic compounds' content. The antimicrobial activity of honey is affected by a number of factors, such as high osmotic pressure, water activity, pH value, production of H_2O_2, methylglyoxal, antimicrobial peptide bee defensin-1, lysozyme, phenolic acids, flavonoids, etc. [47,49]. The peroxide activity of honey may be destroyed by heat, light, and long-term storage of honey, and the antimicrobial activity of honeydew honey and honeydew mead could therefore be explained by the combined effect of the non-peroxide (high concentration of phenolics and flavonoids) and the

Table 5. Antimicrobial activity of meads and antibiotic discs (diameter of inhibition zone), minimum inhibitory (MIC), and minimum bactericidal concentration (MBC) of meads on bacterial cultures growth

	Sample	*Escherichia coli ATCC 25922*	*Staphylococcus aureus ATCC 25923*	*Pseudomonas aeruginosa ATCC 10145*	*Bacillus cereus ATCC 7004*
1A	Disc-diffusion (mm)	*NA	*NA	*NA	*NA
	MIC % (v/v)	30	30	30	30
	MBC % (v/v)	40	40	40	40
1B	Disc-diffusion (mm)	*NA	*NA	*NA	*NA
	MIC % (v/v)	30	30	30	30
	MBC % (v/v)	40	40	40	40
1C	Disc-diffusion (mm)	*NA	*NA	*NA	*NA
	MIC % (v/v)	30	30	30	30
	MBC % (v/v)	40	40	40	40
2A	Disc-diffusion (mm)	*NA	*NA	*NA	*NA
	MIC % (v/v)	40 %	>40 %	40 %	40 %
	MBC % (v/v)	>40 %	>40 %	40 %	>40 %
2B	Disc-diffusion (mm)	*NA	*NA	*NA	*NA
	MIC % (v/v)	40 %	>40 %	40 %	40 %
	MBC % (v/v)	>40 %	>40 %	40 %	>40 %
2C	Disc-diffusion (mm)	*NA	*NA	*NA	*NA
	MIC % (v/v)	40 %	>40 %	40 %	40 %
	MBC % (v/v)	>40 %	>40 %	40 %	>40 %
3A	Disc-diffusion (mm)	*NA	*NA	*NA	*NA
	MIC % (v/v)	40	40	30	30
	MBC % (v/v)	40	>40	40	>40
3B	Disc-diffusion (mm)	*NA	*NA	*NA	*NA
	MIC % (v/v)	40	40	30	30
	MBC % (v/v)	40	>40	40	>40
3C	Disc-diffusion (mm)	*NA	*NA	*NA	*NA
	MIC % (v/v)	40	40	30	30
	MBC % (v/v)	40	>40	40	>40
4A	Disc-diffusion(mm)	*NA	*NA	*NA	*NA
	MIC % (v/v)	30	30	30	30
	MBC % (v/v)	40	>40	30	>40
4B	Disc-diffusion(mm)	*NA	*NA	*NA	*NA
	MIC % (v/v)	30	30	30	30
	MBC % (v/v)	40	>40	30	>40
4C	Disc-diffusion(mm)	*NA	*NA	*NA	*NA
	MIC % (v/v)	30	30	30	30
	MBC % (v/v)	40	>40	30	>40
Ampicillin 10 mg (mm)		16.00±4.39	33.00±2.16	*NA	10.88±2.53
Ciprofloxacin 5 mg (mm)		37.00±3.37	29.25±2.99	33.33±0.58	27.38±3.54
Erytromycin 15 mg (mm)		10.75±1.50	27.75±2.99	*NA	24.5±2.52
Gentamicin 10 mg (mm)		25.50±1.29	29.75±1.90	21.33±1.53	24±2.53

*NA- no activity.

peroxide antimicrobial activity, low pH value, high concentration of sugar, etc. Fikselova *et al.* [50] studied the antimicrobial activity of several kinds of honeydew honey and found that the most sensitive bacteria strains were *E. coli* and *P. aeruginosa*, while *B. cereus* was the most resistant. In contrast, Srećković *et al.* [51] found

that honeydew honey was more effective against G (+) bacteria compared to G (-). Nicodim *et al.* [52] examined the effect of temperature on the antibacterial activity of honey and found that the lower temperatures (30 °C and 50 °C) did not have any effect on its antibacterial properties, while the antibacterial activity was reduced at the temperature of 70 °C.

The content of alcohol in mead, which was more or less balanced, did not affect the antibacterial properties of mead, which is in accordance with the previous studies related to wine, in which the content of alcohol ranged from 10% v/v to 13% v/v, where it was too low to show the bactericidal effect [53,54]. Radovanović *et al.* [54] and Vulić *et al.* [55] determined that the combination of organic acids (lactic, malic, acidic, and tartaric) and ethanol contributed to this stronger antimicrobial effect of the wine. However, the role of phenolic compounds is not completely clear because different opinions can be found in the literature. In their studies, Sheth *et al.* [56] and Arima *et al.* [57] suggested that compounds such as flavonoids (quercetin and quercetin-3-glucoside) and monomeric anthocyanins might be used as biochemical markers that contributed to the antimicrobial activity of red wines. However, Boban *et al.* [58], to clarify the role of polyphenols, pH, ethanol, and other wine components, tested the antimicrobial effects of intact wine compared to that of phenols-stripped wine, dealcoholized wine, ethanol, and low pH applied separately and in combination. They concluded that the antibacterial activity of the samples could not be related to their total phenolics and resveratrol content, ethanol content, or pH. After intact wine, the phenols-stripped wine had the strongest antimicrobial effect against *Salmonella enterica* and *E. coli*, so the authors concluded that nonphenolic constituents of wine were responsible for a major part of its antimicrobial activity. Krisch *et al.* [59] tested the antibacterial effect of extracts and juices of many different fruits. They determined that juices and extracts had low pH (from 2.8 to 5.5), which originated from weak organic and phenolic acids, which in the undissociated form (mainly on pH 3–5) can interact with cell membranes and penetrate the cells causing acidification of the cytoplasm. However, in their experiment, there was only a weak correlation between the acidity of the samples and their antibacterial effect. Krstić [60] tested the alcohol extract and chokeberry juice and determined the absence of the effect of juice on a large number of bacteria tested through the agar-well method. In contrast, MBC values in the juice were mainly over 20 mg/mL.

When preparing the mead, honey was diluted in a 1:3 ratio, which reduced the initial concentration of honey in a sample. Then, it was pasteurized, which might have influenced the antibacterial properties of the mead. Besides, the juice was pasteurized too, which also might have influenced the antibacterial properties of mead, even though the antioxidant properties were preserved. Further studies are needed to clarify the mechanism of the antimicrobial action of different compounds of meads. Still, the antimicrobial activity of a complex solution such as mead is based on more than one compound.

CONCLUSION

Adding chokeberry juice improved the final product's antioxidant properties and positively affected the course of the fermentation of mead with a fairly good overlap of the curves predicted by the model with the experimentally obtained data. Regarding the chemical composition of the mead, there is no significant difference, except in the content of obtained ethanol, which is the highest in the samples with 10% of added chokeberry juice. The control sample showed the best antimicrobial activity, while the sample with the least amount of added chokeberry juice showed the weakest effect. Among the samples with added chokeberry juice, the sample with the highest amount of added juice showed the strongest effect, which still indicated the impact of the quantity of added juice on the antimicrobial effect of mead.

REFERENCES

[1] Codex Standard for Honey 12-1981, Rev.1 (1987), Rev. 2 (2001)1 https://alimentosargentinos.magyp.gob.ar/contenido/marco/Codex_Alimentarius/normativa/codex/stan/CODEX_STAN_12.htm.

[2] A. Wilczyńska, Polish J. Food Nutr. Sci. 60 (2010) 309–313. http://journal.pan.olsztyn.pl/pdf- 98274- 31027?filename=PHENOLIC%20CONTENT%20AND.pdf.

[3] M. Bucekova, M. Buriova, L. Pekarik, V. Majtan, J. Majtan, Sci. Rep. 8 (2018) 1–9. https://doi.org/10.1038/s41598-018-27449-3.

[4] D. Šmorgovičová, P. Nádaský, R. Tandlich, B.S. Wilhelmi, G. Cambray, Czech J. Food Sci. 30 (2012) 241–246. https://doi.org/10.17221/113/2011-CJFS.

[5] G.I. Dezmirean, L.A. Mărghitaş, O. Bobiş, D.S. Dezmirean, V. Bonta, S. Erler, J. Agric. Food Chem. 60 (2012) 8028–8035. https://doi.org/doi.org/10.1021/jf3022282.

[6] Y. Teramoto, R. Sato, S. Ueda, Afr. J. Biotechnol. 4 (2005) 160–163. https://doi.org/10.4314/AJB.V412.15072.

[7] P. Vargas, R. Gulling, Making Wild Wines & Meads, Storey Publishing, United States (1999), p.122 ISBN: 1580171826.

[8] A. Savić, A. Velemir, S. Papuga, M. Stojković, Foods Raw

Mater. 9 (2021) 146–152. https://doi.org/10.21603/2308-4057-2021-1-146-152.

[9] A. Iglesias, A. Pascoal, A.B. Choupina, C.A. Carvalho, X. Feás, L.M. Estevinho, Molecules 19 (2014) 12577–12590. https://doi.org/10.3390/molecules190812577.

[10] J. Šnebergová, H. Čižková, E. Neradová, B. Kapci, A. Rajchl, M. Voldřich, Czech J. Food Sci. 32 (2014) 25–30. https://doi.org/10.17221/540/2012-CJFS.

[11] P. Denev, M. Číž, M. Kratchanova, D. Blazheva, Food Chem. 284 (2019) 108–117. https://doi.org/10.1016/j.foodchem.2019.01.108.

[12] A. Bataraga, V. Valkovska, Key Eng. Mater. 850 (2020) 184-189. https://doi.org/10.4028/www.scientific.net/KEM.850.184.

[13] M.J. Dodić, D.G. Vučurović, S.N. Dodić, J.A. Grahovac, S.D. Popov, N.M. Nedeljković, Appl. Energy 99 (2012) 192–197. https://doi.org/10.1016/j.apenergy.2012.05.016.

[14] H.S. Lakićević, I.T. Karabegović, N.Č. Nikolić, M.G. Petrović, S.A. Đorđević, L.M. Lazić, Adv. Technol. 7 (2018) 11–18. https://doi.org/10.5937/SavTeh1802011L.

[15] International Code of Oenological Practices. International Organisation of Vine and Wine, Paris (2021) https://www.oiv.int/sites/default/files/publication/2022-10/International%20Code%20of%20oenlogical%20practices.pdf.

[16] M.L. Wang, Y.M. Choong, N.W. Su, M.H. Lee, J. Food Drug Anal. 11 (2003) 133–140. https://doi.org/10.38212/2224-6614.2710.

[17] K. Wolfe, R.H. Liu, J. Agric. Food Chem. 51 (2003) 1676–1683. https://doi.org/10.1021/jf020782a.

[18] A.A.L. Ordonez, J.D. Gomez, M.A. Vattuone, M.I. Isla, Food Chem. 97 (2006) 452–458. https://doi.org/10.1016/j.foodchem.2005.05.024.

[19] W. Brand-Williams, M.E. Cuvelier, C. Barset, LWT - Food Sci. Technol. 28 (1995) 25–30. https://doi.org/10.1016/S0023-6438(95)80008-5.

[20] R. Re, N. Pellegrini, A. Proteggente, A. Pannala, M. Yang, C. Rice-Evans, Free Radical. Biol. Med. 26 (1999) 1231–1237. https://doi.org/10.1016/s0891-5849(98)00315-3.

[21] I.F.F. Benzie, J.J. Strain, Anal. Biochem. 239 (1996) 70–76. https://doi.org/10.1006/abio.1996.0292.

[22] M. Balouiri, M. Sadiki, S.K. Ibnsouda, J. Pharm. Anal. 6 (2016) 71–79. https://doi.org/10.1016/j.jpha.2015.11.005.

[23] Determination of minimum inhibitory concentrations of antibacterial agents by agar dilution, EUCAST (2000). https://doi.org/10.1046/j.1469-0691.2000.00142.x.

[24] N.N. Verović, MSc Thesis, University of Niš (in Serbian) (2018) https://www.pmf.ni.ac.rs/download/master/master_radovi_geografija/geografija_master_radovi/2018/2018-10-30-vn.pdf.

[25] A.P. Pereira, A. Mendes-Ferreira, J.M. Oliveira, L.M. Estevinho, A. Mendes-Faia, Food Microbiol. 33 (2013) 114–123. https://doi.org/10.1016/j.fm.2012.09.006.

[26] P. Sroka, P. Satora, Food Hydrocolloids 63 (2017) 233–239. https://doi.org/10.1016/j.foodhyd.2016.08.044.

[27] A.M. Martínez, G.J. Vivas, M.C. Quicazán, Chem. Eng. Trans. 49 (2016) 19–24. https://doi.org/10.3303/CET1649004.

[28] S.S.D. Mohammed, B. Yohanna, J.R. Wartu, N.L. Abubakar, S. Bello, Int. J. Biol. Sci. 10 (2018) 52–61. https://doi.org/10.5539/ijb.v10n3p52.

[29] A. Mendes-Ferreira, F. Cosme, C. Barbosa, V. Falco, A. Inês, A. Mendes-Faia, Int. J. Food Microbiol. 144 (2010) 193–198. https://doi.org/10.1016/j.ijfoodmicro.2010.09.016.

[30] P. Sroka, T. Tuszyński, Food Chem. 104 (2007) 1250–1257. https://doi.org/10.1016/j.foodchem.2007.01.046.

[31] A.P. Pereira, A. Mendes-Ferreira, L.M. Estevinho, A. Mendes-Faia, J. Inst. Brew. 121 (2015) 405–410. https://doi.org/10.3390/microorganisms7100404.

[32] J. Kawa-Rygielska, K. Adamenko, A.Z. Kucharska, K. Szatkowska, Food Chem. 283 (2019) 19–27. https://doi.org/10.1016/j.foodchem.2019.01.040.

[33] H. Akalin, M. Bayram, R.E. Anli, J. Inst. Brew. 123 (2017) 167–174. https://doi.org/10.1002/jib.396.

[34] M. Bely, I. Masneuf-Pomarède, D. Dubourdieui, J. Int. Sci. Vigne Vin 39 (2005) 191–197. https://doi.org/.20870/oeno-one.2005.39.4.886.

[35] C.H. Chen, Y.L. Wu, D. Lo, M.C. Wu, J. Inst. Brew. 119 (2013) 303–308. https://doi.org/10.1002/jib.95.

[36] A.P. Pereira, A. Mendes-Ferreira, J.M. Oliveira, L.M. Estevinho, A. Mendes-Faia, Food Microbiol. 33 (2013) 114–123. https://doi.org/10.1016/j.fm.2012.09.006.

[37] K. Adamenko, J. Kawa-Rygielska, A.Z. Kucharska, N. Piórecki, Molecules 23 (2018) 2024–2037. https://doi.org/10.3390/molecules23082024.

[38] T. Gomes, T. Dias, V. Cadavez, J., Verdial, J. S. Morais, E. Ramalhosa, L.M. Estevinho, Pol. J. Food Nutr. Sci. 65 (2015) 137–142. https://doi.org/10.1515/pjfns-2015-0006.

[39] K.A. Roni, D. Kartika, H. Apriyadi, N. Herawati, J. Comput. Theor. Nanosci. 16 (2019) 5228–5232. https://doi.org/10.1166/jctn.2019.8591.

[40] S. Czabaj, J. Kawa-Rygielska, A.Z. Kucharska, J. Kliks, Molecules 22 (2017) 803–818. https://doi.org/10.3390/molecules22050803.

[41] U. Miljić, Ph.D. Thesis, University of Novi Sad (in Serbian) (2015) https://nardus.mpn.gov.rs/handle/123456789/1815?locale-attribute=sr_RS.

[42] A.C. Şarba, Ph.D. Thesis, University of Cluj-Napoca (2015) (in English) www.usamvcluj.ro/en/files/teze/en/2015/Şarba.pdf.

[43] D. Kahoun, S. Řezková, K. Veškrnová, J. Královský, M. Holčapek, J. Chromatogr. A 1202 (2008) 19–33. https://doi.org/10/1016/j.chroma.2008.06.016.

[44] J.N. Eloff, I.E. Angeh, L.J. McGaw, Ind. Crop. Prod. 110 (2017) 103–112. https://doi.org/10.1016/j.indcrop.2017.11.014.

[45] J.N. Eloff, BMC Complementary Altern. Med. 19 (2019) 106–114. https://doi.org/10.1186/s12906-019-2519-3.

[46] M. Stojković, D. Cvetković, A. Savić, Lj. Topalić-Trivunović, A. Velemir, S. Papuga, M. Žabić, J. Food Sci. Technol. 58 (2021) 2555–2566. https://doi.org/10.1007/s13197-020-04762-2.

[47] P.C. Molan, Bee World 73 (1992) 5–28. https://doi.org/10.1080/0005772X.1992.11099109.

[48] S. Bogdanov, LWT- Food Sci. Technol. 30 (1997) 748–753.

https://doi.org/10.1016/fstl.1997.0259.

[49] F.J. Leyva-Jimeneza, J. Lozano-Sanchez, I. Borras-Linares, M.L. Cadiz-Gurrea, E. Mahmoodi-Khaledi, LWT-Food Sci. Technol. 101 (2019) 236–245. https://doi.org/10.1016/j.lwt.2018.11.015.

[50] M. Fikselova, M. Kačaniova, L. Hleba, M. Mellen, N. Vučković, M. Dzugan, Anim. Sci. Biotechnol. 47 (2014) 218–224. https://web.archive.org/web/20180502025911id_/http://www.spasb.ro/index.php/spasb/article/viewFile/1697/1722.

[51] N.Z. Srećković, V.B. Mihailović, J.S. Katanić-Stanković, Kragujev. J. Sci. 41 (2019) 53–68. https://doi.org/10.5937/KgJSci1941053S.

[52] M.E. Weise, B. Eberly, D.A. Person, BMJ 311 (1995) 1657–1660. https://doi.org/10.1136/bmj.311.7021.1657.

[53] M.J.R. Vaquero, M.R. Alberto, M.C.M. de Nadra, Food Control 18 (2007) 93–101. https://doi.org/10.1016/j.f00dc0nt.2005.08.010.

[54] A. Radovanović, B. Radovanović, B. Jovančićević, Food Chem. 117 (2009) 326–331. https://doi.org/10.1016/j.foodchem.2009.04.008.

[55] J.J. Vulić, T.N. Cebović, V.M. Candanović, G.S. Cetković, S.M. Đilas, J.M. Candanović-Brunet, J.M. Velićanski, D.D. Cvetković, V.T. Tumbas, Food Funct. 4 (2013) 713–721. https://doi.org/10.1039/c3fo30315b.

[56] N.K. Steth, T.R. Wisniewski, T.R. Franson, Am. J. Gastroenterol. 83 (1988) 658–660. https://pubmed.ncbi.nlm.nih.gov/3287903/.

[57] H. Arima, H. Ashida, G. Danno, Biosci. Biotechnol. Biochem. 66 (2002) 1009–1014. https://10.1271/bbb.66.1009.

[58] N. Boban, M. Tonkic, D. Budimir, D. Modun, D. Sutlovic, V. Punda-Polic, M. Boban, J. Food Sci. 75 (2010) 322–326. https://10.1111/j.1750-3841.2010.01622.x.

[59] J. Krisch, G. László, M. Tölgyesi, T. Papp, C. Vágvölgyi, Acta Biol. (Szeged) 52 (2008) 267–270. https://abs.bibl.u-szeged.hu/index.php/abs/article/view/2639/2631.

[60] T. Krstić, Ph.D. Thesis, University of Novi Sad (in Serbian) (2018) https://nardus.mpn.gov.rs/handle/123456789/11068.

MAJA MILIJAŠ[1]
DRAGOLJUB CVETKOVIĆ[2]
ALEKSANDAR SAVIĆ[1]
ANA VELEMIR[1]
LJILJANA TOPALIĆ-TRIVUNOVIĆ[1]
SAŠA PAPUGA[1]

[1]Tehnološki fakultet, Univerzitet u Banjoj Luci, Banja Luka, Republik Srpska

[2]Tehnološki fakultet, Univerzitet u Novom Sadu, Novi Sad, Srbija

NAUČNI RAD

UTICAJ DODATKA RAZLIČITIH KOLIČINA KVASCA I VOĆNOG SOKA OD ARONIJE NA FERMENTACIJU MEDOVINE

Med predstavlja nutritivno visoko vrijedan proizvod, koji se kao sirovina koristi za dobijanje medovine. Kvalitet medovine može da se poboljša dodatkom voćnih sokova, a među njima i sokom od aronije. Cilj ovog rada je ispitivanje uticaja dodatka različitih količina soka od aronije (5%, 10% i 20%) u rastvore za fermentaciju, uz varijaciju 3 količine inokuliranog kvasca (150 mg/l, 300 mg/l i 600 mg/l), na tok fermentacije, fizičko-hemijska, antioksidativna i antimikrobna svojstva medovina. Od fizičko-hemijskih parametara u medovini je analiziran sadržaj suve materije, pH vrednost i sadržaj isparljivih kiselina, etanola i metanola. Analiza antioksidativnih svojstava je podrazumevala je određivanje sadržaja ukupnih fenola i flavonoida, FRAP, DPPH i ABTS testove. Testiranje antimikrobnih svojstava medovina vršeno je primenom dve metode. Rezultati dobijeni u ovom radu ukazuju da je dodatak soka od aronije poboljšao antioksidativna svojstva finalnog proizvoda, a pozitivno je uticao i na tok fermentacije medovine, odnosno doveo je do povećanja maksimalne koncentracije etanola (Pm). U pogledu hemijskog sastava medovina ne postoji značajna razlika, osim u sadržaju dobijenog etanola, koji je najveći kod uzoraka sa 10% dodanog soka od aronije. Uzorak 1 (kontrolni uzorak) pokazao je najbolju antimikrobnu aktivnost, dok je najslabije dejstvo pokazao uzorak 2 (sa 5% dodanog soka od aronije). Nakon kontrolnog uzorka, najjače dejstvo pokazao je uzorak sa 20% dodanog soka od aronije.

Ključne reči: antimikrobna aktivnost, antioksidativna aktivnost, aronija, brzina fementacije, kinetički model, medovina.

CI&CEQ
Chemical Industry & Chemical Engineering Quarterly

Available online at
Association of the Chemical Engineers of Serbia AChE
www.ache.org.rs/CICEQ

Chem. Ind. Chem. Eng. Q. 29 (2) 161–167 (2023) CI&CEQ

PONGAYI PONNUSAMY SELVI[1]

RAJOO BASKAR[2]

[1]Department of Chemical Engineering, Kongu Engineering College, Perundurai, Tamil Nadu, India

[2]Department of Food Technology, Kongu Engineering College, Perundurai, Tamil Nadu, India

SCIENTIFIC PAPER

UDC 502/504:546.264-31

CO_2 MITIGATION STUDIES IN PACKED ABSORPTION COLUMN USING IRON OXIDE NANOFLUID

Article Highlights

- Experiments were carried out with ferromagnetic nanofluids since the agglomeration was less
- The chemical precipitation method was employed for the synthesis of iron oxide nanoparticles
- Characterization was done by SEM, TEM, and XRD analysis

Abstract

The challenging task in our ecosystem is to reduce acidic gas emissions to some extent. Many gases are emitted from the industries like H_2S, CO, CO_2, SO_2, NO, and NO_2 as exhaust gases. Among these gases, CO_2, NO_2, and SO_2 are acidic, which results in adverse effects on humans, animals, and plants. The increase in the emission of CO_2 gases from both anthropogenic and industrial sources resulted in CO_2 mitigation studies. CO_2 absorption studies were carried out using iron oxide nanofluid with the novel structured packed absorption column. Iron oxide nanoparticles were synthesized and characterized using XRD, SEM, and TEM analysis. Ammonia is used as an absorbent along with iron oxide nanofluid of three different concentrations (0.0001 w/v%, 0.001 w/v%, and 0.0015 w/v%). It was found that the iron oxide nanofluid of 0.0015 w/v% showed an improved % CO_2 removal efficiency. This enhanced % CO_2 removal efficiency was due to the increased interfacial area of the ameliorated contact between the liquid and gas phases. In addition, the magnetic field was introduced along with the packed column, which increased CO_2 removal efficiency by 1.5%.

Keywords: absorption, CO_2 removal efficiency, interfacial area, mass transfer coefficient, nanofluid, packed column.

The enormous increase in CO_2 emission resulted in rapid climatic changes, ozone layer depletion, and global warming. The increased emission of greenhouse gases into the atmosphere resulted in variable climatic conditions that paved the way for the increased atmospheric temperature [1]. Green plants utilize CO_2 present in the atmosphere during photosynthesis for food preparation for plants. But today, due to deforestation, CO_2 has not been consumed by plants, resulting in an enormous amount in the environment. Research has found that the increase in CO_2 content raises global warming [2,3]. Global Carbon Project has found an increase in CO_2 emission to about 1.9% in 2019 and 2.7% in 2021. A special Intergovernmental Panel on Climate Change report reported that carbon emissions should fall to 50% by 2030 to keep global temperatures within 1.5 °C [4,5]. An increase in coal consumption by 7.1% in India and 4.5% in China causes the release of CO_2 into the atmosphere more than the standard limit [6,7]. Two methods can shift the trend line from an increase in CO_2 emission. One is to support emission reduction, and the other is to restrict the growth of the nations that increases the emission of CO_2 [8,9,10]. The increase in the growth of renewable and low-carbon technologies accounts for strengthening emission reduction. Recent technological development should monitor the climatic impacts and drive CO_2 emission to zero by 2050 [11].

Correspondence: P.P.Selvi, Department of Chemical Engineering, Kongu Engineering College, Perundurai, Erode-638 060, Tamil Nadu, India.
E-mail: selvi.chem@kongu.edu
Paper received: 10 May, 2021
Paper revised: 5 April, 2022
Paper accepted: 1 September, 2022

https://doi.org/10.2298/CICEQ210510023S

Most of the CO_2 emission is from power plants and chemical industries. Hence advancements should be made to the present CO_2 capture technology to reduce the emission [12,13]. One such technology is Carbon Capture Sequestration (CCS). Among them, the absorption of CO_2 by chemical solvents is technically promising and can be commercialized. Research has found that the amine solutions account for the increased carbon dioxide absorption rate. Recent literature studies prove that ammonia is a promising solvent for this purpose [14]. The major advantage of ammonia over other amine solutions is that it does not degrade easily during solvent regeneration, has low energy input, and has no corrosion problem [15]. Furthermore, the use of structured packing provides the uniform distribution of the gas and solvent flow inside the absorption column and thereby increases the % CO_2 removal [16,17]. Recently nanofluids have attracted the attention of researchers for their improved functionality. It is found that the presence of iron oxide nanofluid increases the absorption of carbon dioxide into the solvent by the mechanisms like the grazing or shuttle mechanism and Brownian movement [18].

The ammonia (NH_3) solvent was used as the absorbent for further studies. Further, the % CO_2 removal, mass transfer rate per unit volume, mass transfer coefficient, mass flux, number of transfer units (NTU), and height of transfer units (HTU) for structured packing materials were studied. The structured packing material shows a better result for CO_2 absorption than the random packing material. The column loaded with the structured packing material was investigated with 12% (v/v) NH_3 concentration. To identify the best condition, 12% (v/v) solvent concentration provides higher % CO_2 removal than the other solvent concentrations. Further, the study continued to examine the enhancement of CO_2 absorption by synthesizing and adding iron oxide nanofluids. The effect of iron oxide nanofluid concentration on the % enhancement in CO_2 absorption was also studied and reported. Further, the impact of applying a magnetic field on CO_2 absorption while employing solvent with Fe_3O_4 nanoparticles was also investigated. The introduction of nanofluids was found to have a significant impact on enhancing CO_2 absorption. Iron oxide nanofluid has a wide range of applications in many fields and has good commercial potential for absorption studies. Experiments are carried out with ferromagnetic nanofluids since the agglomeration is less with ammonia as the base fluid. Many researchers used amine solvents, but only limited work is available in the literature. The chemical precipitation method is employed for the synthesis of iron oxide nanoparticles. Characterization has been done by SEM, TEM, and XRD analysis. The mass diffusion enhancement mechanism is Brownian movement, and mass diffusion reduction mechanisms are aggregation and clustering.

MATERIALS AND METHODS

Synthesis of iron oxide

Iron oxide nanoparticles were synthesized by the chemical precipitation method. First, 4 g of hydrated ferrous sulfate and hydrated ferric chloride were dissolved in 300 ml of distilled water. When the reaction temperature (80 °C) was reached, 48 ml of alkaline solution (27% NH_4OH) was added drop by drop. After this, heating and stirring continued for another 40 minutes. The brown precipitate obtained was cooled overnight. Then the precipitate was filtered, washed with distilled water and alcohol, and dried in the oven at 100 °C. Finally, the synthesized Iron oxide nanoparticles were placed in Sonicator to increase the nanofluid's stability.

XRD analysis

The Fe3O4 nanoparticles were prepared at room temperature for XRD analysis. It shows that the nanoparticles were crystalline. Fig. 1 shows the XRD analysis report of Fe3O4 nanoparticles. The most intensive lines were observed with diffraction peaks at 2θ= 36.2 and 64.1. The graph shows that Fe3O4 was in a cubic structure. The broad peaks indicate that the particles were very fine with a crystalline structure. The size of the particle was determined using Debye Scherer's formula:

XRD analysis

At the end of fermentations, the oenological parameters of mead: pH value, volatile acidity, and dry matter content, were measured [15].

The content of ethanol and methanol in mead was determined by the GC-FID method at Clarus 680 Perkin Elmer instrument with the FID detector, Elite-Wax L 60 m column, ID 0.32, DF 0.5, absolute ethanol and methanol standards, with acetonitrile as the internal standard. The injector and detector temperature of 250 °C, a sample volume of 0.5 µL, and a temperature regime of 45 °C (2 min), 45 °C/min to 245 °C (1 min). The total duration was 7.44 min, and the flow was 3 mL/min [16].

$$D = k\lambda / \beta \cos\theta \quad (1)$$

where k = 0.89 is the shape factor, λ is the X-ray wavelength of CuKα radiation, β is the full width at half maximum of the peaks, and θ is the glancing angle. The average crystallite size is 49.9 nm.

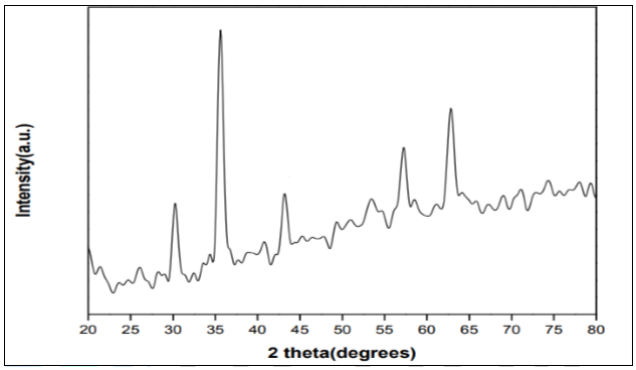

Figure 1. XRD analysis of Fe_3O_4 nanoparticles.

SEM analysis

Scanning electron microscopy (SEM) was done for the Fe_3O_4 nanoparticles, revealing the surface topography. The SEM image indicates that the particles are spherical and have well-connected grain regions. The flower-like architecture is built from several nanosheets. Fig. 2 represents the magnified SEM image of nanosheets on the spherical surface having a void.

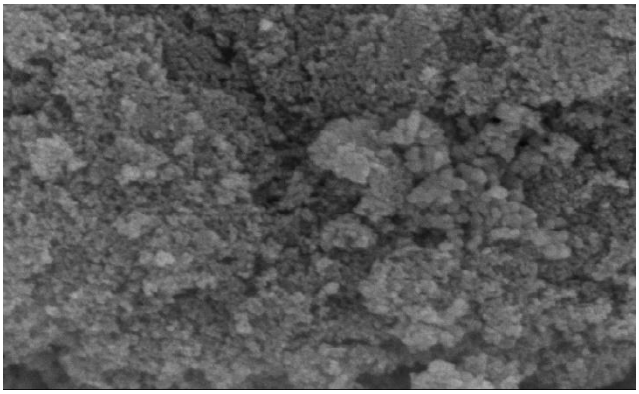

Figure 2. SEM analysis of Fe_3O_4 nanoparticles.

TEM analysis

The morphology and the size study of the synthesized Fe_3O_4 nanoparticles were done using the transmission electron microscope (TEM). The samples were prepared by dispersing the particles in de-ionized water under sonication for 30 minutes, then placing the drop onto a copper grid coated with a layer of amorphous carbon. Fig. 3 shows the TEM image of Fe_3O_4 at 50 nm magnification. The image shows that the particles were spherical when combined with the SEM image. It also shows that the particles were uniformly distributed and well connected. From this micrograph, the particles have an average diameter of 50 nm, which agrees with the result obtained by XRD.

The following equation gives the CO_2 absorption rate (NA) in the absorbent:

$$N_A = K_G P\left(y - y^*\right) \tag{2}$$

where K_G is the overall mass transfer coefficient, P is the system pressure, y is the mole fraction of the components in the gas phase, and y^* is the equilibrium mole fraction of components in the gas phase. The number of transfer units (NTU) is given by:

$$NTU = \ln\left(\frac{y_1}{y_2}\right) \tag{3}$$

where y_1 and y_2 are the outlet and inlet CO_2 concentrations.

Likewise, the height of the transfer units (HTU) is given by:

$$HTU = \frac{z}{NTU} \tag{4}$$

where z is the total height of the packed tower.

The gas partial pressure (ΔP_L) is the log mean average of inlet and outlet partial pressures. The overall mass transfer coefficient is determined by:

$$K_G\alpha = \frac{N_A}{z\ A_C\ P_T\ \Delta y} \tag{5}$$

where K_G is the mass transfer coefficient, α is the specific interfacial area in m^2/m^3, Ac is the area of the column in m^2, P_T is the total pressure in atm, and Δy is the difference in the mole fraction.

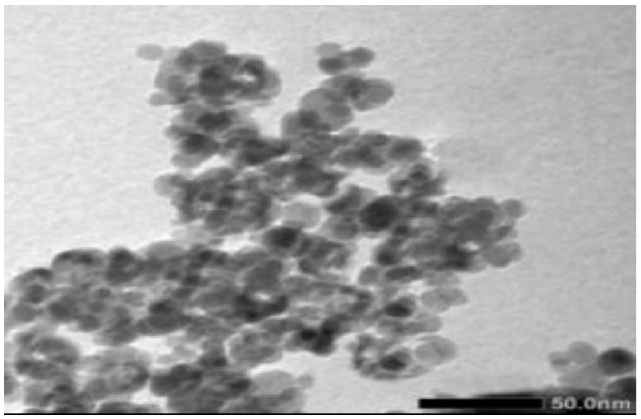

Figure 3. TEM analysis of Fe_3O_4 nanoparticles.

Experimental setup

The experimental setup for the packed absorption column is shown in Fig. 4. The packed column was made of glass with 0.6 m in height and 0.05 m inside diameter. The column was filled with a laboratory BX-DX structured packing material with an outer diameter of 0.045 m and a height of 0.05 m. The porosity of the packing material is 90%, and the specific surface area is about 250 m^2/m^3–750 m^2/m^3. Experimental conditions of the structured packed column are given in Table 1.

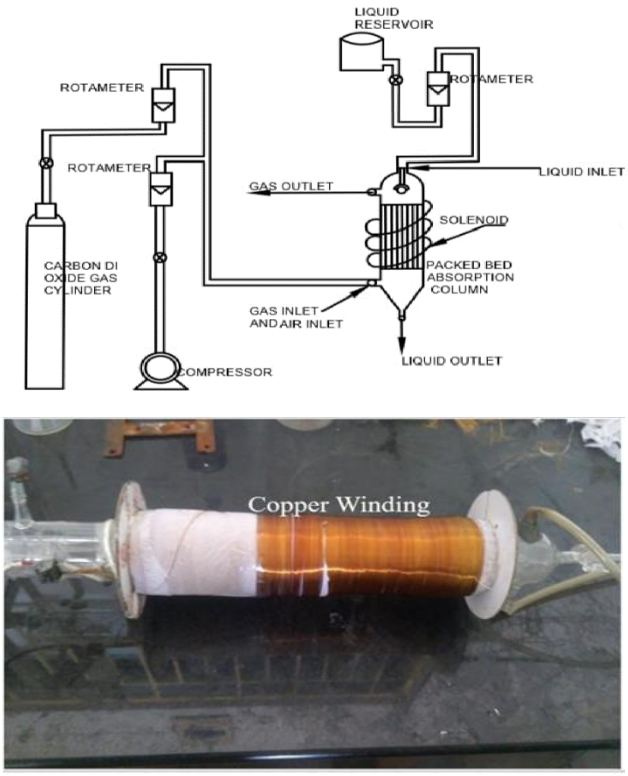

Figure 4. Schematic diagram of the experimental setup with the external magnetic field.

Table 1. Experimental conditions of the structured packed column.

No.	Parameter	Conditions
1	Absorption solvent	Aqueous NH_3 solution
2	Gas flow rate, L min^{-1}	9, 12, 14, 17, 19, 21, 23
3	CO_2: Air ratio	4:1
4	Liquid flow rate, L h^{-1}	
5	NH_3 conc. % (v/v)	2, 4, 6, 8, 10, 12
6	Temperature, °C	28

Both the gas and solvent flow rates were controlled by the flow meters. The CO_2 gas and the compressed air were passed through the packed column from its bottom. When the mixture gas reached a steady state, the aqueous ammonia solution was pumped into the column from its top. After that, the reacted sample was collected in the reservoir. The collected reacted sample was titrated against 0.1N HCl because ammonium carbonate was formed during the reaction of the gas mixture, which was a weak base and should be titrated against strong acid. The iron oxide nanoparticles were taken at 0.0001% (w/v), 0.001% (w/v), and 0.0015% (w/v). For stability of nanoparticles in the base liquid, it was kept in the ultra sonicator for 3 h. The prepared nanoparticle was immediately sent to the container and used in the CO_2 capture to prevent the deposition of the nanoparticles [19,20].

A coil of 1.1 mm thick copper wire with windings was wrapped around the external surface of the absorption column to generate a homogeneous magnetic field. The height of the coil was 0.5 m, placed in the middle part of the column, and a maximum electrical current of 2 A was applied to the coil.

RESULTS AND DISCUSSION

CO_2 absorption with structured packing employing iron oxide nano fluid with solvent

Iron oxide nanoparticles were dissolved in the 12% (v/v) ammonia solvent at concentrations ranging from 0.0001% (w/v) to 0.0015% (w/v). A significant increase in CO_2 absorption was seen at 0.0001% (w/v), 0.001% (w/v), and 0.0015% (w/v). Among them, 0.0015% (w/v) at 12% (v/v) ammonia shows better results. The removal efficiency was increased to 98%, which was previously 74% at 12% (v/v) ammonia without nanofluids. It was also found that there was a significant increase in the absorption rate, NTU, and mass transfer coefficient when iron oxide nanofluids were introduced. Compared to graphene oxide nanoparticles, iron oxide-based nanofluids show 5% better CO_2 absorption because the size of the iron oxide nanoparticles was 50 nm, much less than 100 nm graphene oxide nanoparticles. Hence the agglomeration of the particles was less in iron oxide than in graphene oxide nanoparticles. Also, the surface area created for the adsorption of CO_2 into nanoparticles was larger in the case of iron oxide nanoparticles. Similar results have been reported by [21] with different nanofluids in a packed column.

Brownian movement and micro-convection of a particle is an effect of the thermal motion of the molecular agitation of the liquid medium. Much stronger random displacement of a particle is usually observed in a less viscous liquid, with smaller particle size and higher temperature. The velocity field in the fluid, created by the Brownian motion of nanoparticles, can be responsible for such enhancement.

Effect of solvent flow rate on % CO_2 removal

The effect of solvent flow rate on CO_2 removal for the structured packing material with 12% (v/v) solvent concentration for the different iron oxide nanofluid concentrations, varying from 0.0001% (w/v) to 0.0015% (w/v), was shown in Fig. 5. It was observed that for 0.0001% (w/v) of Fe_3O_4 nanofluid the percentage of CO_2 removal was 78%, and for 0.001% (w/v) of Fe_3O_4 nanofluid, the percentage of CO_2 removal is almost 83%. At the higher concentration of Fe_3O_4 nanofluids, the percentage of CO_2 removal is 98%. It may be due to the increase in the concentration of nanoparticles

resulting in increased surface area for CO_2 absorption. CO_2 removal without nanofluids is 74%. Similar results have been reported in the previous study [21] in the packed column with nanofluids.

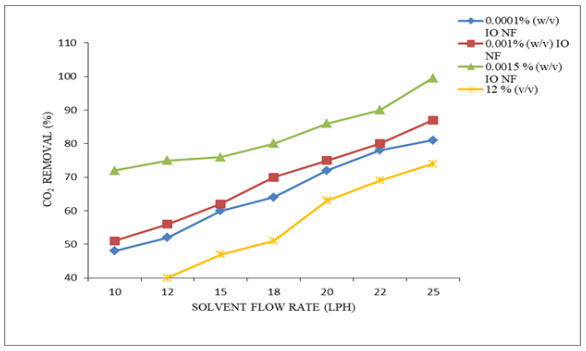

Figure 5. Effect of solvent flow rate on % CO_2 removal by employing iron oxide nanofluid and magnetic field.

Effect of solvent flow rate on rate of absorption

The effect of solvent flow rate on the absorption rate for the structured packing material with a 12% (v/v) solvent concentration for different iron oxide nanofluid concentrations (varying from 0.0001% (w/v) to 0.0015% (w/v) is shown in Fig. 6. The rate of CO_2 absorption was 0.0023 kmol/m^3s for 0.0001% (w/v) and for 0.001% (w/v) and 0.0015% (w/v) Fe_3O_4 nanofluids the rate of CO_2 absorption was 0.0025 kmol/m^3s. The mass transfer rate was enhanced with nanoparticles in a gas-liquid system. It was a gas transfer phenomenon from the gas-liquid phase to the liquid phase by gas adsorption in the dispersed Fe_3O_4 nanoparticles. Hence, the gas concentration near the interface will decrease, resulting in absorption enhancement. Similar results were reported in the previous study by [21] in the packed column with nanofluids.

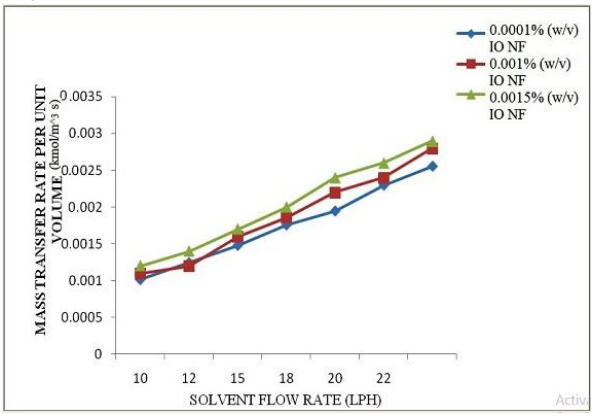

Figure 6. Effect of solvent flow rate on the rate of absorption by employing iron oxide nanofluid and magnetic field.

Effect of solvent flow rate on the number of transfer units

The effect of solvent flow rate on NTU for structured packing material with a 12% (v/v) solvent concentration for different iron oxide nanofluid concentrations (varying from 0.0001% (w/v) to 0.0015% (w/v) was shown in Fig. 7. The NTU value increases for a low Fe_3O_4 nanofluid concentration of 0.0001% (w/v) than 0.001% (w/v) and 0.0015% (w/v) due to the better magnetic iron particles that produce thermal energy leading to a low NTU value. Similar results have been reported in the previous study [22] in the packed column with nanofluids.

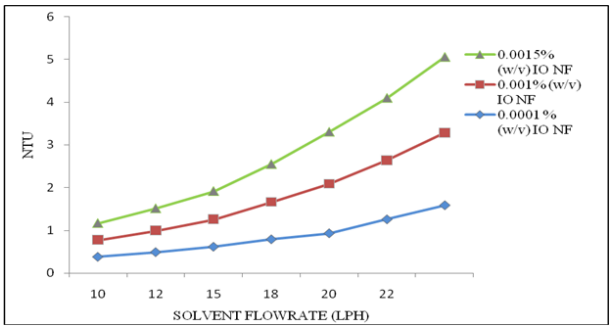

Figure 7. Effect of solvent flow rate on NTU by employing iron oxide nanofluid and magnetic field.

Effect of solvent flow rate on height of transfer unit

The effect of solvent flow rate on HTU for the structured packing material with a 12% (v/v) solvent concentration for the different iron oxide nanofluid concentrations (varying from 0.0001% (w/v) to 0.0015% (w/v) was shown in Fig. 8. The height of transfer unit is almost 1.6 for 0.0001% (w/v) iron oxide nanofluids. For higher nanofluids of 0.001% (w/v) and 0.0015% (w/v), the HTU value is 0.8. It was further observed that a lower value of HTU results in a high absorption performance. Similar results have been reported in a previous study [22] in the packed column with nanofluids.

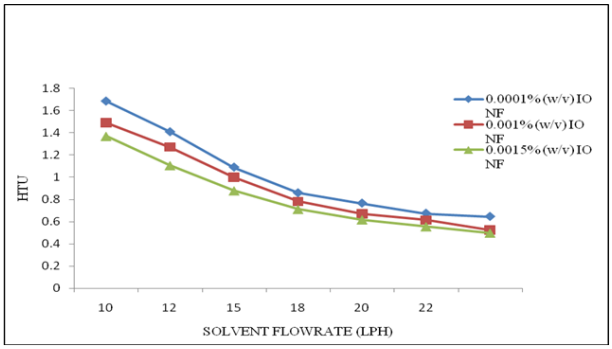

Figure 8. Effect of solvent flow rate on HTU by employing iron oxide nanofluid and magnetic field.

Effect of solvent flow rate on volumetric overall mass transfer coefficient

The effect of the solvent flow rate on the mass transfer coefficient for the structured packing material with a 12% (v/v) solvent concentration for different iron oxide nanofluid concentrations (varying from 0.0001% (w/v) to 0.0015% (w/v) is shown in Fig. 9. The mass

transfer coefficient increases with an increase in the solvent flow rate for all three Fe_3O_4 nanofluid concentrations. But for 0.0015% (w/v), iron oxide nanofluids increase the volumetric overall mass transfer coefficient to 27 kmol/h m^3. This increase in the overall volumetric mass transfer coefficient was due to the addition of magnetic iron oxide nanofluids in the absorbent. Similar results have been reported in the previous study by [23] in the packed column with nanofluids.

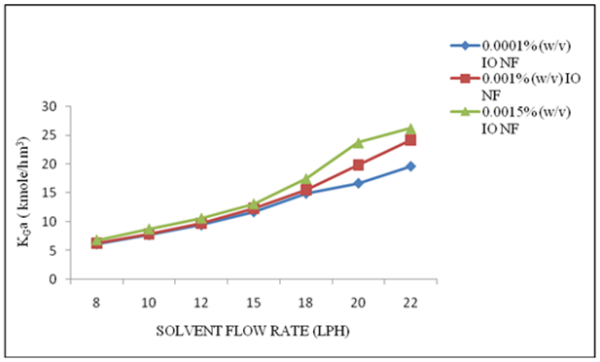

Figure 9. Effect of solvent flow rate on volumetric overall mass transfer coefficient by employing iron oxide nanofluid and magnetic field.

Optimum values of operational parameters

The efficiencies of the random and structured packing material in CO_2 removal are compared in Table 2. The structured packing material is more efficient in CO_2 removal than the random packing material. On the other hand, the efficiency of iron oxide with a magnetic field in CO_2 removal is higher than the efficiency of iron oxide, as can be seen in Table 3.

Table 2. Comparison between the random and structured packing material.

S.No.	% CO_2 removal	
	12% Random packing material	12% Structured packing material
1	30	34
2	36	40
3	44	47
4	47	51
5	57	63
6	58	69
7	62	74

Table 3. Comparison of % CO_2 removal for iron oxide and iron oxide with a magnetic field.

S.No.	Iron Oxide	Iron Oxide+ Magnetic Field
1	70	73
2	76	79
3	80	84
4	85	88
5	89	91
6	92	94
7	98	99.5

CONCLUSION

The CO_2 gas absorption studies were carried out in a packed absorption column. The selection of suitable solvent, comparison of random and structured packing material performance, enhancement of absorption by adding iron oxide nanoparticles in a solvent, and induction of magnetic field were in detail studied. As a result, the following conclusions were drawn.

Among the different solvents considered, NH_3 was the best for CO_2 gas absorption. Furthermore, structured packing resulted in higher efficiency than random packing. The CO_2 removal increased with an increase in the NH_3 concentration, and about 74% CO_2 removal was achieved. With the introduction of nanofluid like Fe_3O_4 along with the absorbent, the % CO_2 removal increased by 98%. Moreover, the Fe_3O_4 nanofluid showed a better result than the other nanofluids under all conditions because the other nano fluid settled in the solvent, whereas Fe_3O_4 was a magnetite form with better paramagnetic properties and lesser particles agglomerated. The paramagnetic nature of Fe_3O_4 particles favored the further marginal enhancement of CO_2 removal up to 99.5% with the application of an external magnetic field, whereas a 12% enhancement was seen [9]. The captured CO_2 from the packed column can be used in the product synthesis. The absorption kinetics of CO_2 over a while could be studied. CO_2 sequestration can be tried with hybrid nanofluids and also by varying particle size. The applied electric current to induce a magnetic field in this study is 2 mA, and future studies can be conducted by varying the electric current. Similarly, NO_2, and SO_2 sequestrations can also be examined in the structured packed column with nanofluids and the magnetic field.

REFERENCES

[1] A. Aroonwilas, Ind. Eng. Chem. Res. 43 (2004) 2228–2237. https://doi.org/10.1021/ie0306067.

[2] A. Aroonwilas, P. Tontiwachwuthikul, Chem. Eng. Sci. 55 (2000) 3651–3663. https://doi.org/10.1016/S0009-2509(00)00035-X.

[3] W.M.Budzianowski, R.Miller, Recent Pat. Mech. Eng. 2 (2009) 228–239. https://doi.org/10.2174/1874477X10902030228.

[4] T.W. Chien, H. Chu, H.T. Hsueh, J. Environ. Eng. 129 (2003) 967–974. https://doi.org/10.1061/(ASCE)0733-9372(2003)129:11(967).

[5] F. Zhang, C.-G. Fang, Y.-T. Wu, Y.-T. Wang, A.-M. Li, Z.-B. Zhang, Chem. Eng. J. 160 (2010) 691–697. https://doi.org/10.1016/j.cej.2010.04.013.

[6] H. Monnier, L. Falk, Chem. Eng. Sci. 66 (2011) 2475–2490. https://doi.org/10.1016/j.ces.2011.01.016.

[7] H. Monnier, L. Falk, N. Mhiri, Chem. Eng. Process. 49 (2010) 953–957. https://doi.org/10.1016/j.cep.2010.05.001.

[8] J. Salimi, F. Salimi, Rev. Mex. Ing. Quim. 15 (2016) 185–192. http://www.rmiq.org/ojs311/index.php/rmiq/article/view/1106/413.

[9] J. Salimi, F. Salimi, Heat Mass Transfer 51 (2015) 621–629. https://doi.org/10.1007/s00231-014-1439-5.

[10] A.O. Lawal, R.O. Idem, Ind. Eng. Chem. Res. 45 (2006) 2601–2607. https://doi.org//10.1021/ie050560c.

[11] R. Notz, N. Asprion, I. Clausen, H. Hasse, Chem. Eng. Res. Des. 85 (2007) 510–515. https://doi.org/10.1205/cherd06085.

[12] P. Oinas, G. Wild, N. Midoux, H. Haario, Chem. Eng. Process. 34 (1995) 503–513. https://doi.org/10.1016/0255-2701(95)00454-8.

[13] O. Lawal, A. Bello, R. Idem, Ind. Eng. Chem. Res. 44 (2005) 1874–1879. https://doi.org/10.1021/ie049261y.

[14] Z. Niu, Y. Guo, Q. Zeng, W. Lin, Ind. Eng. Chem. Res. 51 (2012) 5309–5319. https://doi.org/10.1021/ie2030536.

[15] Q. Zeng, W. Lin, Y. Guo, Z. Niu, Fuel Process. Technol. 108 (2013) 76–81. https://doi.org/10.1016/j.fuproc.2012.05.005.

[16] P.P. Selvi, R. Baskar, P.S. Nair, J. Adv. Chem. 13 (2017) 6520–6523. https://doi.org/10.24297/jac.v13i10.5789.

[17] P.P. Selvi, R. Baskar, J. Chem. Soc. Pak. 41 (2019) 820–824. https://jcsp.org.pk/PublishedVersion/3b17aa02-80a4-466d- aaa9- cff35adc7448Manuscript%20no%2010,%20Final%20Gally%20Proof%20of%2011943%20(Pongayi%20Ponnusamy%20Selvi).pdf.

[18] P.P. Selvi, R. Baskar, Chem. Ind. Chem. Eng. Q. 26 (2020) 321–328. https://doi.org/10.2298/CICEQ181225008S.

[19] S.-S. Ashrafmansouri, M.N. Esfahany, Inter. J. Therm. Sci. 82 (2014) 84–99. https://doi.org/10.1016/j.ijthermalsci.2014.03.017.

[20] W. Yu, H. Xie, J. Nano Mater. 2012 (2011) ID 435873. https://doi.org/10.1155/2012/435873.

[21] W. Hao, E. Bjorkman, M. Lilliestrale, N. Hedin, Chem. Sustainability 7 (2014) 875–882. https://doi.org/10.1002/cssc.201300912.

[22] W. Yuan, B. Li B, L. Li, Appl. Surf. Sci.257 (2011) 10183–10187. https://doi.org/10.1016/j.apsusc.2011.07.015.

[23] Z. Zhang, W. Zhang, X. Chen, Q. Xia, Z. Li, Sep. Sci. Technol. 45 (2010) 710–719. https://doi.org/10.1080/01496390903571192.

[24] M. M. Tun, D. Juchelková, Environ. Eng. Res. 24 (2019) 618–629. http://dx.doi.org/10.4491/eer.2018.327.

[25] Z. Samadi, M Haghshenasfard, A Moheb, Chem. Eng. Technol. 37 (2014) 462–470. https://doi.org/10.1002/ceat.201300339.

[26] M. Ansaripour, M Haghshenasfard, A Moheb, Chem. Eng. Technol. 41 (2018) 367–378. https://doi.org/10.1002/ceat.201700182.

[27] M.Khani, M. Haghshenasfard, N. Etesami, M.R. Talaei, J. Mol. Liq. 334 (2021) 116078. https://doi.org/10.1016/j.molliq.2021.116078.

PONGAYI PONNUSAMY SELVI[1]

RAJOO BASKAR[2]

[1]Department of Chemical Engineering, Kongu Engineering College, Perundurai, Tamil Nadu, India

[2]Department of Food Technology, Kongu Engineering College, Perundurai, Tamil Nadu, India

NAUČNI RAD

ISTRAŽIVANJA UKLANJANJA CO_2 U APSORPCIONOJ KOLONI SA PAKOVANJEM KORIŠĆENJEM NANOFLUIDA SA OKSIDOM GVOŽĐA

Izazovan zadatak u našem ekosistemu je da u određenoj meri smanjimo emisije kiselih gasova. Mnogi gasovi se emituju iz industrija, kao što su H_2S, CO, CO_2, SO_2, NO i NO_2. Među ovim gasovima, CO_2, NO_2 i SO_2 su kiseli, što dovodi do štetnih efekata na ljude, životinje i biljke. Povećanje emisije CO_2 gasova iz antropogenih i industrijskih izvora iniciralo je studije uklanjanja CO_2. Studije apsorpcije CO_2 su sprovedene korišćenjem nanofluida sa gvožđe-oksidom sa novom apsorpcionom kolonom sa strukturiranim pakovanjem. Nanočestice oksida gvožđa su sintetizovane i okarakterisane KSRD, SEM i TEM analizom. Amonijak se koristi kao apsorbent zajedno sa nanofluidom sa oksidom gvožđa u tri različite koncentracije (0,0001%, 0,001% i 0,0015%). Utvrđeno je da je ovaj nanofluid u koncentraciji od 0,0015% pokazao poboljšanu efikasnost uklanjanja CO_2. Ova poboljšana efikasnost uklanjanja % CO_2 je rezultat povećane međufazne površine poboljšanog kontakta između tečne i gasne faze. Pored toga, magnetno polje je razvijeno duž kolone, što je povećalo efikasnost uklanjanja CO_2 za 1,5%.

Ključne reči: apsorpcija, efikasnost uklanjanja CO_2, međufazna površina, koeficijent prenosa mase, nanofluid, kolona sa pakovanjem.